1.3 Background reading

Bethe, H. (1929) Splitting of terms in crystals. (Termsaufspaltung in Kristallen.) *Ann. Phys.*, **3**, 133–206. [*Transl.*: Consultants Bureau, New York.]

Burns, R. G., Clark, R. H. & Fyfe, W. S. (1964) Crystal field theory and applications to problems in geochemistry. In *Chemistry of the Earth's Crust, Proceedings of the Vernadsky Centennial Symposium.* (A. P. Vinogradov, ed.; Science Press, Moscow), **2**, 88–106. [*Transl.*: Israel Progr. Sci. Transl., Jerusalem , pp. 93–112 (1967).]

Burns, R. G. & Fyfe, W. S. (1967a) Crystal field theory and the geochemistry of transition elements. In *Researches in Geochemistry.* (P. H. Abelson, ed.; J. Wiley & Son, New York), **2**, 259–85.

Burns, R. G. (1985) Thermodynamic data from crystal field spectra. In *Macroscopic to Microscopic. Atomic Environments to Mineral Thermodynamics.* (S. W. Kieffer & A. Navrotsky, eds; Mineral. Soc. Amer. Publ.), *Rev. Mineral.*, **14**, 277–316.

Orgel, L. E. (1952) The effects of crystal fields on the properties of transition metal ions. *J. Chem. Soc.*, pp. 4756–61.

Williams, R. J. P. (1959) Deposition of trace elements in a basic magma. *Nature*, **184**, 44.

2

Outline of crystal field theory

Crystal field theory gives a survey of the effects of electric fields of definite symmetries on an atom in a crystal structure.
– – A direct physical confirmation should be obtainable by analysis of the spectra of crystals.
H. A. Bethe, *Annalen der Physik*, 3, 206 (1929)

2.1 Introduction

Crystal field theory describes the origins and consequences of interactions of the surroundings on the orbital energy levels of a transition metal ion. These interactions are electrostatic fields originating from the negatively charged anions or dipolar groups, which are collectively termed ligands and are treated as point negative charges situated on a lattice about the transition metal ion. This is a gross simplification, of course, because sizes of anions or ligands such as O^{2-}, OH^-, H_2O, SO_4^{2-}, etc., are much larger than corresponding ionic radii of cations (Appendix 3). Two effects of the crystalline field are the symmetry and the intensity of the electrostatic field produced by the ligands. The changes induced on the central transition metal ion depend on the type, positions and symmetry of the surrounding ligands.

2.2 Orbitals

The position and energy of each electron surrounding the nucleus of an atom are described by a wave function, which represents a solution to the Schrödinger wave equation. These wave functions express the spatial distribution of electron density about the nucleus, and are thus related to the probability of finding the electron at a particular point at an instant of time. The wave function for each electron, $\Psi(r,\theta,\phi)$, may be written as the product of four separate functions, three of which depend on the polar coordinates of the electron

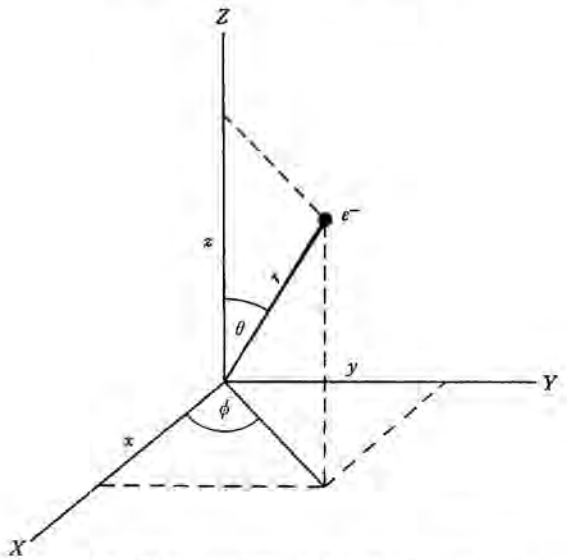

Figure 2.1 Polar coordinates of an electron in space.

illustrated in fig. 2.1. These three functions include the radial function, $R(r)$, which depends only on the radial distance, r, of the electron from the nucleus, and two angular functions $\Theta(\theta)$ and $\Phi(\phi)$ which depend only on the angles θ and ϕ. The fourth function, the spin function, Ψ_s, is independent of the spatial coordinates r, θ and ϕ. Thus, the overall wave function of an electron may be written as the product

$$\Psi(r,\theta,\phi) = R(r)\ \Theta(\theta)\ \Phi(\phi)\ \Psi_s\ . \tag{2.1}$$

Surfaces may be drawn to enclose the amplitude of the angular wave function. These boundary surfaces are the atomic orbitals, and lobes of each orbital have either positive or negative signs resulting as mathematical solutions to the Schrödinger wave equation.

The overall wave function and each of its components are expressed in terms of certain parameters called quantum numbers, four of which are designated n, l, m_l and m_s.

2.2.1 Principal quantum number n

Solutions to the $R(r)$ portion of the Schrödinger equation are expressed as

$$E_n = -\frac{1}{n^2}\frac{2\pi^2\mu^2Z^2e^4}{h^2}\ , \tag{2.2}$$

where E_n is the energy of an electron with charge e; Z is the charge on the nucleus; μ is the reduced mass of the electron (m) and the nucleus (M), with $\mu = Mm/(M + m)$; h is Planck's constant; and n is the principal quantum number relating to the average distance of the electron from the nucleus.

The principal quantum number, n, can have all integral values from 1 to infinity. It is a measure of the energy of an electron. Thus, $n = 1$ is the lowest energy orbital level. As n increases, the energies of the orbitals increase, becoming less negative. In the limit of $n = \infty$, the energy of the electron becomes zero. The electron is no longer bound to the nucleus, so that the atom becomes ionized. There is then a continuum of states with zero bonding energy and an arbitrary kinetic energy. The ionization energy corresponds to the energy difference between the $n = 1$ and $n = \infty$ levels.

2.2.2 Azimuthal quantum number l

The azimuthal quantum number or orbital angular momentum quantum number, l, is related to the shape of an orbital and occurs in solutions to the $\Theta(\theta)$ function of the wave equation. It may be regarded as representing the angular momentum of an electron rotating in an orbit, the magnitude of which corresponds to $[l(l + 1)]^{1/2}$ units of $h/2\pi$. Again, l can have only integral values, but its maximum value is limited by the value of n associated with the orbital. Thus, l has the values 0, 1, 2, ..., $(n-1)$. In the first shell, for example, $n = 1$ and there exists only one wave function with $l = 0$. In the second shell $n = 2$, and there are wave functions with $l = 0$ and $l = 1$. Similarly, in the third shell $n = 3$ so that l can take the values 0, 1, and 2; and so on.

Letter symbols are given to the orbitals according to the value of l as follows:

$$\begin{aligned} &\text{for } l = 0, 1, 2, 3, 4, \ldots \\ &\text{the letter symbol is: } s, p, d, f, g, \ldots \end{aligned} \tag{2.3}$$

Thus, s orbitals are states with $l = 0$ and zero orbital angular momentum. The p orbitals with $l = 1$ have orbital angular momenta of $\sqrt{2}$ units of $h/2\pi$, while the d orbitals with $l = 2$ have $\sqrt{6}\ h/2\pi$ units of orbital angular momenta.

2.2.3 Magnetic quantum number m_l

The quantum number, m_l, originating from the $\Theta(\theta)$ and $\Phi(\phi)$ functions of the Schrödinger wave equation, indicates how the orbital angular momentum is oriented relative to some fixed direction, particularly in a magnetic field. Thus, m_l roughly characterizes the directions of maximum extension of the electron

cloud in space. The orbiting, negatively charged electron generates a magnetic field. In the presence of an applied magnetic field along one axis, designated by convention as the z axis, interactions between the two magnetic fields cause the orbital angular momentum vector to be constrained in specific directions. These directions are quantized such that they can have only integral values along the z axis. The quantum number m_l occurs in solutions to both the $\Theta(\theta)$ and $\Phi(\phi)$functions of the Schrödinger equation and can take all integral values from $+l$ to $-l$, or $(2l + 1)$ values in all. For example, for a given principal quantum number n and with $l = 0$, there is only one possible orbital, namely one with $m_l = 0$. Thus, there is only one s orbital associated with each principal quantum shell. These are designated as $1s$, $2s$, $3s$, $4s$, etc., orbitals. For a given n and with $l = 1$, there are three possible values for m_l: -1, 0 and $+1$. Hence, there are three different kinds of p orbitals for each principal quantum number (except $n = 1$) and they constitute the $2p$, $3p$, $4p$, $5p$, etc., orbitals. Similarly, there are five different d orbitals, since $l = 2$ and m_l can take the values 2, 1, 0, -1, and -2. Thus, the $3d$, $4d$, $5d$, etc., shells each contain five d orbitals. The f orbitals, designated as $4f$, $5f$, etc., occur in sets of 7; g orbitals, starting with $5g$, occur in sets of 9; and so on. The energies of orbitals with the same n and l values but different values of m_l are the same, except in the presence of a strong electric or magnetic field. Thus, all three p orbitals in a given shell have the same energies, as do the five d orbitals. The p orbitals are said to be three-fold degenerate and the d orbitals are five-fold degenerate.

2.2.4 Spin quantum number m_s

An electron may be visualized as spinning about some axis. Thus, it possesses spin angular momentum. However, since the electron is negatively charged there will be produced a magnetic field associated with its spin. Depending on the sense of rotation, clockwise or anticlockwise, the magnetic field may be in one or the opposite direction. An electron then can have two kinds of spin, characterized by the quantum numbers $m_s = +\frac{1}{2}$ and $m_s = -\frac{1}{2}$. The magnitude of the spin angular momentum is $[s(s + 1)]^{1/2}$ units of $h/2\pi$, where $s = \frac{1}{2}$. Accordingly, for each space orbital characterized by the quantum numbers, n, l and m_l, there are two possible arrangements of electron spin generally of the same energy in the absence of a magnetic field. Thus, each orbital can accommodate two electrons which spin in opposite directions. In energy level diagrams these are often referred to as spin-up (or α-spin) and spin-down (or β-spin) configurations.

2.2.5 Spin–orbit coupling

The interaction of the two magnetic fields, one produced by an electron spinning around its axis and the other by its rotation in an orbital around the nucleus, is termed spin-orbit coupling. States with opposed magnetic fields associated with spin and rotation are slightly more stable than those with aligned magnetic fields. Effects of spin–orbit coupling become increasingly important with rising atomic number. They are thus more noticable in compounds of Co and Ni than they are in V- and Cr-bearing phases; spin–orbit interactions are particularly significant in elements of the second and third transition series. Spin–orbit coupling influences electron paramagnetic resonance spectra, and also contribute features to visible-region spectra of transition metal compounds, particularly of Co^{2+} and Ni^{2+}-bearing phases.

2.3 Shape and symmetry of the orbitals

All s orbitals are spherically symmetrical because their angular wave functions are independent of θ and ϕ. They are given the group theory symmetry notation a_{1g}; here, symbol a indicates single degeneracy, that is, there is one s orbital per quantum number; subscript 1 means that the sign of the wave function does not change on rotation about the centre of the atom; and subscript g refers to the fact that the wave function does not change sign on inversion through the centre of the atom (German: *gerade* = even). The symbol a_{1g} implies spherical symmetry and s orbitals are said to have symmetric wave functions. The spatial properties of the s orbitals are shown in fig. 2.2. The balloon picture of the orbital is constructed so that the skin of the balloon includes within it most, perhaps 95 per cent, of the electron density. The sign of the wave function of s orbitals is independent of angle in any given spherical shell. Note that for s orbitals alone, there is a finite probability that the electron may be at the nucleus. This feature is important in Mössbauer spectroscopy because the s electron density at the nucleus influences the value of the chemical isomer shift parameter.

The three p orbitals in each shell are mutually perpendicular and depend on the angles θ and ϕ. Individually, they are not spherically symmetrical. The three p orbitals in each set are designated by p_x, p_y and p_z, indicating that lobes project along each of the cartesian axes. The signs of the wave functions represented by the two lobes of each orbital are different. Figure 2.2 shows the angular wave functions of the p orbitals. The p orbitals are shaped like dumbbells and belong to symmetry type t_{1u}: here, t represents the three orbitals per principal quantum number, or three-fold degeneracy; subscript 1 again indicates that the sign of the wave function does not change on rotation about the

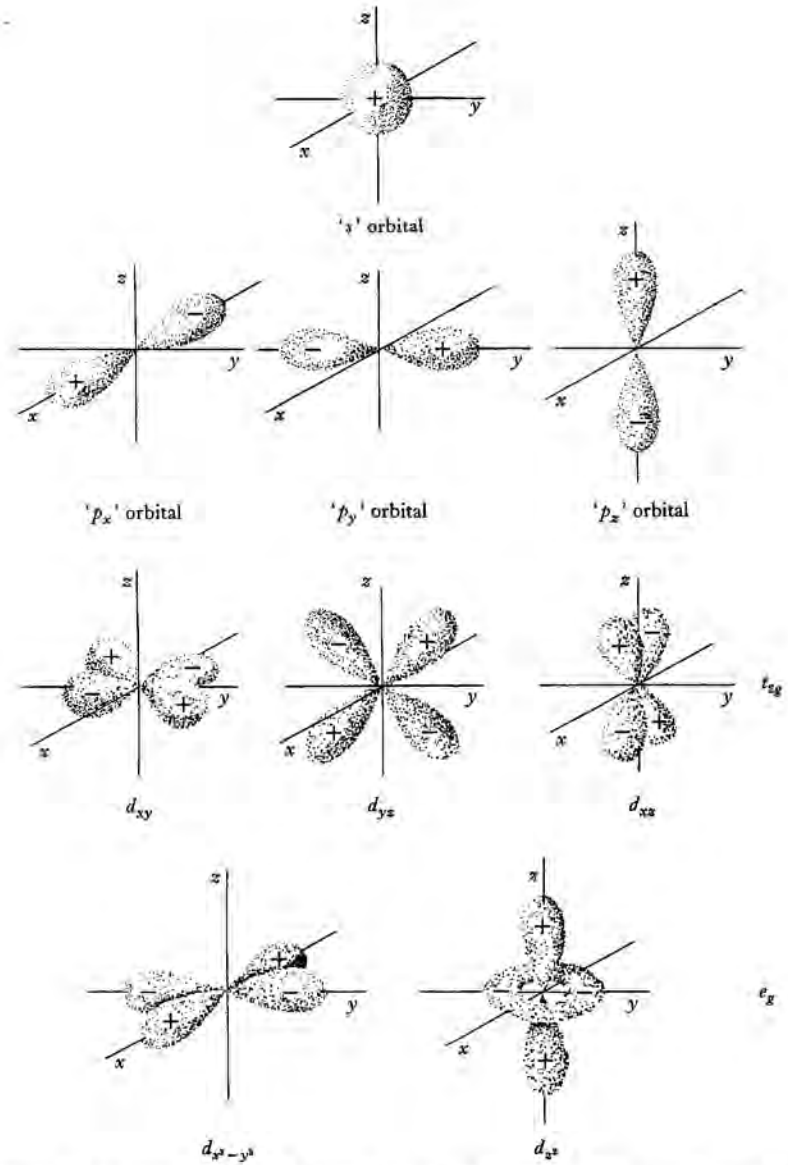

Figure 2.2 Boundary surface of atomic orbitals. The boundaries represent angular distribution probabilities for electrons in each orbital. The sign of each wave function is shown. The *d* orbitals have been classified into two groups, t_{2g} and e_g, on the basis of spatial configuration with respect to the cartesian axes. (Reproduced and modified from: W. S. Fyfe, *Geochemistry of Solids*, McGraw–Hill, New York, 1964, figure 2.5, p. 19).

cartesian axes; and subscript *u* shows that the sign of the wave function changes on inversion through the centre of the atom (German: *ungerade* = uneven). Thus, *p* orbitals are said to be antisymmetric.

The five *d* orbitals which occur in each shell with principal quantum number 3 or higher are designated by d_{xy}, d_{yz}, d_{xz}, $d_{x^2-y^2}$ and d_{z^2}, and each orbital has four lobes in opposite quadrants. This is illustrated in fig. 2.2. The five *d* orbitals may be divided into two groups on the basis of their angular distributions. Three of the orbitals, d_{xy}, d_{yz} and d_{xz}, have lobes projecting between the cartesian axes. This group is designated t_{2g}: here, *t* refers to the three-fold degeneracy; subscript 2 indicates that the sign of the wave function does not change on rotation about the axes diagonal to the cartesian axes; and subscript *g* again refers to the fact that the wave function does not change sign on inversion (*gerade*). The other two orbitals, $d_{x^2-y^2}$ and d_{z^2}, have lobes directed along the cartesian axes. They are designated e_g, where *e* stands for the two-fold degeneracy. The d_{z^2} orbital appears to have a different shape from the other four. This difference is only apparent, however. The d_{z^2} orbital represents a linear combination of two orbitals, $d_{z^2-x^2}$ and $d_{z^2-y^2}$, having the same shape as the other *d* orbitals but which are not independent of them. Note that each of the five *d* orbitals has a symmetric (*g*) wave function, like an *s* orbital. Thus, *d* and *s* orbitals are said to have the same parity. However, *d* orbitals (*g*) and *p* orbitals (*u*) have opposite parities. Also, the plus and minus signs associated with the orbitals illustrated in fig. 2.2 refer to the mathematical signs of the wave functions. The electron density is always positive, however, and is obtained by squaring a wave function. Sometimes, an alternative designation is used for the two groups of *d* orbitals, namely d_ε and d_γ for the e_g and t_{2g} orbitals, respectively.

In passing, it should be noted that there are seven *f* orbitals in the 4*f*, 5*f*, etc., shells. They consist of one orbital, designated f_{xyz} and having a_{2u} symmetry, with eight lobes pointing between the *x*, *y* and *z* axes; three more orbitals, denoted as $f_{z(x^2-y^2)}$, $f_{x(y^2-z^2)}$ and $f_{y(z^2-x^2)}$ with t_{2u} symmetry, in which eight lobes are directed along two of the axes; and three other orbitals labelled as f_{x^3}, f_{y^3} and f_{z^3} with t_{1u} symmetry, that are somewhat analogous to the d_{z^2} orbital by having lobes directed along each cartesian axis and two more regions above and below the plane of the other two axes.

An orbital is capable of accommodating two electrons which, according to the Pauli exclusion principle, must be spinning in opposite directions. Thus, each *s* orbital may contain two electrons, the three *p* orbitals a total of six electrons, the five *d* orbitals up to ten electrons, and the *f* orbitals a maximum of 14 electrons. When there is an insufficient number of electrons in an atom to completely fill a set of orbitals, the electrons may spread out and occupy singly as many of the orbitals as possible with spins aligned parallel; that is, the electrons

spin in the same direction to maximize the exchange energy, in accord with Hund's rules of electronic configurations. Such a distribution minimizes inter-electronic coulombic repulsion and leads to lowest energy states, or ground state configurations, which have the maximum number of unpaired electrons.

2.4 Transition elements

The definition of a transition element, *senso stricto*, is that it is a metal having a partly filled *d* or *f* shell. A broader definition includes also those elements that have partially filled *d* or *f* shells in any one of their commonly occurring oxidation states. Elements of the first transition series have electronic configurations of the general form

$$(1s)^2(2s)^2(2p)^6(3s)^2(3p)^6(3d)^{10-n}(4s)^{1 \text{ or } 2}, \qquad (2.4)$$

where $n = 0, 1, 2, \ldots, 10$. Since the closed shell configuration $(1s)^2(2s)^2(2p)^6(3s)^2(3p)^6$ corresponds to the inert gas argon, Ar, it is termed the argon core and is abbreviated [Ar]. In passing from one element to the next along the first transition series, the 3*d* orbitals are filled progressively. Cations in different oxidation states of the transition elements are formed by the removal of the 4*s* and some, or all, of the 3*d* electrons. Table 2.1 summarizes the electronic configurations of elements of the first transition series in their naturally occurring oxidation states in geochemical environments. Included in table 2.1 are titanium(IV), vanadium(V) and chromium(VI) retaining zero 3*d* electrons, and copper(I) with completely filled 3*d* orbitals. Elements belonging to the second transition series (Y to Ag) and third transition series (from Hf to Au) have partly filled 4*d* and 5*d* orbitals, respectively, whereas the lanthanide elements spanning La to Lu have incompletely filled 4*f* or 5*d* orbitals. Note that on Earth, the most stable oxidation states in minerals occurring in near-surface environments include Ti(IV), V(III), V(V), Cr(III), Cr(VI), Mn(II), Mn(III), Mn(IV), Fe(II), Fe(III), Co(II), Co(III), Ni(II), Cu(II) and Cu(I). On the Moon, however, the oxidation states Fe(II), Mn(II), Ti(III), Ti(IV), Cr(II) and Cr(III) occur in lunar mineral and glass phases. Ferric iron may predominate over Fe(II) in the martian regolith, particularly in bright regions of Mars.

In an isolated transition metal ion, electrons have an equal probability of being located in any one of the five *d* orbitals, since these orbitals have identical energy levels. When a transition metal ion is in a crystal structure, however, the effect of a non-spherical electrostatic field on the five degenerate *d* orbitals is to lower the degeneracy by splitting the *d* orbitals into different energies about the centre of gravity, or baricentre, of the unsplit energy levels. The manner and extent to which the five-fold degeneracy is removed depends on the type, positions and symmetry of ligands surrounding the transition metal.

Table 2.1. *Electronic configurations of the first-series transition elements occurring in minerals*

	Atomic number	Element	Electronic configurations						
			Atom	M(I)	M(II)	M(III)	M(IV)	M(V)	M(VI)
first-series transition elements	19	K	$[Ar]4s^1$	[Ar]					
	20	Ca	$[Ar]4s^2$		[Ar]				
	21	Sc	$[Ar]3d^14s^2$			[Ar]			
	22	Ti	$[Ar]3d^24s^2$		$[Ar]3d^2$	$[Ar]3d^1$	[Ar]		
	23	V	$[Ar]3d^34s^2$		$[Ar]3d^3$	$[Ar]3d^2$	$[Ar]3d^1$	[Ar]	
	24	Cr	$[Ar]3d^54s^1$		$[Ar]3d^4$	$[Ar]3d^3$	$[Ar]3d^2$	$[Ar]3d^1$	[Ar]
	25	Mn	$[Ar]3d^54s^2$		$[Ar]3d^5$	$[Ar]3d^4$	$[Ar]3d^3$		
	26	Fe	$[Ar]3d^64s^2$		$[Ar]3d^6$	$[Ar]3d^5$			
	27	Co	$[Ar]3d^74s^2$		$[Ar]3d^7$	$[Ar]3d^6$			
	28	Ni	$[Ar]3d^84s^2$		$[Ar]3d^8$	$[Ar]3d^7$			
	29	Cu	$[Ar]3d^{10}4s^1$	$[Ar]3d^{10}$	$[Ar]3d^9$				
	30	Zn	$[Ar]3d^{10}4s^2$		$[Ar]3d^{10}$				
	31	Ga	$[Ar]3d^{10}4s^24p^1$			$[Ar]3d^{10}$			
	32	Ge	$[Ar]3d^{10}4s^24p^2$				$[Ar]3d^{10}$		

[Ar] = Argon core, $1s^22s^22p^63s^23p^6$

2.5 Crystal field splitting in octahedral coordination

When a transition metal ion is in octahedral coordination with six identical ligands situated along the cartesian axes, electrons in all five 3*d* orbitals are repelled by the negatively charged anions or dipolar ligands, and the baricentre of the degenerate levels is raised. Since lobes of the e_g orbitals point towards the ligands, electrons in these two orbitals are repelled to a greater extent than are those in the three t_{2g} orbitals that project between the ligands. This difference between e_g and t_{2g} orbitals is illustrated in fig. 2.3 for the $d_{x^2-y^2}$ and d_{xy} orbitals in the *x*–*y* plane. Therefore, the e_g orbitals are raised in energy relative to the t_{2g} orbitals, which may be represented by an energy level diagram, as in fig. 2.4. The energy separation between the t_{2g} and e_g orbitals is termed the crystal field splitting and is designated by Δ_o. Alternatively, the symbol 10 *Dq* utilized in ligand field theory is sometimes used, and $\Delta_o = 10\,Dq$ (see §2.7). An analogous energy separation between t_{2g} and e_g orbital groups exists in the schematic molecular orbital energy level diagram shown in fig. 2.5 which shows 10 *Dq* (or Δ_o) to be the energy separation between orbitals of the t_{2g} and antibonding e_g^* groups (§11.3.1). The value of Δ_o or 10 *Dq* is obtained directly, or may be estimated, from spectral measurements of transition metal-bearing phases in the visible to near-infrared region.

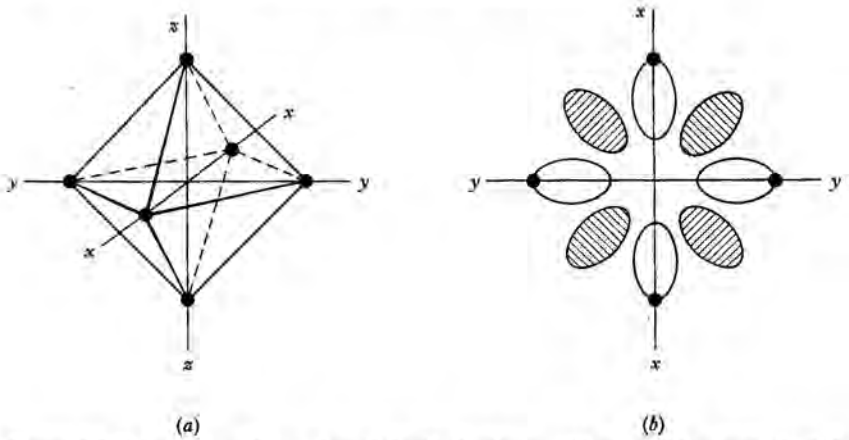

Figure 2.3 Orientations of ligands and *d* orbitals of a transition metal ion in octahedral coordination. (*a*) Orientation of ligands with respect to the cartesian axes; (*b*) the *x*–*y* plane of a transition metal ion in an octahedral crystal field. The d_{xy} orbital is cross-hatched; the $d_{x^2-y^2}$ orbital is open; ligands are black circles.

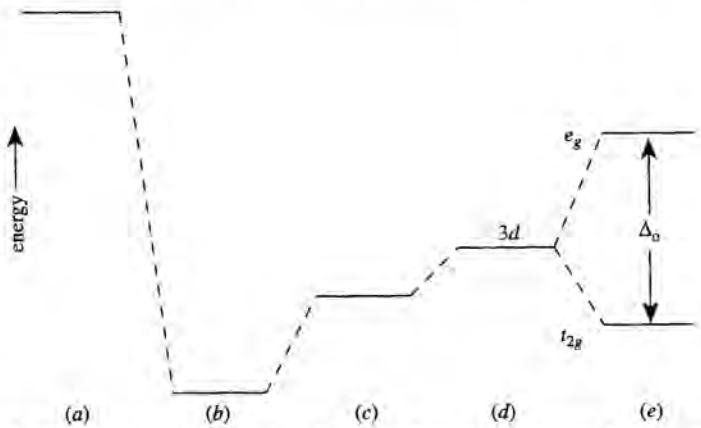

Figure 2.4 Relative energies of a transition metal 3*d* orbitals in octahedral coordination. (*a*) Energy levels of a free cation; (*b*) electrostatic attraction between the cation and anions; (*c*) repulsion between anions and electrons on the cation other than those in 3*d* orbitals; (*d*) repulsion between anions and the 3*d* electrons; (*e*) splitting of 3*d* orbital energy levels in an octahedral crystal field (from Burns, 1985a).

In the crystal field model, the split 3*d* orbital energy levels are assumed to obey a 'centre of gravity' rule. As a result, the three t_{2g} orbitals are lowered by $0.4\Delta_o$ below, and the two e_g orbitals raised by $0.6\Delta_o$ above, the baricentre. This follows from a simple algebraic argument that the energy of six electrons in the three t_{2g} orbitals is compensated by the energy of four electrons in the two e_g

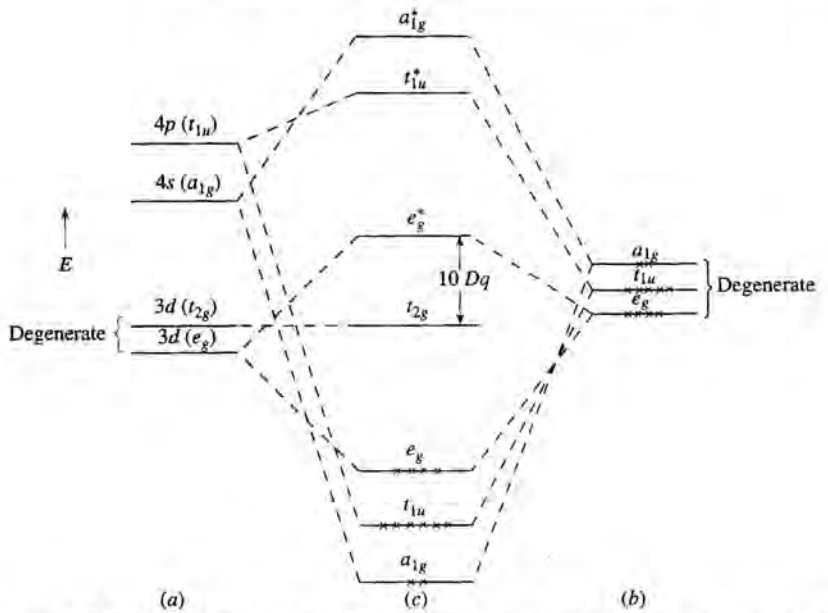

Figure 2.5 Schematic molecular orbital energy level diagram for a transition metal coordination cluster, $[ML_6]$. (*a*) Energy levels of atomic orbitals of the free cation, M; (*b*) energy levels for the six ligands, L, before bonding; (*c*) molecular orbital energy levels for the octahedral $[ML_6]$ cluster.

orbitals. Each electron in a t_{2g} orbital thus stabilizes a transition metal ion by $0.4\Delta_o$, whereas every electron in an e_g orbital diminishes the stability by $0.6\Delta_o$. The resultant nett stabilization energy is termed the crystal field stabilization energy and is designated by CFSE.

The distribution of 3*d* electrons in a given transition metal ion is controlled by two opposing tendencies. First, repulsion and exchange interactions between electrons causes them to be distributed over as many of the 3*d* orbitals as possible with parallel spins. This is in accordance with Hund's first rule. Secondly, the effect of crystal field splitting is to cause electrons to populate 3*d* orbitals having the lowest energy. These two opposing tendencies lead to high-spin and low-spin electronic configurations in certain transition metal ions. The distinction between the high-spin and low-spin states is an experimental one based on, for example, interatomic distances, magnetic susceptibility, visible-region and various X-ray spectroscopic measurements and, in the case of iron, the chemical isomer shift parameter determined by Mössbauer spectroscopy.

Consider the elements of the first transition series in octahedral coordination. Ions with one, two or three 3*d* electrons (for example, Ti^{3+}, V^{3+} and Cr^{3+}, respectively) each can have only one electronic configuration, and the electrons occupy

singly different orbitals of the t_{2g} group with spins aligned parallel. However, ions possessing four, five, six and seven $3d$ electrons (such as Cr^{2+} and Mn^{3+}, Mn^{2+} and Fe^{3+}, Fe^{2+} and Co^{3+}, and Co^{2+} and Ni^{3+}, respectively) have a choice of electronic configuration. The Mn^{3+} ion, for example, with the $3d^4$ configuration may adopt the high-spin state in which three of the $3d$ electrons occupy singly each of the t_{2g} orbitals and the fourth enters an e_g orbital. The CFSE is reduced by the fourth electron entering an e_g orbital, but energy is not expended by the pairing of this electron in one of the half-filled t_{2g} orbitals. Alternatively, the Mn^{3+} ion may attain the low-spin state in which the fourth electron does fill one of the low energy t_{2g} orbitals. The gain in CFSE may outweigh the energy required to pair two electrons in one orbital. Similar factors apply to high-spin and low-spin states for each of the cations with $3d^5$, $3d^6$ and $3d^7$ configurations. Cations having eight, nine and ten $3d$ electrons (for example, Ni^{2+}, Cu^{2+} and Zn^{2+}, respectively) can each possess only one electronic configuration as the t_{2g} orbitals are filled completely. Electronic configurations and crystal field stabilization energies of the transition metal ions in high-spin and low-spin states in octahedral coordination are summarized in table 2.2. Of particular geophysical significance is the possibility that high pressure may induce spin-pairing transitions in iron-bearing minerals in the deep in the Earth's Mantle. This aspect is discussed in chapter 9 (§9.7)

It can be seen from table 2.2 that transition metal ions with $3d^3$, $3d^8$ and low-spin $3d^6$ configurations acquire significantly higher CFSE's in octahedral coordination than other cations. Therefore, ions such as Cr^{3+}, Mn^{4+}, Ni^{2+}, and Co^{3+} are expected to show strong preferences for octahedral coordination sites. Cations with $3d^0$, $3d^{10}$ and high-spin $3d^5$ configurations, such as Ca^{2+}, Zn^{2+}, Mn^{2+} and Fe^{3+}, receive zero CFSE in octahedral coordination.

If there is competition between pairing energy and crystal field stabilization energy, a cation may be unstable towards oxidation and reduction. For example, the Mn^{3+} ($3d^4$) ion is readily oxidized to the Mn(IV) oxidation state and is easily reduced to the Mn^{2+} ion. In addition, the Mn^{3+} ion disproportionates in aqueous solution:

$$2\ Mn^{3+}_{(aq)} + 2\ H_2O_{(l)} \rightarrow Mn^{2+}_{(aq)} + MnO_{2\ (s)} + 4\ H^+_{(aq)} \qquad (2.5)$$

$$\Delta G^\circ_{298} = -109\ \text{kJ mole}^{-1}$$

$$2\ Mn(OH)_{3\ (s)} \rightarrow Mn(OH)_{2\ (s)} + MnO_{2\ (s)} + 2\ H_2O_{(l)}. \qquad (2.6)$$

$$\Delta G^\circ_{298} = -42\ \text{kJ mole}^{-1}$$

Table 2.2. *Electronic configurations and crystal field stabilization energies of transition metal ions in octahedral coordination*

Number of $3d$ electrons	Cation	High-spin state				Low-spin state			
		Electronic configuration		Unpaired electrons	CFSE	Electronic configuration		Unpaired electrons	CFSE
		t_{2g}	e_g			t_{2g}	e_g		
0	Ca^{2+}, Sc^{3+}, Ti^{4+}	↿⇂		0	0	↿⇂		0	0
1	Ti^{3+}	↿		1	$\frac{3}{5}\Delta_0$	↿⇂		1	$\frac{3}{5}\Delta_0$
2	Ti^{2+}, V^{3+}	↿	↿	2	$\frac{4}{5}\Delta_0$	↿⇂		2	$\frac{4}{5}\Delta_0$
3	V^{2+}, Cr^{3+}, Mn^{4+}	↿	↿	3	$\frac{6}{5}\Delta_0$	↿⇂	↿	3	$\frac{6}{5}\Delta_0$
4	Cr^{2+}, Mn^{3+}	↿	↿	4	$\frac{3}{5}\Delta_0$	↿⇂	↿	2	$\frac{3}{5}\Delta_0$
5	Mn^{2+}, Fe^{3+}	↿	↿	5	0	↿⇂	↿	1	$\frac{10}{5}\Delta_0$
6	Fe^{2+}, Co^{3+}, Ni^{4+}	↿⇂	↿	4	$\frac{3}{5}\Delta_0$	↿⇂	↿⇂	0	$\frac{13}{5}\Delta_0$
7	Co^{2+}, Ni^{3+}	↿⇂	↿	3	$\frac{4}{5}\Delta_0$	↿⇂	↿⇂	1	$\frac{9}{5}\Delta_0$
8	Ni^{2+}	↿⇂	↿	2	$\frac{6}{5}\Delta_0$	↿⇂	↿⇂	2	$\frac{6}{5}\Delta_0$
9	Cu^{2+}	↿⇂	↿⇂	1	$\frac{3}{5}\Delta_0$	↿⇂	↿⇂	1	$\frac{3}{5}\Delta_0$
10	Cu^+, Zn^{2+}, Ga^{3+}, Ge^{4+}	↿⇂	↿⇂	0	0	↿⇂	↿⇂	0	0

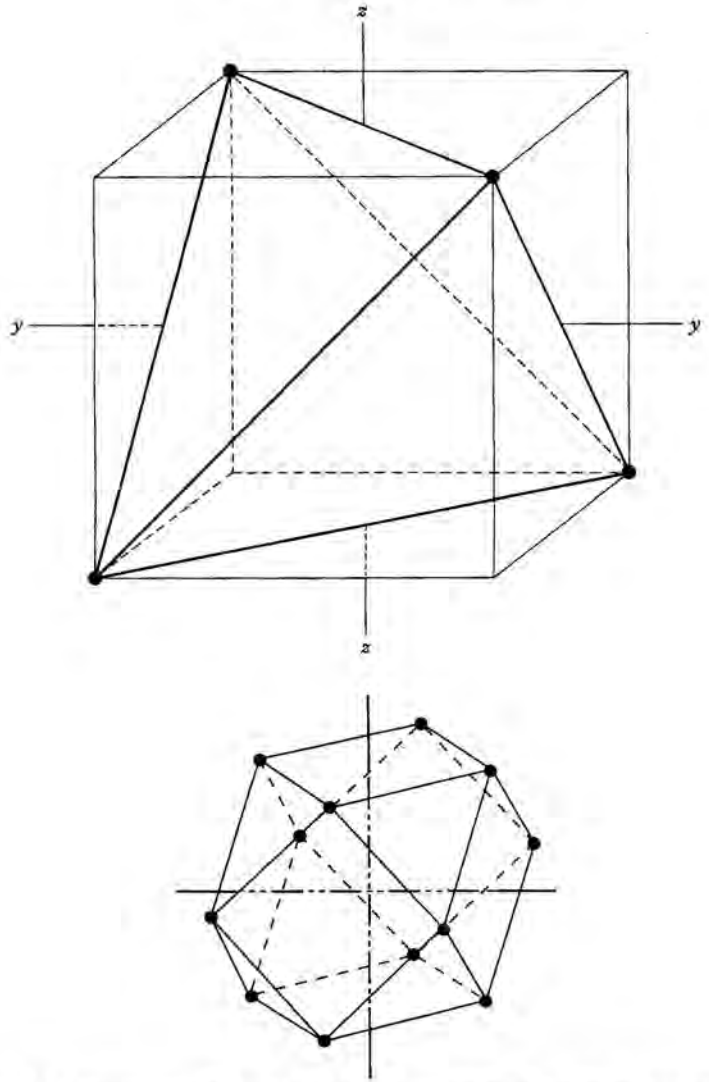

Figure 2.6 Arrangements of ligands about a transition metal ion in (*a*) tetrahedral and cubic coordinations, and (*b*) dodecahedral or cuboctahedral coordination. In tetrahedral coordination, the ligands may be regarded as lying at alternate vertices of a cube. In cubic coordination the ligands are situated on all eight vertices.

The Mn^{2+} ion, $(t_{2g})^3(e_g)^2$, formed in these processes possesses zero CFSE but has the stable electronic configuration with a maximum of five unpaired electrons spinning in the same direction. The Mn(IV) oxidation state, $(t_{2g})^3$, has a very high CFSE. Unstable cations such as Mn^{3+} may be stabilized in distorted

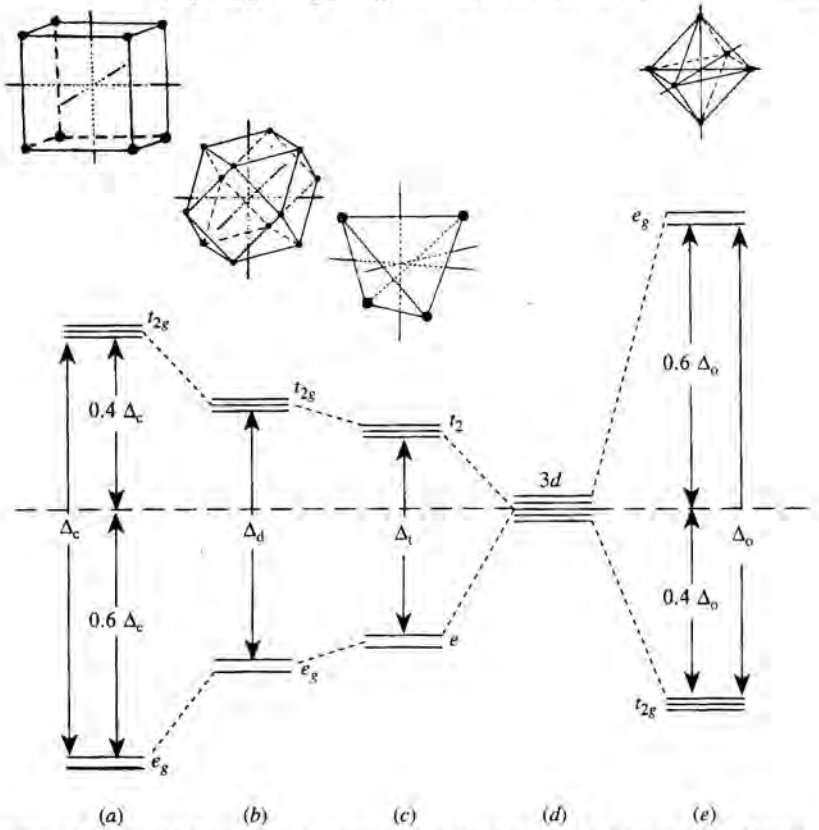

Figure 2.7 Crystal field splittings of transition metal 3*d* orbitals in (*a*) cubic (8-fold); (*b*) dodecahedral (12-fold); (*c*) tetrahedral (4-fold); (*d*) spherical; and (*e*) octahedral (6-fold) coordinations (from Burns, 1985a).

environments, however. This property, which is the result of the Jahn–Teller effect, is discussed in §2.12, §4.4.2 and §6.3.

2.6 Crystal field splittings in other coordinations

2.6.1 Tetrahedral coordination

In structures containing tetrahedral coordination sites, the ligands may be regarded as lying on alternate vertices of a cube with the transition metal ion at the centre. This arrangement is shown in fig. 2.6*a*. A tetrahedron lacks a centre of symmetry so that by group theory nomenclature the two groups of orbitals are designated by t_2 (for the d_{xy}, d_{yz} and d_{zx} orbitals) and e (for the $d_{x^2-y^2}$ and d_{z^2} orbitals) with the subscript g omitted. In tetrahedral coordination, electrons in

the t_2 orbitals are now repelled by the ligands to a greater extent than are electrons in the e orbitals. This leads to an inversion of the energy levels relative to those of a transition metal ion in octahedral coordination. The energy separation between the t_2 and e orbital energy levels is denoted by the tetrahedral crystal field splitting parameter Δ_t. Orbitals of the e group are stabilized by $0.6\Delta_t$ and the t_2 orbitals are destabilized by $0.4\Delta_t$. These relationships are shown in the energy level diagram in fig. 2.7.

Alternative electronic configurations, corresponding to high-spin and low-spin states, are theoretically possible for cations with three, four, five and six $3d$ electrons when they occupy tetrahedral sites. However, low-spin configurations are extremely unlikely because of the smaller value of the crystal field splitting in tetrahedral coordination compared to octahedral coordination discussed below. Nevertheless, the dual configurations for tetrahedral coordination are shown in table 2.3. Table 2.3 also lists the CFSE for each transition metal ion in tetrahedral coordination. Note that cations with d^2 and d^7 configurations, such as V^{3+} and Co^{2+}, respectively, acquire relatively high stabilization energies in tetrahedral coordination and might be expected to favour these sites in crystal structures such as spinel (§6.4) and staurolite (§4.4.3).

The geometries of the octahedral and tetrahedral coordination sites shown in figs 2.3 and 2.6*a* suggest that the value of the tetrahedral crystal field splitting parameter, Δ_t, will be smaller than the octahedral parameter, Δ_o, for each transition metal ion. It may be shown by simple electrostatic arguments and by group theory that

$$\Delta_t = -\frac{4}{9}\Delta_o \tag{2.7}$$

when cations, ligands, and metal-ligand distances are identical in the two coordinations. The implication of the negative sign in eq. (2.7) is that the relative stabilities of the two groups of d orbitals are reversed in the two coordinations. Thus, the d_{z^2} and $d_{x^2-y^2}$ orbitals are less stable in octahedral coordination but are the more stable group in tetrahedral coordination relative to the d_{xy}, d_{yz} and d_{zx} orbitals.

2.6.2 Cubic and dodecahedral coordinations

In body-centred cubic coordination, the eight ligands surrounding a transition metal ion lie at the vertices of a cube (cf. fig. 2.6*a*.). In one type of dodecahedral coordination site found in the ideal perovskite structure (cf. fig. 9.3), the 12 nearest-neighbour anions lie at the vertices of a cuboctahedron illustrated in fig. 2.6*b*. The relative energies of the e_g and t_{2g} orbital groups in these two centrosymmetric coordinations are identical to those of the e and t_2 orbital groups

Table 2.3. *Electronic configurations and crystal field stabilization energies of transition metal ions in tetrahedral coordination*

Number of $3d$ electrons	Cation	High-spin state				Low-spin state			
		Electronic configuration		Unpaired electrons	CFSE	Electronic configuration		Unpaired electrons	CFSE
		e	t_2			e	t_2		
0	Ca^{2+}, Sc^{3+}, Ti^{4+}			0	0			0	0
1	Ti^{3+}	↑		1	$\frac{3}{5}\Delta_t$	↑		1	$\frac{3}{5}\Delta_t$
2	Ti^{2+}, V^{3+}	↑ ↑		2	$\frac{6}{5}\Delta_t$	↑ ↑		2	$\frac{6}{5}\Delta_t$
3	V^{2+}, Cr^{3+}, Mn^{4+}	↑ ↑ ↑		3	$\frac{4}{5}\Delta_t$	⇅ ↑ ↑		1	$\frac{4}{5}\Delta_t$
4	Cr^{2+}, Mn^{3+}	↑ ↑ ↑	↑	4	$\frac{3}{5}\Delta_t$	⇅ ⇅		0	$\frac{12}{5}\Delta_t$
5	Mn^{2+}, Fe^{3+}	↑ ↑ ↑	↑ ↑	5	0	⇅ ⇅	↑	1	$\frac{10}{5}\Delta_t$
6	Fe^{2+}, Co^{3+}, Ni^{4+}	⇅ ↑	↑ ↑ ↑	4	$\frac{3}{5}\Delta_t$	⇅ ⇅	↑ ↑	2	$\frac{3}{5}\Delta_t$
7	Co^{2+}, Ni^{3+}	⇅ ⇅	↑ ↑ ↑	3	$\frac{6}{5}\Delta_t$	⇅ ⇅	↑ ↑ ↑	3	$\frac{6}{5}\Delta_t$
8	Ni^{2+}	⇅ ⇅ ↑	↑ ↑	2	$\frac{4}{5}\Delta_t$	⇅ ⇅	↑ ↑	2	$\frac{4}{5}\Delta_t$
9	Cu^{2+}	⇅ ⇅ ↑	↑ ↑	1	$\frac{3}{5}\Delta_t$	⇅ ⇅	↑ ↑	1	$\frac{3}{5}\Delta_t$
10	Cu^{+}, Zn^{2+}, Ga^{3+}, Ge^{4+}	⇅ ⇅	⇅ ⇅	0	0	⇅ ⇅	⇅ ⇅	0	0

in tetrahedral coordination, so that the electronic configurations and relative crystal field stabilization summarized in table 2.3 are also applicable to transition metal ions in cubic and dodecahedral coordinations. The cubic crystal field splitting parameter, Δ_c, however, is larger than Δ_t. Electrostatic and group theory arguments, again based on the same cation, similar ligands and identical metal-ligand distances in the two coordinations, lead to the following relationships between the cubic and octahedral crystal field splitting parameters

$$\Delta_c = -\frac{8}{9}\Delta_o \,. \tag{2.8}$$

Similarly, for dodecahedral (Δ_d) and octahedral coordinations,

$$\Delta_d = -\frac{1}{2}\Delta_o \,. \tag{2.9}$$

These relative crystal field splittings are portrayed schematically in fig. 2.7.

2.6.3 *Other regular coordination environments*

Several regular, non-distorted coordination environments providing coordination numbers ranging from 3 to 12 exist in chemical compounds of the transition elements, many being represented in mineral crystal structures discussed in later chapters. Relative energy levels corresponding to identical metal–ligand distances in each of these coordination environments are summarized in table 2.4, together with mineralogical examples.

2.7 The 10 *Dq* parameter

In an octahedral coordination site, the electrostatic field produced by the six ligands (represented as point negative charges and interacting with an electron in the vicinity of the central cation) is expressed by the potential

$$V_{oct} = \frac{6Z_L e}{R} + \frac{35Z_L e}{4R^5}\left(x^4 + y^4 + z^4 - \frac{3}{5}r^4\right), \tag{2.10}$$

where $(Z_L e)$ is the charge on the ligands separated by a distance R from the cation, and x, y, z and r are the polar coordinates of the electron (fig. 2.1). The first and largest term of this expression, $(6Z_L e/R)$, is the constant potential contributed by electrons of the argon core (table 2.1). This term contributes the

Table 2.4. *Relative energy levels of 3d orbitals in crystal fields of different symmetries**

Coordination number	Symmetry of site	d_{z^2}	$d_{x^2-y^2}$	d_{xy}	d_{xz}	d_{yz}	Examples
3	triangular	− 0.321	0.546	0.546	− 0.386	− 0.386	(carbonate ion)
4	tetrahedral	− 0.267	− 0.267	+ 0.178	+ 0.178	+ 0.178	spinel
4	square planar	− 0.528	1.228	0.228	− 0.464	− 0.464	gillespite, eudialyte
5	trigonal bipyramid	0.707	− 0.082	− 0.082	− 0.272	− 0.272	hibonite, andalusite
5	square pyramid	0.086	0.914	− 0.086	− 0.457	− 0.457	S_N1 reactions, eudialyte
6	octahedral	0.600	0.600	− 0.400	− 0.400	− 0.400	many Fe–Mg and Al silicates
6	trigonal prism	0.096	− 0.584	− 0.584	0.536	0.536	troilite
7	pentagonal bipyramid	0.493	0.282	0.282	− 0.528	− 0.528	S_N2 reactions
8	cube	− 0.534	− 0.534	0.356	0.356	0.356	garnet
8	square antiprism	− 0.534	− 0.089	− 0.089	0.356	0.356	diopside M2
12	dodecahedron (cuboctahedron)	0.300	0.300	− 0.200	− 0.200	− 0.200	perovskite

*Expressed as fractions of the octahedral crystal field splitting parameter, Δ_o.

major share to thermodynamic properties of a transition metal compound and influences the baricentre of the 3*d* orbital energy levels (fig. 2.4). However, since the $(6Z_Le/R)$ term is spherically symmetrical, it does not participate in the splitting of the 3*d* orbital energy levels. Hence, it is usually neglected in crystal field theory, being unimportant when *energy differences* are being considered.

The second term in eq. (2.10) may be expressed by

$$V'_{oct} = D\,(x^4 + y^4 + z^4 - \frac{3}{5}r^4)\,, \tag{2.11}$$

where constant, D, is given by

$$D = \frac{35Z_Le}{4R^5}\,. \tag{2.12}$$

The potential, V'_{oct}, interacting with 3*d* electrons in the t_{2g} and e_g orbitals leads to the following expressions for their respective energies:

$$E(t_{2g}) = -4\,Dq \tag{2.13}$$

and

$$E(e_g) = +6\,Dq\,, \tag{2.14}$$

where

$$q = \frac{2e}{105}\int_0^\infty r_{3d}^2(r)r^4r^2\mathrm{d}r = \frac{2e<r^4>}{105}\,, \tag{2.15}$$

so that the energy difference between the t_{2g} and e_g orbitals is

$$E(e_g) - E(t_{2g}) = 10\,Dq\,, \tag{2.16}$$

which is equivalent to the crystal field splitting parameter Δ_o.

In eq. (2.15), $<r^4>$ is the mean value of the fourth power of the radial distance of a 3*d* orbital from the nucleus. Although accurate estimates of $<r^4>$ are not yet available, its value is assumed to be approximately constant for cations of similar valence in the same transition series. Combining eqs (2.12) and (2.15), the product of D and q is $(Z_Le^2/6R^5)<r^4>$, so that

$$\Delta_o = 10Dq = \frac{Z_Le^2}{6R^5}<r^4> = \frac{Q<r^4>}{R^5}\,, \tag{2.17}$$

where Q is a constant.

The inverse fifth-power dependency of crystal field splitting on metal–oxygen distance expressed in eq. (2.17) is of fundamental importance in transition metal geochemistry, particularly in mineral physics at high pressures and interpretations of visible to near-infrared spectra of minerals. Thus, the $\Delta \propto R^{-5}$ relationship, eq. (2.17), is referred to frequently in later chapters.

2.8 Evaluation of Δ or 10 *Dq*

The magnitude of the crystal field splitting parameter, Δ or 10 *Dq*, may be estimated by two independent methods. The conventional way for evaluating Δ is from positions of absorption bands in visible-region spectra of transition metal compounds. The energy required to excite an electron from one 3*d* orbital to another 3*d* orbital of higher energy corresponds to radiation in the visible and near-infrared regions of the electromagnetic spectrum. Absorption of visible radiation by such intra-electronic transitions is the most common cause of colour in transition metal compounds and minerals. Accordingly, crystal field spectra are commonly referred to as optical spectra, alluding to colour variations of transition metal-bearing phases that are visible to the eye. Crystal field spectra are also called *d–d* spectra and, more generally, electronic absorption spectra, although the latter designation also includes interelectronic or charge transfer transitions between adjacent ions. The theory of crystal field spectra is described in chapter 3, while applications to colours of minerals are discussed in chapter 4.

The second method for estimating the value of Δ is from plots of thermodynamic data for series of similar compounds of transition elements. This method is discussed further in chapter 7.

2.9 Factors influencing values of Δ or 10 Dq

Certain generalizations may be made about factors that influence the magnitude of Δ or 10 *Dq*, values of which depend on individual cations, types of anions or ligands, interatomic distances, pressure and temperature variations, and symmetries of ligand environments.

2.9.1 Type of cation

Values of Δ_o are generally higher for trivalent cations than for corresponding divalent ions. This is demonstrated by the data summarized in table 2.5 for divalent and trivalent transition metal ions in simple oxide structures and in hydrated environments. For example, Δ_o values for Fe^{2+} and Fe^{3+} ions in aqueous solution are 10,400 cm^{-1} and 13,700 cm^{-1}, respectively.

There is a general sequence of Δ_o values which increase in the order

$$Mn^{2+} < Ni^{2+} < Co^{2+} < Fe^{2+} < V^{2+} < Fe^{3+} < Cr^{3+} < V^{3+} < Co^{3+} < Mn^{4+}. \quad (2.18)$$

This sequence is particularly well characterized for fluoride complexes of high-spin cations of the first-series transition elements (Allen and Warren, 1971). Moreover, between successive transition metal series, values of Δ_o increase by about thirty to fifty per cent. For example, in hydrated cations of the first and second transition series, Δ_o for $[Cr(H_2O)_6]^{3+}$ and $[Mo(H_2O)_6]^{3+}$ are 17,400 cm^{-1} and 26,110 cm^{-1}, respectively.

2.9.2 Type of ligand

Ligands coordinated to transition metal ions may also be arranged in order of increasing Δ. This order is called the spectrochemical series, reflecting colour variations in chemical compounds of individual cations with different ligands. Thus, for Cr^{3+} and Co^{3+} cations in octahedral coordination with different ligands, the order of increasing Δ_o is

$$I^- < Br^- < Cl^- < SCN^- < F^- < \text{urea} = OH^- < CO_3^{2-} = \text{oxalate} < O^{2-} < H_2O < \text{pyridine} < NH_3 < \text{ethylene diamene} < SO_3^{2-} < NO_2^- < HS^- < S^{2-} < CN^-. \quad (2.19)$$

Such an order is difficult to rationalize in terms of electrostatic energies embodied in the simple point-charge model of crystal field theory. For example, the charged O^{2-} anion precedes the dipolar H_2O molecule in the spectrochemical series. Note that the spectrochemical series differs from the nephelauxetic series discussed in chapter 11 (eq. 11.6), which is a measure of the degree of covalent bonding.

Transition metal ions with $3d^4$ to $3d^7$ configurations in coordination with ligands at the beginning of the spectrochemical series generally have high-spin configurations, whereas low-spin states exist in complexes with ligands at the end of the series. Thus, fluoride compounds of the first transition series contain cations in high-spin states, whereas low-spin states exist in cyanide complexes. The crossover point from high-spin to low-spin configuration varies from one cation to another, and may be ascertained from magnetic susceptibility measurements, interatomic distances in crystal structure refinements and information from spectroscopic techniques such as X-ray photoelectron (XPS), X-ray absorption (EXAFS, XANES) and Mössbauer spectroscopies. Most cations of the first transition series have high-spin configurations in oxide structures at

Table 2.5. *Crystal field splittings in transition metal-bearing oxides*

Electronic Structure	Cation		Electronic configuration	Δ corundum (cm^{-1})	Δ periclase (cm^{-1})	Δ aqueous (cm^{-1})	CFSE of hexahydrate (Δ_o)	(cm^{-1})	(kJ/g.ion)	Pairing energy* (cm^{-1})
$3d^0$	Sc^{3+}	Ti^{4+}	[Ar]							
$3d^1$	Ti^{3+}		$(t_{2g})^1$	19,100	11,360	18,950	$0.4\Delta_o$	= 7,580	= −90.7	
$3d^2$	V^{3+}		$(t_{2g})^2$	18,730		19,100	$0.8\Delta_o$	= 15,280	= −182.8	
$3d^3$		V^{2+}	$(t_{2g})^3$			12,600	$1.2\Delta_o$	= 15,120	= −180.9	
$3d^3$	Cr^{3+}		$(t_{2g})^3$	18,150	16,200	17,400	$1.2\Delta_o$	= 20,880	= −249.9	
$3d^3$		Mn^{4+}	$(t_{2g})^3$			21,000				
hs $3d^4$	Cr^{2+}		$(t_{2g})^3(e_g)^1$			13,900	$0.6\Delta_o$	= 8,340	= −99.8	20,425
hs $3d^4$	Mn^{3+}		$(t_{2g})^3(e_g)^1$	19,370		21,000	$0.6\Delta_o$	= 12,600	= −150.8	25,215
hs $3d^5$	Mn^{2+}		$(t_{2g})^3(e_g)^2$			7,800	0	0	0	23,825
hs $3d^5$	Fe^{3+}		$(t_{2g})^3(e_g)^2$	14,300		13,700	0	0	0	29,875
hs $3d^6$	Fe^{2+}		$(t_{2g})^4(e_g)^2$		10,200	9,400	$0.4\Delta_o$	= 3,760	= −45.0	19,150
ls $3d^6$	Co^{3+}		$(t_{2g})^6$			18,600	$2.4\Delta_o$	= 44,640	= −534.2	23,625
hs $3d^7$	Co^{2+}		$(t_{2g})^5(e_g)^2$	12,300	9,000	9,300	$0.8\Delta_o$	= 7,440	= −89.1	20,800
ls $3d^7$	Ni^{3+}		$(t_{2g})^6(e_g)^1$	18,000						
$3d^8$		Ni^{2+}	$(t_{2g})^6(e_g)^2$	10,700	8,500	8,500	$1.2\Delta_o$	= 10,200	= −122.1	
$3d^9$		Cu^{2+}	$(t_{2g})^6(e_g)^3$			13,000	$0.6\Delta_o$	= 7,800	= −93.3	
$3d^{10}$	Zn^{2+}	Ga^{3+}	Ge^{4+} $(t_{2g})^6(e_g)^4$							

* Pairing energies for high-spin (hs) to low-spin (ls) configurations in field-free cations are from Huheey (1983), p.380. The values are 15–30 % smaller when cations are chemically bound in coordination sites as a result of the nephelauxetic effect (§11.2.3).

atmospheric pressures. The Co^{3+} and Ni^{3+} ions are exceptions, however, and usually have low-spin configurations $(t_{2g})^6$ and $(t_{2g})^6(e_g)^1$, respectively, in oxide structures at atmospheric pressure.

In many transition metal-bearing minerals, oxygen is the most common ligand coordinated to cations in silicates, oxides, carbonates, phosphates and sulphates, for example. However, the oxygen bond-type varies from free O^{2-} anions in oxides and some silicates (e.g., Al_2SiO_5 polymorphs, epidote, wadsleyite or β–Mg_2SiO_4), to OH^- ions in oxyhydroxides and many silicates (e.g., amphiboles, micas, epidote, tourmaline), to non-bridging Si–O^- in most silicates (e.g., garnets, olivines, pyroxenes), to bridging Si–O–Si atoms in pyroxenes and amphiboles, to H_2O in a variety of hydrated minerals. Such differences of oxygen bond-type may produce small variations of Δ and influence the visible-region spectra, colours of rock-forming minerals and cation site occupancies in crystal structures. Such effects are discussed in later chapters.

2.9.3 Interatomic distance

The value of Δ is influenced by the distances between the transition metal and surrounding ligands, as formulated in eq. (2.17). This inverse fifth-power relationship indicates that Δ changes rapidly with variations of metal-ligand distances. For example, in a ferromagnesian silicate such as olivine, $(Mg,Fe)_2SiO_4$, the replacement of smaller Mg^{2+} ions (octahedral ionic radius, $r_{oct} = 72$ pm) by larger Fe^{2+} ions ($r_{oct} = 77$ pm), which causes a decrease of lattice parameters and bond-lengths in the crystal structure, leads to a decrease of Δ in the crystal field spectra of forsterite-fayalite series (§5.4.2.3). Ruby is coloured red, and not green as eskolaite (Cr_2O_3) is, due to the compression of Cr^{3+} (61 pm) replacing Al^{3+} ions (57 pm) in the corundum structure.

2.9.4 Pressure

At elevated pressures, the inverse fifth-power relationship expressed by eq. (2.17) leads to

$$\frac{\Delta_P}{\Delta_0} = \left(\frac{R_0}{R_P}\right)^5 , \tag{2.20}$$

where Δ_P, Δ_0 and R_P, R_0 are the crystal field splittings and average cation to oxygen distances for a transition metal ion in a mineral structure at high and ambient pressures, respectively. Since $R = 1/V^3$, where V is volume,

$$\Delta \propto V^{-5/3}, \text{ or } \ln \Delta = -\frac{5}{3} \ln V . \tag{2.21}$$

Differentiation of eq. (2.21) gives

$$\frac{d\Delta}{\Delta} = \frac{5}{3}\frac{dV}{V} = \frac{5}{3}\frac{d\rho}{\rho} = \frac{5}{3}\frac{dP}{\kappa} , \tag{2.22}$$

where ρ is the density and κ the bulk modulus or incompressibility of the coordination polyhedron. κ is related to the compressibility, β, of the coordination polyhedron by

$$\kappa = \frac{1}{\beta} = -V\frac{dP}{V} , \tag{2.23}$$

Rewriting eq. (2.22) gives

$$\frac{d\Delta}{dP} = \frac{5}{5}\frac{\Delta}{\kappa} , \tag{2.24}$$

from which site incompressibilities or polyhedral bulk moduli of transition metal-bearing minerals may be estimated from Δ derived from high pressure crystal field spectral measurements. This application of high pressure spectroscopy is discussed in chapter 9 (§9.6).

Another application of eq. (2.20) concerns spin-pairing transitions in cations with $3d^4$ to $3d^7$ configurations. According to eq. (2.17), a small contraction of metal-ligand distance caused, for example, by increased pressure leads to a large increase in Δ. Such sensivity of Δ to contraction of bond lengths raises the possibility of spin-pairing transitions; that is, a change from a high-spin to low-spin configuration, in some transition metal ions. Such pressure-induced transitions are discussed further in chapter 9 in connection with possible electronic-induced phase changes in minerals deep in the Lower Mantle (§9.7).

2.9.5 Temperature

The temperature variation of Δ may be expressed by

$$\frac{\Delta_T}{\Delta_0} = \left(\frac{V_0}{V_T}\right)^{5/3} = \left[1 = \alpha(T - T_0)\right]^{-5/3} , \tag{2.25}$$

where Δ_T, Δ_0 and V_T, V_0 are crystal field splittings and molar volumes at elevated temperatures (T) and room temperature (T_0), respectively; α is the volume coefficient of thermal expansion. Generally, $V_T > V_0$, so that decreased values of Δ might be expected at elevated temperatures. However, other factors contribute to temperature-induced variations of absorption bands and some of these are discussed in chapters 3 and 10 (§3.9.4 and §10.7).

2.9.6 Symmetry of the ligand environment

As noted earlier, Δ depends on the symmetry of the ligands surrounding a transition metal ion. The relationships expressed in eqs (2.7), (2.8) and (2.9) for crystal field splittings in octahedral, tetrahedral, body-centred cubic and dodecahedral coordinations are summarized in eq. (2.26)

$$\Delta_o:\Delta_c:\Delta_d:\Delta_t = 1:-\frac{8}{9}:-\frac{1}{2}:-\frac{4}{9} \qquad (2.26)$$

and are shown schematically in fig. 2.7. These splittings which apply to regular or high-symmetry coordination polyhedra are further modified in non-cubic coordination environments such as those listed in table 2.4, as well as distorted coordination sites described later (§2.11).

2.10 Values of CFSE

The data in table 2.5 illustrate some of the generalizations enunciated in §2.9 regarding relative values of the crystal field splitting parameter, Δ. Crystal field stabilization energies (CFSE's) estimated from the Δ_o values of the hexahydrated ions are also calculated in table 2.5. The spectrum of Cr^{3+} in aqueous solution, for example, yields a value for Δ_o of 17,400 cm^{-1}. The CFSE of the Cr^{3+} ion, $(t_{2g})^3$, is $1.2\Delta_o$, or 20,880 cm^{-1}. This may be converted to joules by applying the conversion factor, 1 cm^{-1} = 11.966 J (see Appendix 8) giving –249.9 kJ/(g. ion) as the CFSE of Cr^{3+} in aqueous solution. The corresponding CFSE for Cr^{3+} in the corundum structure is (1.2 x 18,150 x 11.966) or –260.6 kJ/(g.ion). In Cr^{3+}–doped periclase the CFSE is about –233 kJ/(g.ion). These values for octahedrally coordinated Cr^{3+} ions, which are among the highest for transition metal ions with high-spin configurations in oxide structures, profoundly influence the geochemical behaviour of chromium (e.g., §8.5.3). Similarly, the unique configuration of low-spin Co^{3+}, $(t_{2g})^6$, also results in this trivalent cation having a very high CFSE, which has important consequences in sedimentary geochemistry (§8.7.5). Among divalent cations, Ni^{2+} has the highest CFSE. Such a relatively high electronic stability in octahedral sites has important implications in crystal chemical and geochemical properties of nickel (e.g., §8.5). The relatively high CFSE values for Cr^{3+}, Co^{3+} and Ni^{2+} contrast to the zero CFSE's of Mn^{2+} and Fe^{3+} resulting from their unique high-spin $3d^5$ configurations. Cations with zero $3d$ electrons (for example, Mg^{2+}, Ca^{2+}, Sc^{3+}, Ti^{4+}) and ten $3d$ electrons (for example, Cu^{1+}, Zn^{2+}, Ga^{3+}, Ge^{4+}) also have zero CFSE. Such differences of relative CFSE's profoundly influence the crystal chemical and geochemical properties of the cations, and are highlighted in later chapters.

2.11 Crystal fields in non-cubic environments

The discussion so far has been concerned with crystal field splittings within transition metal ions when they are surrounded by identical ligands in regular octahedral, tetrahedral, cubic and dodecahedral coordinations. Such high-symmetry coordination sites possibly exist in aqueous solutions, fused salts and silicate melts. However, coordination polyhedra are rarely so regular in crystal structures of most transition metal-bearing phases. In silicate minerals in particular, oxygen atoms frequently occur at the vertices of distorted polyhedra, and metal-oxygen distances are not identical within a coordination site (see Appendix 7). Furthermore, ligands may not be identical or equivalent in the coordination polyhedra. Thus, certain silicates (e.g., micas, amphiboles, tourmaline, topaz) contain appreciable amounts of OH^-, F^- and Cl^- anions, in addition to oxygens linked to silicon atoms, surrounding the cation coordination sites. As noted earlier (§2.9.2), the bond-type of oxygen ligands may vary within a site. Thus, minor differences in crystal field splittings may occur between O^{2-}, OH^-, Si–O^-, Si–O–Si, and H_2O groups. These factors, and their impact on cation site occupancies, are discussed in §6.8.

Further resolution of the $3d$ orbital energy levels takes place within a transition metal ion when it is located in a low-symmetry site, including non-cubic coordination environments listed in table 2.4 and polyhedra distorted from octahedral or cubic symmetries. As a result, the simple crystal field splitting parameter, Δ, loses some of its significance when more than one energy separation occurs between $3d$ orbitals of the cation.

2.12 The Jahn–Teller effect

Distortions of coordination polyhedra in the crystal structures of certain transition metal compounds are to be expected for theoretical reasons known as the Jahn–Teller effect. Jahn and Teller (1937) proved that if the ground state or lowest energy level of a molecule is degenerate, it will distort spontaneously to a lower symmetry so as to remove the degeneracy and make one energy level more stable. For example, if one of the $3d$ orbitals is completely empty or completely filled while another of equal energy is only half-filled, the environment about the transition metal ion is predicted to distort spontaneously to a different geometry in which a more stable electronic configuration is attained by making the half-filled orbital lower in energy.

The proof of the Jahn–Teller theorem lies in group theory and quantum mechanics. However, the origin of the distorting forces may be illustrated by considering the Mn^{3+} ion in octahedral coordination with oxygen. The Mn^{3+} ion has the high-spin configuration, $(t_{2g})^3(e_g)^1$, in which each t_{2g} orbital is occupied by one $3d$ electron and the fourth electron may occupy either the $d_{x^2-y^2}$ or d_{z^2} orbital (fig. 2.8). If the four oxygen atoms in the x–y plane move towards the central Mn^{3+} ion and, simultaneously, the two oxygen atoms along the z axis move away, the solitary e_g electron will favour the d_{z^2} orbital in which repulsion by the oxygen ions is smaller than in the $d_{x^2-y^2}$ orbital. Therefore, the e_g orbital group is separated into two energy levels with the d_{z^2} orbital becoming the the more stable. At the same time the t_{2g} orbital group is split into two energy levels, the d_{xz} and d_{yz} orbitals becoming more stable than the d_{xy} orbital. The four Mn–O distances in the x–y plane become smaller than the two distances along the z axis. The resulting coordination polyhedron and relative energies of the $3d$ orbitals are shown schematically in fig. 2.8*a*.

A converse situation exists whereby the two oxygen ions along the z axis may move closer to the Mn^{3+} ion (fig. 2.8*b*). This results in the stabilization of the $d_{x^2-y^2}$ orbital relative to the d_{z^2} orbital, and shorter Mn–O distances along the z axis compared to the x–y plane. In either of the tetragonally distorted environments shown in fig. 2.8 the Mn^{3+} ion becomes more stable relative to a regular octahedral coordination site. In most minerals, however, the Mn^{3+} ion occurs in an axially elongated octahedron (see table 6.1).

Transition metal ions most susceptible to large Jahn–Teller distortions in octahedral coordination in oxide structures are those with $3d^4$, $3d^9$ and low-spin $3d^7$ configurations, in which one or three electrons occupy e_g orbitals. Thus, the Cr^{2+} and Mn^{3+}, Cu^{2+}, and Ni^{3+} ions, respectively, are stabilized in distorted environments, with the result that compounds containing these cations are frequently distorted from type-structures. Conversely, these cations may be stabilized in distorted sites already existing in mineral structures. Examples include Cr^{2+} in olivine (§8.6.4) and Mn^{3+} in epidote, andalusite and alkali amphiboles (§4.4.2). These features are discussed further in chapter 6.

Uneven electron distributions also exist in the t_{2g} orbitals of some transition metal ions, including those with $3d^1$, $3d^2$, and high-spin $3d^6$ and $3d^7$ configurations, suggesting that the t_{2g} orbital group may also undergo Jahn–Teller splitting. However, van Vleck (1939) proved and examples have confirmed that Jahn–Teller distortions are small when there is degeneracy in the t_{2g} orbital group. For example, the lower-level splittings of t_{2g} orbitals, δ_1, depicted in fig. 2.8 are about 10 cm^{-1} to 100 cm^{-1} when cations such as Ti^{3+}, V^{3+}, Fe^{2+} and Co^{2+} occur in structures (e.g., MgO) and environments (e.g., aqueous solutions) providing regular octahedral coordination sites. In contrast, the upper-level splittings of e_g orbitals, δ_3, are much larger and may be of the order of several thousand wave number units. In some structures accommodating Mn^{3+}, Cr^{2+} and Cu^{2+} ions in octahedral sites, energy separations between the d_{z^2} and $d_{x^2-y^2}$ orbitals (δ_3) may be comparable to Δ_o values.

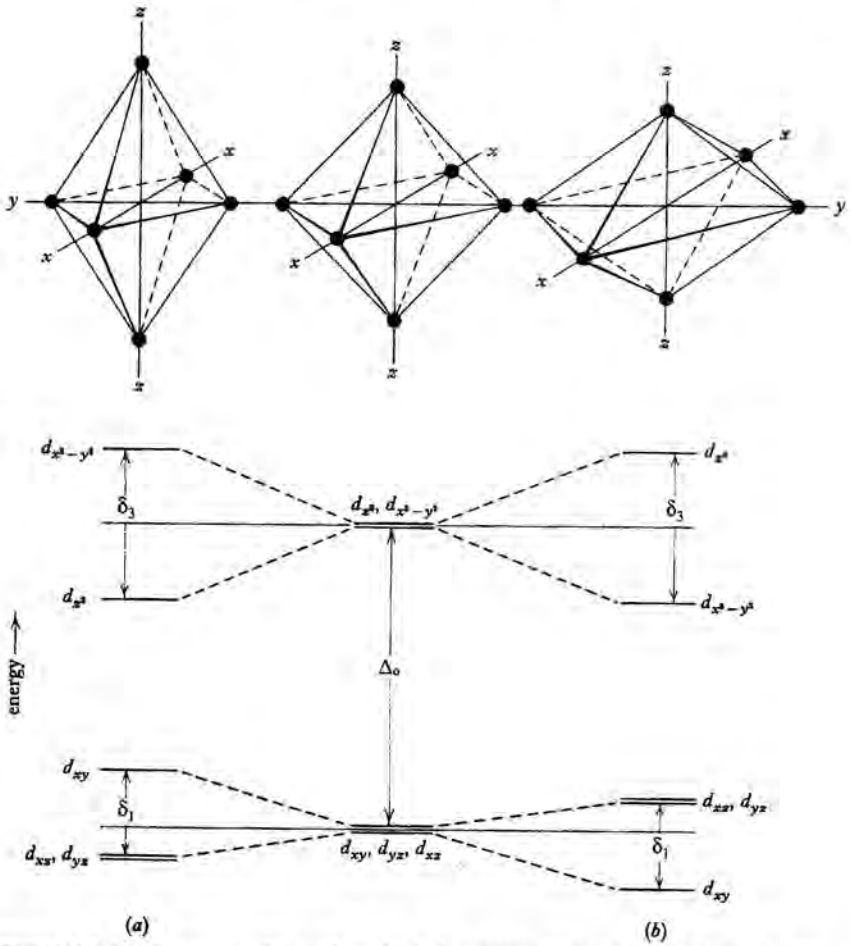

Figure 2.8 Arrangements of ligands and relative energy levels of $3d$ orbitals of transition metal ions in tetragonally distorted octahedral sites. (*a*) Octahedral site elongated along one of the tetrad axes (z axis); (*b*) octahedral site compressed along one of the tetrad axes (z axis). Ligand arrangements and energy levels for a regular octahedral site are shown for reference.

Jahn–Teller distortions are also predicted for certain transition metal ions in tetrahedral coordination. The electronic configurations predicted to undergo no Jahn–Teller distortions are the high-spin $3d^2$, $3d^5$, $3d^7$ and low-spin $3d^4$

cations. However, ions having $3d^3$, $3d^4$, $3d^8$ and $3d^9$ configurations (e.g., Cr^{3+}, Mn^{3+}, Ni^{2+} and Cu^{2+}) are predicted to be more stable in distorted sites if they were to occur in tetrahedral coordination. The Cr^{3+} and Mn^{3+} ions rarely, if ever, occur in tetrahedral coordination, due to their high octahedral CFSE's.

Some important corollaries to the Jahn–Teller theorem should be noted. First, the theorem only predicts that distortion must occur whenever an ion possesses a degenerate electronic configuration. It does not give any indication of the amount or geometrical nature of the the distortion, apart from retaining a centre of symmetry, if present. For example, it is impossible to predict whether the environment about the Mn^{3+} ion will distort to an axially elongated (fig. 2.8*a*) or axially compressed (fig. 2.8*b*) octahedron. The position of a transition metal ion in a crystal structure is controlled by several factors one of which is the Jahn–Teller force. The nature and a probable Jahn–Teller distortion of a coordination site may be ascertained only from experiments using such techniques as X-ray, electron, and neutron diffraction, crystal field spectra, X-ray absorption spectra, electron paramagnetic resonance and nuclear magnetic resonance measurements. In fact, most Mn^{3+}–bearing compounds and minerals are observed to accommodate trivalent manganese in axially elongated octahedra (table 6.1). Copper minerals, on the other hand, often contain Cu^{2+} ions bonded to oxygen ligands in square planar coordination (table 6.1).

A second consequence of the Jahn–Teller theorem is that it predicts splittings of energy levels will occur when cations exist in transient excited states. The simplest example is Ti^{3+}, $3d^1$, in which the single $3d$ electron occupies a t_{2g} orbitals. When this electron is excited into an empty e_g orbital by light in the visible region, the d_{z^2} and $d_{x^2-y^2}$ orbitals become separated into two energy levels during the very short lifetime of the electronic transition (10^{-15} s). This phenomenon, known as dynamic Jahn–Teller splitting, has important implications and leads to asymmetric spectrum profiles in the crystal field spectra of some transition metal ions, notably Fe^{2+} and Ti^{3+}. Examples are discussed in chapter 3 (§3.9).

2.13 Stabilization energies in distorted coordination sites

As noted in §2.11, ligands forming high-symmetry coordination polyhedra (i.e., regular octahedra, tetrahedra, cubes and dodecahedra) about central transition metal ions are rare. Such highly idealized coordinations, nevertheless, do exist in the periclase (octahedra), cubic perovskite (octahedra, dodecahedra) and spinel (tetrahedra) structures. The more important rock-forming oxide and silicate minerals provide, instead, low-symmetry coordination environments. These include trigonally distorted octahedra in the corundum, spinel and garnet structures, the rhombic distorted dodecahedra in garnets, and a wide variety of deformed octahedra and six-coordinated sites in ferromagnesian silicates, including the olivine, pyroxene and amphibole structures illustrated later (figs 5.8, 5.16 and 5.18; see also Appendix 7). Non-cubic symmetry also exists in coordination sites when different arrangements of oxygen ligands surround a cation, such as Si–O^- and OH^- anions in amphiboles and micas. In micas, for example, the *trans*–M1 and *cis*–M2 sites differ with respect to the positions of the two hydroxyl ions in the coordination polyhedron surrounding the cation in octahedral sites (fig. 5.21). A similar distinction exists between the *trans*–M3 and *cis*–M1 sites in the amphibole structure (fig. 5.18). The occurrence of transition metal ions in such low-symmetry sites leads to further resolution of the $3d$ orbitals into additional energy levels which influence electronic configurations and modify estimates of CFSE's.

For example, in a tetragonally distorted octahedron elongated along the tetrad axis, such as that shown in fig. 2.8a, the t_{2g} and e_g orbital groups are each resolved into two additional energy levels. The energy separations between the resolved orbitals of the t_{2g} and e_g groups are denoted by δ_1 and δ_3 respectively. If the split energy levels obey centre of gravity rules about the t_{2g} and e_g baricentres, the d_{xz} and d_{yz} orbitals are stabilized by $\delta_1/3$ and the d_{z^2} orbital by $\delta_3/2$, respectively. In a site compressed along the tetrad axis, on the other hand, the d_{xy} and $d_{x^2-y^2}$ orbitals are the more stable ones of the t_{2g} and e_g groups, respectively. In table 2.6 are listed the stabilization energies of each transition metal ion in regular and tetragonally distorted octahedral sites, together with the configurations of the most stable site predicted for each transition metal ion. Ions that are most stable in regular octahedral sites are those with $3d^3$, $3d^8$ and low-spin $3d^6$ configurations. The remaining cations attain increased stability in distorted coordination sites.

Transition metal ions in crystal structures may also occur in coordination sites possessing symmetries other than regular and tetragonally distorted octahedral and tetrahedral. Some of the geometries of low-symmetry coordination polyhedra occurring in silicates include trigonally distorted octahedra, orthorhombic and skewed octahedra, distorted cubes, square planar and, rarely, linear and square antiprisms. Transition metal ions in each of these coordination sites have their $3d$ orbitals split into several energy levels and examples are shown schematically in fig. 2.9. In each configuration, the z electronic axis, by convention, is designated as the axis of highest symmetry and usually corresponds to the axis of distortion of an octahedron. Other examples of distorted coordination polyhedra are portrayed in later chapters.

Distorted coordination sites in oxides and silicates have several important consequences in transition metal geochemistry and crystal chemistry. First,

Table 2.6. *Stabilization energies of transition metal ions in tetragonally distorted octahedral sites in oxides*

Electronic structure		Cation			Electronic configuration	Stabilization energy: Octahedron elongated along tetrad axis	Stabilization energy: Octahedron compressed along tetrad axis	Configuration of the most stable six-coordinated site
	$3d^0$	Ca^{2+}	Sc^{3+}	Ti^{4+}	[Ar]	-	-	octahedron
	$3d^1$		Ti^{3+}	V^{4+}	$(t_{2g})^1$	$\frac{2}{5}\Delta_o + \frac{1}{3}\delta_1$	$\frac{2}{5}\Delta_o + \frac{2}{3}\delta_1$	compressed octahedron
	$3d^2$		V^{3+}	Cr^{4+}	$(t_{2g})^2$	$\frac{4}{5}\Delta_o + \frac{2}{3}\delta_1$	$\frac{4}{5}\Delta_o + \frac{1}{3}\delta_1$	elongated octahedron
	$3d^3$	V^{2+}	Cr^{3+}	Mn^{4+}	$(t_{2g})^3$	$\frac{6}{5}\Delta_o$	$\frac{6}{5}\Delta_o$	octahedron
hs	$3d^4$	Cr^{2+}	Mn^{3+}		$(t_{2g})^3(e_g)^1$	$\frac{2}{5}\Delta_o + \frac{1}{2}\delta_3$	$\frac{2}{5}\Delta_o + \frac{1}{2}\delta_3$	deformed octahedron
ls	$3d^4$	Cr^{2+}	Mn^{3+}		$(t_{2g})^4$	$\frac{8}{5}\Delta_o + \frac{1}{3}\delta_1$	$\frac{8}{5}\Delta_o + \frac{2}{3}\delta_1$	compressed octahedron
hs	$3d^5$	Mn^{2+}	Fe^{3+}		$(t_{2g})^3(e_g)^2$	0	0	octahedron
ls	$3d^5$	Mn^{2+}	Fe^{3+}		$(t_{2g})^5$	$2\Delta_o + \frac{2}{3}\delta_1$	$2\Delta_o + \frac{1}{3}\delta_1$	elongated octahedron
hs	$3d^6$	Fe^{2+}	Co^{3+}		$(t_{2g})^4(e_g)^2$	$\frac{2}{5}\Delta_o + \frac{1}{3}\delta_1$	$\frac{2}{5}\Delta_o + \frac{2}{3}\delta_1$	compressed octahedron
ls	$3d^6$	Fe^{2+}	Co^{3+}		$(t_{2g})^6$	$\frac{12}{5}\Delta_o$	$\frac{12}{5}\Delta_o$	octahedron
hs	$3d^7$	Co^{2+}	Ni^{3+}		$(t_{2g})^5(e_g)^2$	$\frac{4}{5}\Delta_o + \frac{2}{3}\delta_1$	$\frac{4}{5}\Delta_o + \frac{1}{3}\delta_1$	elongated octahedron
ls	$3d^7$	Co^{2+}	Ni^{3+}		$(t_{2g})^6(e_g)^1$	$\frac{9}{5}\Delta_o + \frac{1}{2}\delta_3$	$\frac{9}{5}\Delta_o + \frac{1}{2}\delta_3$	deformed octahedron
	$3d^8$	Ni^{2+}			$(t_{2g})^6(e_g)^2$	$\frac{6}{5}\Delta_o$	$\frac{6}{5}\Delta_o$	octahedron
	$3d^9$	Cu^{2+}			$(t_{2g})^6(e_g)^3$	$\frac{3}{5}\Delta_o + \frac{1}{2}\delta_3$	$\frac{3}{5}\Delta_o + \frac{1}{2}\delta_3$	deformed octahedron
	$3d^{10}$	Zn^{2+}	Ga^{3+}	Ge^{4+}	$(t_{2g})^6(e_g)^4$	-	-	octahedron*

hs and ls are high-spin and low-spin configurations, respectively; Δ_o Crystal field splitting parameter in octahedral coordination; δ_1 Splitting of t_{2g} orbital group; δ_3 Splitting of e_g orbital group.
* Zn^{2+} occurs in tetrahedral coordination in most oxide structures.

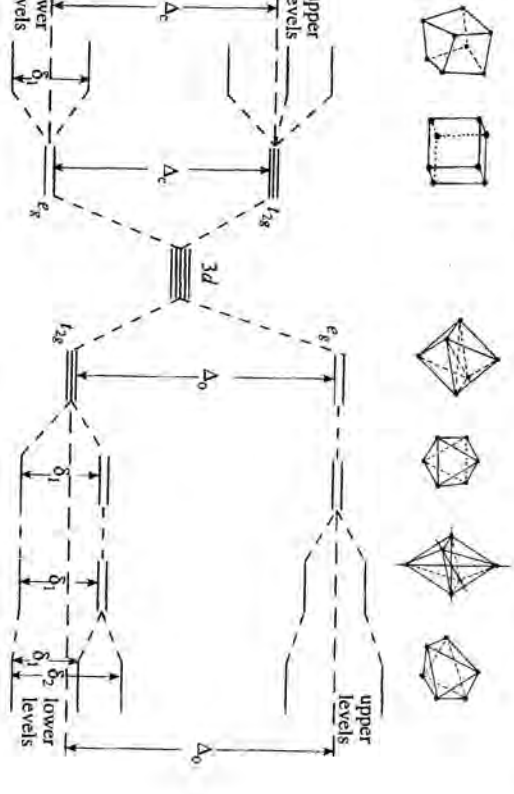

Figure 2.9 Relative energies of 3*d* orbital energy levels of a transition metal ion in low-symmetry distorted sites. (*a*) Regular octahedron (e.g., periclase); (*b*) trigonally distorted octahedron (e.g., corundum, spinel, approx. olivine M2 site); (*c*) tetragonally distorted octahedron (e.g., approx. olivine M1 site); (*d*) highly distorted six-coordinated (e.g., pyroxene M2 site); (*e*) regular cube; (*f*) distorted cube (e.g., triangular dodecahedral site of garnet).

distorted coordination polyhedra induce cation ordering in many mineral structures. If there is a variety of sites available to a cation during mineral crystallization, the cation will favour that site which accommodates it best and bestows greatest electronic stability. Site preferences of the transition metals are discussed in chapter 6 (§6.7). Second, unusual cation valences may be stabilized in distorted sites. Examples including Cr^{2+} in lunar olivines, Ti^{3+} in some pyroxenes found in carbonaceous chondrites and mare basalts from the Moon, and Mn^{3+} in the epidote and andalusite structures. These and other examples are described in §4.4.1, §4.4.2 and §6.2. Third, low-symmetry environments contribute to visual pleochroism in many non-cubic minerals when viewed in polarized light under the polarizing microscope. These effects on colours of minerals and gems are discussed in chapter 4 (§4.7). Finally, different splittings of the 3*d* orbitals, particularly for Fe^{2+} ions in highly distorted sites in pyroxenes and olivine, produce absorption bands at different energies in the near-infrared region and enable each mineral to be identified in remote-sensed spectra of planetary surfaces. Examples are considered in chapter 10.

2.14 Electronic entropy

We have noted that small changes of crystal field stabilization energy, an enthalpy term, are induced in many transition metal ions when they are situated in low-symmetry coordination sites. Another thermodynamic property similarly affected is the electronic entropy arising from differences of electronic configurations of a transition metal ion (Wood, 1981). Consider, for example, the Ti^{3+} ion. It contains one $3d$ electron which, in octahedral coordination, may be localized in any one of the three t_{2g} orbitals, each having the same energy. However, at a given instant, this single $3d$ electron has a one-third probability of being located in each of the d_{xy}, d_{yz} or d_{zx} orbitals. The entropy contribution resulting from this disorder is given by

$$S_{el} = -R \Sigma (P_i \ln P_i), \tag{2.27}$$

where P_i is the probability of the ith configuration occurring and R is the gas constant. When Ti^{3+} ions are located in a regular (undistorted) octahedral site, there are three configurations each with a one-third probability of occurrence, so that per gram ion

$$S_{el}(\text{oct}) = -3R \left(\frac{1}{3} \ln \frac{1}{3}\right) = 9.13 \text{ J (deg. g.ion)}^{-1}. \tag{2.28}$$

Similarly, if the Ti^{3+} ions were to occur in tetrahedral coordination, the single $3d$ electron could occupy either one of the two e orbitals, d_{z^2} or $d_{x^2-y^2}$, and the electronic entropy would be

$$S_{el}(\text{tet}) = -2R \left(\frac{1}{2} \ln \frac{1}{2}\right) = 5.76 \text{ J (deg. g.ion)}^{-1}. \tag{2.29}$$

For Cr^{3+} ions in octahedral coordination, there is just one unique electronic configuration in which its three $3d$ electrons occupy singly each of the t_{2g} orbitals. With probability of occurrence equal to one, the electronic entropy of Cr^{3+} is given by

$$S_{el}(\text{oct}) = -R (1 \ln 1) = 0. \tag{2.30}$$

The presence of a Ti^{3+} ion in a distorted octahedral site would also yield a zero electronic entropy term. This results from removal of the three-fold degeneracy of t_{2g} orbitals in the low-symmetry environment. Other effects of electronic entropy on thermodynamic properties of transition metal-bearing minerals are discussed in chapter 7 (§7.4).

2.15 Summary

Chapter 2 outlines the crystal field theory of chemical bonding, which is appropriate to ionic structures such as silicate and oxide minerals. In this electrostatic model, anions and dipolar groups (ligands) are regarded as point negative charges, and the effects of the surrounding ligands on the orbital energy levels of a transition metal cation are examined.

Orbitals. Atomic orbitals represent the angular distribution of electron density about a nucleus. The shapes and energies of these amplitude probability functions are obtained as solutions to the Schrödinger wave equation. Corresponding to a given principal quantum number, for example $n = 3$, there are one $3s$, three $3p$ and five $3d$ orbitals. The s orbitals are spherical, the p orbitals are dumb-bell shaped and the d orbitals crossed dumb-bell shaped. Each orbital can accomodate two electrons spinning in opposite directions, so that the d orbitals may contain up to ten electrons.

Transition elements. Elements of the first transition series are characterized by having incompletely filled $3d$ orbitals in one or more of their common oxidation states. The series includes scandium, titanium, vanadium, chromium, manganese, iron, cobalt, nickel and copper, which have electronic configurations of the form $(1s)^2(2s)^2(2p)^6(3s)^2(3p)^6(3d)^{10-n}(4s)^{1 \text{ or } 2}$.

Crystal field splitting, Δ. In the absence of magnetic and electric fields, the five $3d$ orbitals of an isolated transition metal ion have the same energy, that is they are five-fold degenerate, but have different spatial orientations. Lobes of the d_{z^2} and $d_{x^2-y^2}$ orbitals (the e_g group) project along the cartesian axes, whereas lobes of the d_{xy}, d_{yz} and d_{zx} orbitals (the t_{2g} group) are directed between these axes. When a transition metal ion is in octahedral coordination in a structure, the effect of the six ligands situated along the cartesian axes is to repel electrons in e_g orbitals to a greater extent than electrons in t_{2g} orbitals. The octahedral crystal field splitting parameter, Δ_o, is the induced energy separation between the t_{2g} and e_g orbital groups. The energy level of the t_{2g} group is lowered by $0.4\Delta_o$ and the e_g orbital group raised by $0.6\Delta_o$ relative to the hypothetical level of unresolved $3d$ orbitals.

Crystal field stabilization energy, CFSE. Each electron in a t_{2g} orbital stabilizes a transition metal ion in octahedral coordination by $0.4\Delta_o$, whereas every electron in an e_g orbital destabilizes it by $0.6\Delta_o$. The crystal field stabilization energy, CFSE, represents the algebraic sum of these factors. Cations may have

either high-spin configurations in which electrons with spins aligned occupy singly as many t_{2g} and e_g orbitals as possible, or low-spin configurations in which electrons fill t_{2g} orbitals. Favourable exchange interactions, reduced interelectronic repulsion and unnecessary pairing energies of two electrons in one orbital contribute to the stabilities of high-spin states. Low-spin states lead to a substantial increase in CFSE. Magnetic susceptibilities, interatomic distances and a variety of spectroscopic measurements may identify the spin state of each transition metal ion. Apart from Co^{3+} and Ni^{3+} ions, all transition metal cations exist in high-spin states in oxide structures on the Earth's surface. The ions Cr^{3+}, Ni^{2+} and Co^{3+} acquire high CFSE in octahedral coordination and Mn^{2+} and Fe^{3+} receive zero CFSE in high-spin states.

Evaluation of Δ. Energy separations between resolved 3*d* orbital energy levels correspond to visible and near-infrared radiation. Measurements of absorption spectra of transition metal compounds and minerals are used to obtain Δ and to evaluate the CFSE of the ions. Crystal field splittings may also be estimated from plots of thermodynamic data for the first-series transition metal compounds. The magnitude of Δ depends on:

(i) the symmetry of the coordinated ligands. Ratios of crystal field splittings in octahedral, body-centred cubic, dodecahedral and tetrahedral sites (where the cation is coordinated to 6, 8, 12 or 4 ligands, respectively) are: $\Delta_o : \Delta_c : \Delta_d : \Delta_t = 1 : -\frac{8}{9} : -\frac{1}{2} : -\frac{4}{9}$ where the negative signs indicate that d_{z^2} and $d_{x^2-y^2}$ orbitals become the more stable set relative to the other three *d* orbitals;

(ii) the valence of the cation, values for M^{3+} ions being higher than those for M^{2+} ions;

(iii) the nature and type of ligand coordinated to the cation. Thus, Δ_o for six CN^- anions is considerably larger than that for six H_2O ligands, with the result that cyanide complexes contain transition metal ions in low-spin states;

(iv) the interatomic distance, *R*, between metal and ligand. The $\Delta \propto R^{-5}$ relationship shows that small decreases in *R* lead to large increases of Δ;

(v) pressure, the effect of which is to shorten interatomic distances at elevated pressures, thereby increasing the CFSE of most transition metal cations; and

(vi) temperature, because thermal expansion may lower Δ.

The Jahn–Teller effect and stabilization energies in distorted coordination sites. Transition metal ions rarely occur in high-symmetry coordination sites in silicate minerals, which show various distortions from regular octahedral, tetrahedral, cubic and dodecahedral symmetries. The Jahn–Teller theorem states that cations with $3d^4$, $3d^9$ and low-spin $3d^7$ configurations, which have uneven distributions of electrons in e_g orbitals, should spontaneously distort their environments, thereby attaining increased electronic stability in low-symmetry sites. This explains why compounds of Cr^{2+}, Mn^{3+}, Cu^{2+} and Ni^{3+} are usually distorted from type-structures. In low-symmetry coordination sites the simple crystal field splitting parameter loses some of its significance because more than one energy separation between 3*d* orbital energy levels must be considered. Lowering of one or two orbital energy levels results in certain transition metal ions acquiring increased stabilization in distorted coordination sites. This leads to the possibility of relative enrichment of some cations in certain sites in silicate structures during mineral formation, stabilization of unusual oxidation states, pleochroism in non-cubic minerals, and specific profiles for Fe^{2+} silicates in remote-sensed spectra of planetary surfaces.

Electronic entropy. As a result of unequal electron occupancies of degenerate t_{2g} orbitals, the Ti^{3+} and Fe^{2+} ions in octahedral or tetrahedral sites, for example, may have large electronic entropies compared to zero values for Cr^{3+}. Electronic entropies decrease at elevated temperatures and are smaller when cations are located in distorted sites.

2.16 Background reading

Ballhausen, C. J. (1962) *Introduction to Ligand Field Theory.* (McGraw–Hill, New York), ch. 1.

Burns, R. G. (1985) Thermodynamic data from crystal field spectra. In *Macroscopic to Microscopic. Atomic Environments to Mineral Thermodynamics.* (S. W. Kieffer & A. Navrotsky, eds; Mineral. Soc.Amer. Publ.), *Rev. Mineral.*, 14, 277–316.

Burns, R. G. & Fyfe, W. S. (1967) Crystal field theory and the geochemistry of transition elements. In *Researches in Geochemistry, vol 2.* (P. H. Abelson, ed.; J. Wiley, New York), pp. 259–85

Cotton, F. A. & Wilkinson, G. (1988) *Advanced Inorganic Chemistry, 4th edn.* (Interscience Publ., New York), ch. 20.

Cotton, F. A., Wilkinson, G., & Gaus, P. L. (1988) *Basic Inorganic Chemistry, 2nd edn.* (J. Wiley & Sons, New York), chs 2 & 23.

Huheey, J. E. (1983) *Inorganic Chemistry: Principles of Structure and Reactivity, 3rd edn.* (Harper & Row, New York), ch. 9.

Orgel, L. E. (1966) *An Introduction to Transition Metal Chemistry: Ligand–Field Theory, 2nd edn.* (Methuen, London), chs 2 & 3.

Phillips, C. S. G. & Williams, R. J. P. (1966) *Inorganic Chemistry.* (Clarendon Press, Oxford), ch. 24.

3

Energy level diagrams and crystal field spectra of transition metal ions

A variety of selection rules derived from quantum mechanics governs the intensity of the various types of absorption phenomena.
– – The rules can be bent when ions get together.
G. R. Rossman, *Rev. Mineral.*, 18, 214 (1988)

3.1 Introduction

In the previous chapter it was shown how electrostatic fields produced by anions or negative ends of dipolar ligands belonging to coordination sites in a crystal structure split the 3*d* orbitals of a transition metal ion into two or more energy levels. The magnitude of these energy separations, or crystal field splittings, depend on the valence of the transition metal ion and the symmetry, type and distances of ligands surrounding the cation. The statement was made in §2.8 that separations between the 3*d* orbital energy levels may be evaluated from measurements of absorption spectra in the visible to near-infrared region. The origins of such crystal field spectra, also termed *d–d* spectra and optical spectra, are described in this chapter. Later chapters focus on measurements and applications of crystal field spectra of transition metal-bearing minerals.

3.2 Units in absorption spectra

When light is passed through a compound or mineral containing a transition metal ion, it is found that certain wavelengths are absorbed, often leading to coloured transmitted light. One cause of such absorption of light is the excitation of electrons between the split 3*d* orbital energy levels. Measurements of the intensity of light incident on and transmitted through the transition metal-bearing phase produces data for plotting an absorption spectrum. An absorption spectrum shows the amount of radiation absorbed or transmitted at each wavelength or energy. The absorption scale forms the ordinate and the abscissa is an energy or wavelength scale.

3.2.1 Wavelength and energy units

The position of an absorption band is measured on a wavelength scale which may be calibrated in ångstroms (Å), nanometre (nm) or micron (μm) units. Ångstrom units were most commonly used in early mineral spectroscopy literature, including the first edition of this book. However, in current spectral mineralogy research, absorption spectra are often plotted on nanometre scales, whereas micron units are commonly employed in reflectance spectra and remote-sensing applications (chapter 10). The relationship between these wavelength units is

$$1.0\ \mu m = 1{,}000\ nm = 10{,}000\ Å = 10^{-6}\ m\ . \qquad (3.1)$$

Some spectra are recorded on a wavenumber scale, which is inversely proportional to wavelength. The most common wavenumber unit is the reciprocal centimetre, which is related to wavelength units as follows:

$$1.0\ \mu m = 10^{-4}\ cm = 10^{4}\ cm^{-1} \text{ or } 10{,}000\ cm^{-1}. \qquad (3.2)$$

Thus, 1,000 nm corresponds to 10,000 cm^{-1}, 400 nm to 25,000 cm^{-1} and 2,000 nm to 5,000 cm^{-1}. Wavenumbers are sometimes equated with kaysers, ***K***, where

$$1\ \boldsymbol{K} = 1\ cm^{-1}, \text{ and } 10{,}000\ cm^{-1} = 10\ k\boldsymbol{K}\ . \qquad (3.3)$$

The advantage of the wavenumber scale is that it is linearly proportional to other energy units. Some of the relationships and conversion factors (see Appendix 8) are as follows:

$$1\ cm^{-1} = 11.966\ J = 2.859\ cal = 1.24 \times 10^{-4}\ eV. \qquad (3.4)$$

Convenient bench-marks in visible to near-infrared spectroscopy are summarized in table 3.1. Note that the Å, nm and cm^{-1} units are used interchangeably in this chapter and elsewhere throughout the book. Note, too, that the wavelength range 400 to 2,000 nm (or 4,000 to 20,000 Å, or 25,000 to 5,000 cm^{-1}) corresponds to energies of approximately 300 to 60 kJ. Energies of this magnitude are comparable to changes of enthalphies and free energies in many chemical reactions.

Table 3.1. *Wavelength and energy units used in crystal field spectra of minerals*

Wavelength units			Energy units			Colour
microns (μm)	nanometres (nm)	ångstroms (Å)	wave-numbers (cm^{-1})	electron volts (eV)	kilojoules (kJ)	
0.3	300	3,000	33,000	4.09	394.7	ultraviolet
0.4	400	4,000	25,000	3.10	299.0	violet
0.5	500	5,000	20,000	2.48	239.4	green
0.6	600	6,000	16,667	2.07	199.3	orange
0.7	700	7,000	14,286	1.77	170.9	red
0.8	800	8,000	12,500	1.55	149.5	near-infrared
1.0	1,000	10,000	10,000	1.24	119.6	↓
1.25	1,250	12,500	8,000	0.99	95.7	
1.5	1,500	15,000	6,667	0.83	79.7	
1.75	1,750	17,500	5,714	0.71	68.3	
2.0	2,000	20,000	5,000	0.62	59.8	mid-infrared
2.5	2,500	25,000	4,000	0.50	47.8	↓

3.2.2 Absorption terminology

A variety of constants have been used to express absorption. All of these constants are based on the following general equation

$$\log \frac{I_0}{I} = a\,b, \tag{3.5}$$

where: I_0 is the intensity of the incident light,
I is the intensity of the emergent light,
a is the absorption constant
b is a constant depending on the conditions of the measurement.

The ratio I_0/I is obtained directly from a spectrophotometric measurement, and the value of a is then calculated from eq. (3.5) to yield the desired absorption constant. The numerous absorption constants found in the literature arise from the choice of quantities incorporated in the constant b. Some of the terms most commonly used to express absorption in minerals are summarized in table 3.2. Note that optical densities (*O.D.*), representing the direct output from many spectrophotometers, lack specificity about sample thickness and element concentrations. Absorption coefficients (α) indicate that sample thicknesses have been measured or estimated. Molar extinction coefficients (ε) require chemical analytical data as well as knowledge of sample thicknesses.

Table 3.2. *Absorption units used in crystal field spectra of minerals*

Intensity term	Symbol	Equation*	Units
Transmission	T	$T = (I/I_0)$	–
Absorption	A	$A = 1 - T = 1 - (I/I_0)$	–
Optical density or Absorbance	*O.D.*	*O.D.* $= \log(I/I_0)$	–
Absorption coefficient or Extinction coefficient	α	$\alpha = \log(I/I_0)/d$	cm^{-1}
Molar extinction coefficient	ε	$\varepsilon = \log(I/I_0)/C\,d$	litre $mole^{-1}$ cm^{-1} or litre $(g.ion)^{-1}$ cm^{-1}
Oscillator strength	f	$f \approx$ (const) $\varepsilon_{max}\,\Delta\upsilon_{1/2}$	–

* I_0 and I are the intensities of incident and emergent light, respectively; d is the thickness, in cm, of the material or optical path length in the medium; C is the concentration of the absorbing species in moles per litre or gm ions per litre; $\Delta\upsilon_{1/2}$ is the width of an absorption band (expressed as wavenumber units) at half peak-height at which the molar extinction coefficient, ε, is a maximum.

The assumption is made that absorption bands have Gaussian shapes, that is, they fit an expression of the form

$$\varepsilon = \varepsilon_0 \exp[-C(\upsilon - \upsilon_0)^2], \tag{3.6}$$

where C is a constant, υ_0 is the wavenumber at the centre of the band, and ε_0 is the molar extinction coefficient there. The area under the absorption band is approximately equal to $\varepsilon_0\Delta\upsilon_{1/2}$, where $\Delta\upsilon_{1/2}$ is the full width of the band at half peak-height in wavenumber units. This area also appears in approximations of the oscillator strength, f, which is related to the probability of an electronic transition, discussed later (§3.7.1).

A fundamental relationship used in electronic absorption spectroscopy is the Beer–Lambert law which states that the amount of light absorbed is proportional to the number of absorbing molecules or ions through which the light passes. The Beer–Lambert law is formulated as

$$\log \frac{I_0}{I} = \varepsilon\,C\,d, \tag{3.7}$$

where ε is the molar extinction coefficient in units such as litre $mole^{-1}$ cm^{-1}
C is concentration expressed in moles/litre or gram ions/litre
d is the path length measured in centimetres.

The concentration, C, of a transition metal ion in solid-solution in a silicate mineral may be calculated from the mole fraction, X, and the molar volume, V, of the silicate phase by the equation

$$C = \frac{X}{V}. \tag{3.8}$$

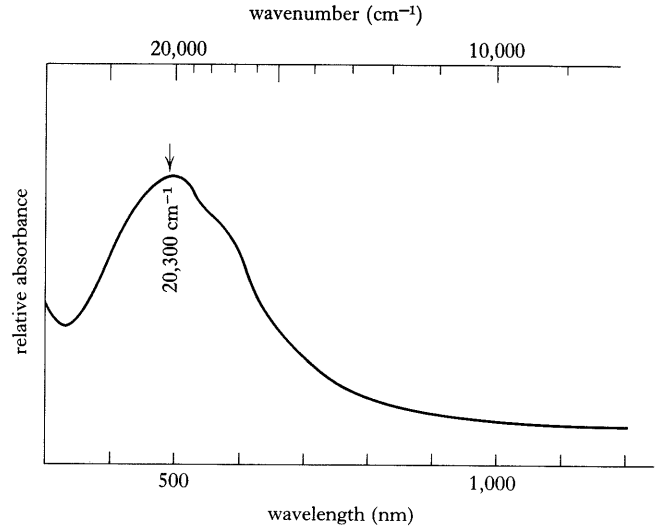

Figure 3.1 Absorption spectrum of the hexahydrated Ti^{3+} ion in an aqueous solution of caesium titanium(III) sulphate.

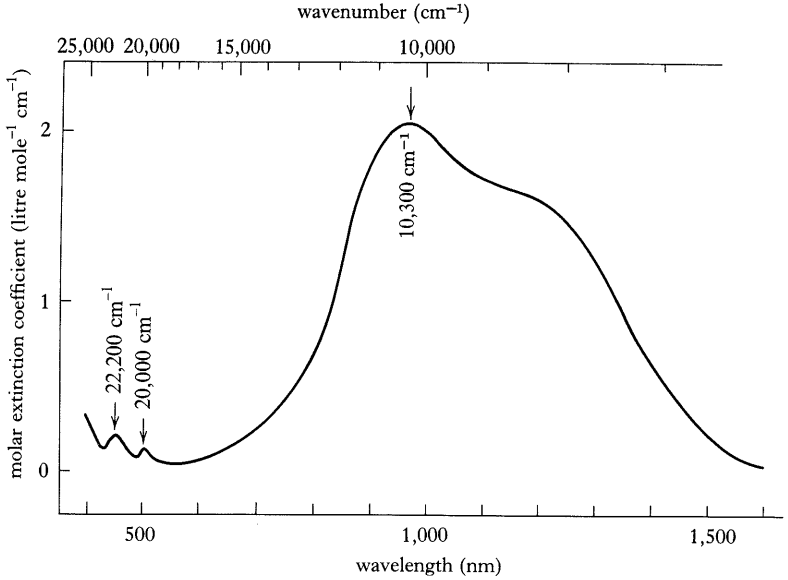

Figure 3.2 Absorption spectrum of the hexahydrated Fe^{2+} ion in an aqueous solution of iron(II) ammonium sulphate

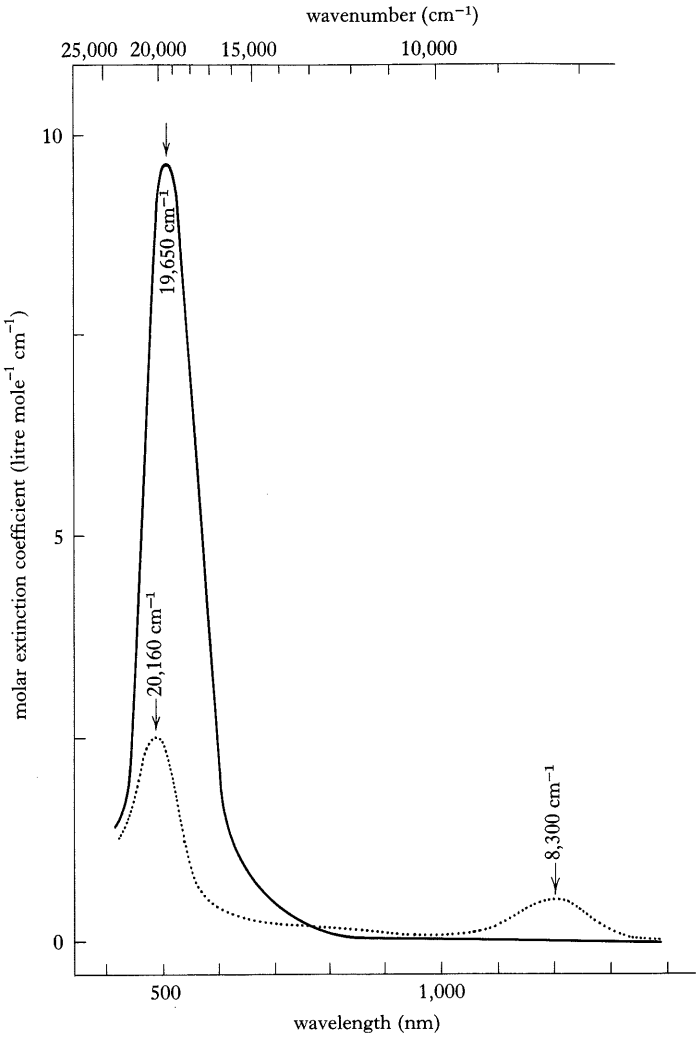

Figure 3.3 Polarized absorption spectra of the tetragonal mineral gillespite, $BaFe^{2+}Si_4O_{10}$, measured with light polarized parallel and perpendicular to the *c* crystallographic axis (see §3.8.1). ——**E**∥*c* spectrum; ·····**E**⊥*c* spectrum.

Methods for calculating molar extinction coefficients of minerals are outlined in chapter 4 (§4.3). The importance of the Beer–Lambert law, eq. (3.7), is that the molar extinction coefficient of an absorption band should be independent of the concentration of the absorbing species. Deviations from this law originating from cation ordering are discussed in chapter 4.

3.3 Examples of crystal field spectra

The absorption spectrum profile for the hexahydrated Ti^{3+} ion, $[Ti(H_2O)_6]^{3+}$, is shown in fig. 3.1. For this $3d^1$ cation, the spectrum consists of a broad band centred at a wavelength of about 493 nm (20,280 cm^{-1}). Absorption spectra of ions with more than one $3d$ electron are more complex. This is illustrated in fig. 3.2 by the spectrum of the hexahydrated Fe^{2+} ion with six $3d$ electrons. In addition to the dominant broad band centred around 1,000 nm, several sharp peaks occur between 400 and 500 nm for the $[Fe(H_2O)_6]^{2+}$ ion. Further complexities arise in the spectra of transition metal ions in anisotropic crystals in polarized light. For example, the spectra of the tetragonal mineral gillespite, $BaFe^{2+}Si_4O_{10}$, shown in fig. 3.3 differ when the electric vector, **E**, of polarized light is transmitted along the two different crystallographic directions of this uniaxial mineral (§3.8.1). Even larger variations exist in polarized spectra of transition metal ions in biaxial minerals, such as Fe^{2+} in orthorhombic olivine (fig. 5.8) and Mn^{3+} in monoclinic epidote crystals (fig. 4.3) described in later chapters.

Absorption bands in each of the crystal field spectra illustrated in figs 3.1, 3.2 and 3.3 have three characteristic features: energy, as measured by the position of the band expressed in wavelength (e.g., nanometres or ångstroms) or wavenumber (cm^{-1}) units; intensity of absorption, as measured by the height or area of the band; and sharpness or width of the band at half maximum peak-height. The origins of these spectral features may be correlated with energy levels corresponding to differerent electronic configurations of each transition metal ion in various coordination sites.

3.4 Energy level diagrams for octahedral environments

3.4.1 Spectroscopic terms and crystal field states

The effect of an octahedral crystal field on the $3d$ orbitals of a transition metal ion is to split the original group of five $3d$ orbitals into two levels, a lower-level group of three t_{2g} orbitals and an upper-level group of two e_g orbitals separated by an energy Δ_o (see fig. 2.4). Illustrated in fig. 3.4 are the energy levels of the Ti^{3+} ion before and after its single $3d$ electron is excited from a t_{2g} orbital to an e_g orbital when the cation is in octahedral coordination with six ligands. The energy level diagram shows that the energy separation between the two electronic states increases with increasing strength of the crystal field. The two crystal field states are derived from one energy level for the gaseous or field-free Ti^{3+} ion, designated as the ^2D spectroscopic term. The lowest energy state, or ground state, of the Ti^{3+} ion in an octahedral crystal field can have only one

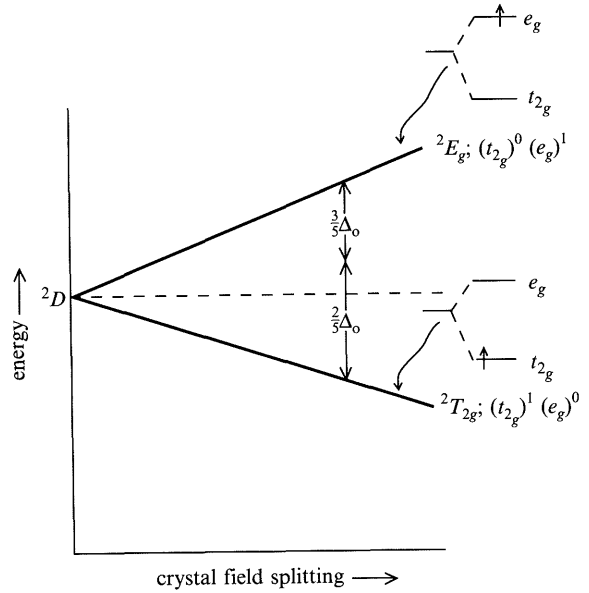

Figure 3.4 Energy level diagram for the Ti^{3+} ($3d^1$) ion in an octahedral crystal field.

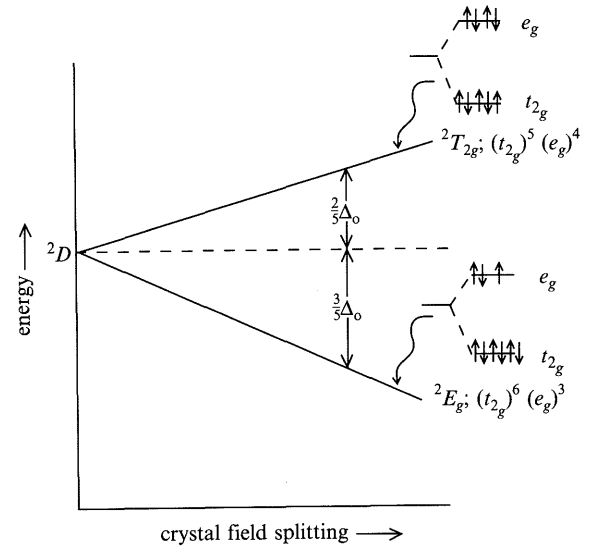

Figure 3.5 Energy level diagram for the Cu^{2+} ($3d^9$) ion in an octahedral crystal field.

configuration, $(t_{2g})^1(e_g)^0$. The spectrum in fig. 3.1 represents the excitation of the single $3d$ electron from the t_{2g} to the e_g level to give the excited state with configuration $(t_{2g})^0(e_g)^1$. The spectrum indicates that the average value of Δ_o for the hydrated Ti^{3+} ion is about 20,300 cm^{-1}. Cations with nine $3d$ electrons, such as Cu^{2+}, also can have only one configuration in the ground state, $(t_{2g})^6(e_g)^3$. Absorption of radiation at 12,600 cm^{-1} by aqueous solutions containing the $[Cu(H_2O)_6]^{2+}$ complex ion excites an electron from a t_{2g} orbital to the hole or vacancy in the e_g level to give the excited state with configuration $(t_{2g})^5(e_g)^4$. Alternatively, the transition may be regarded as transfer of a hole in the unfilled e_g orbital to a t_{2g} orbital. As a result, the energy level diagram for a $3d^9$ cation is similar to that for a $3d^1$ cation but the levels are inverted. This is illustrated in fig. 3.5.

Energy level diagrams for cations with more than one or less than nine $3d$ electrons are more complex. For such ions there are more than two ways of arranging the $3d$ electrons in the orbitals of the field-free cation, leading to several electronic configurations with different interelectronic repulsion energies for the excited states. The different electronic configurations for the isolated or field-free ions are called spectroscopic, L–S, or Russell–Saunders terms and are designated by symbols such as ^2D, ^3F, ^6S, etc. The capital letters denote the total atomic orbital angular momenta ($L = \Sigma m_l$) summed over all of the $3d$ electrons, the nomenclature being similar to those for individual *s, p, d* and *f* electrons given in §2.2.2. The superscript numerals denote the spin multiplicities, r, where $r = (2\Sigma m_s + 1)$ and $m_s = \frac{1}{2}$ for each unpaired electron. Thus, the spin-multiplicity is simply obtained by adding one to the total number of unpaired electrons in an electronic configuration. States with zero, one, two, etc., unpaired electrons are designated as singlet, doublet, triplet, etc., states, respectively. The nomenclatures of spectroscopic terms are defined in Appendix 4 and are summarized in table 3.3 for each d^n configuration. A $3d^1$ ion such as Ti^{3+} has only one spectroscopic term, ^2D, whereas the Fe^{2+} ion with six $3d$ electrons has sixteen such terms, including the quintet ground term ^5D and several excited triplet and singlet terms. Each spectroscopic term has a different energy level, since electrons populating different orbitals interact with one another and with the nucleus in different ways. The energy separations between the various spectroscopic terms are expressed by the Racah B and C parameters* which in the field-free (gaseous) cation are a measure of interelectronic repulsion resulting from coulombic and exchange interactions. Energy separations between spectroscopic terms of the same spin multiplicity usually contain the Racah B parameter, whereas both B and C parameters appear in

* Occasionally, the Condon-Shortley parameters F_2 and F_4, are used instead, and are related to the Racah parameters by $B = F_2 - 5F_4$ and $C = 35F_4$

Table 3.3. *Spectroscopic terms arising from each $3d^n$ configuration for transition metal ions*

Electronic configuration	Cations							Spectroscopic terms*
	M^{1+}	M^{2+}	M^{3+}	M^{4+}	M^{5+}	M^{6+}	M^{7+}	
[Ar]	K^+	Ca^{2+}						**^1S**
[Ar]$3d^0$ [Ar]$3d^{10}$	Cu^+	Zn^{2+}	Sc^{3+} Ga^{3+}	Ti^{4+} Ge^{4+}	V^{5+}	Cr^{6+}	Mn^{7+}	**^1S**
[Ar]$3d^1$ [Ar]$3d^9$		Cu^{2+}	Ti^{3+}	V^{4+}				**^2D**
[Ar]$3d^2$ [Ar]$3d^8$		Ni^{2+}	V^{3+}					**^3F**, ^3P, ^1G, ^1D, ^1S
[Ar]$3d^3$ [Ar]$3d^7$		Co^{2+}	Cr^{3+} Ni^{3+}	Mn^{4+}				**^4F**, ^4P, ^2H, ^2G, ^2F, ^2D, ^2D
[Ar]$3d^4$ [Ar]$3d^6$		Cr^{2+} Fe^{2+}	Mn^{3+} Co^{3+}					**^5D**, ^3H, ^3G, ^3F, ^3F, ^3D, ^3P, ^3P, ^1I, ^1G, ^1G, ^1F, ^1D, ^1D, ^1S, ^1S
[Ar]$3d^5$		Mn^{2+}	Fe^{3+}					**^6S**, ^4G, ^4F, ^4D, ^4P, ^2I, ^2H, ^2G, ^2G, ^2F, ^2F, ^2D, ^2D, ^2D, ^2P, ^2S

* The ground term for each electronic configuration is listed first.

expressions for energy differences between terms having different spin multiplicities (Lever, 1984, p. 126). Although these parameters could be obtained by accurate calculations of the coulomb and exchange integrals (Ballhausen, 1962; Lever, 1984), they are determined empirically from measurements of atomic spectra. The use of Racah parameters as a measure of covalent bonding is discussed in chapter 11 (§11.2).

The energy level diagram for Ti^{3+} in fig. 3.4 shows the manner by which the ^2D spectroscopic term is resolved into two different levels, or crystal field states, when the cation is situated in an octahedral crystal field produced by surrounding ligands. In a similar manner the spectroscopic terms for each $3d^n$ configuration become separated into one or more crystal field states when the transition metal ion is located in a coordination site in a crystal structure. The extent to which each spectroscopic term is split into crystal field states can be obtained by semi-empirical calculations based on the interelectronic repulsion Racah B and C parameters derived from atomic spectra (Lever, 1984, p. 126).

Table 3.4. *Crystal field states arising from free ion spectroscopic terms of transition metals in octahedral coordination*

Free-ion spectroscopic terms	Crystal field states
S	A_{1g}
P	T_{1g}
D	$T_{2g} + E_g$
F	$A_{2g} + T_{1g} + T_{2g}$
G	$A_{1g} + E_g + T_{1g} + T_{2g}$
H	$E_g + T_{1g} + T_{1g} + T_{2g}$
I	$A_{1g} + A_{2g} + E_g + T_{1g} + T_{2g} + T_{2g}$

Bethe, in 1929, used symmetry arguments to determine the qualitative nature of the orbital splittings for transition metal ions in various coordination symmetries. Bethe (1929) demonstrated how it is possible, using the methods of group theory, to determine just what crystal field states will result when an ion of any given electronic configuration is introduced into a crystal field with a definite symmetry. Bethe's calculations showed that for octahedral environments there are collectively only five types of crystal field states that can arise from the various spectroscopic terms of field-free transition metal ions when they are placed in an octahedral crystal field. These crystal field states are summarized in table 3.4 (see also Appendix 5). Each crystal field state is given a group theory symbol notating the symmetry properties of its electronic configuration, by analogy with the wave functions of electrons in individual s (a_{1g}), p (t_{1u}) and d (t_{2g} and e_g) orbitals described earlier (§2.3). Thus, the ^2D spectroscopic term of Ti^{3+} is resolved into the $^2T_{2g}$ and ^2E_g crystal field states when the cation is present in an octahedral site in a crystal structure. This symbolism for crystal field states is analogous to that used for $3d$ orbitals which are separated into t_{2g} and e_g groups when the cation occurs in octahedral coordination. The symbol $^2T_{2g}$ represents the symmetry of the ground-state configuration $(t_{2g})^1(e_g)^0$ and highlights the symmetry of the three-fold degeneracy (symbol T_2) of the single $3d$ electron in three equivalent t_{2g} orbitals in the centrosymmetric (subscript g) octahedral site. The spin-multiplicity of Ti^{3+} is denoted by the superscript 2 (doublet) in the $^2T_{2g}$ representation. When the single $3d$ electron of Ti^{3+} is induced to occupy one of the e_g orbitals by absorption of light in the visible region (*e.g.*, at the wavelength 493 nm in fig. 3.1), the excited state is represented by ^2E_g to designate the symmetry of the two-fold degeneracy (symbol E) of the $(t_{2g})^0(e_g)^1$ electronic configuration. The $^2T_{2g} \rightarrow {}^2E_g$

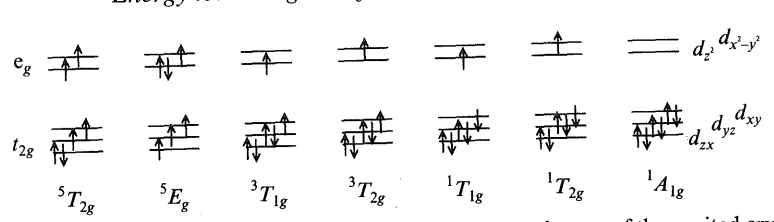

Figure 3.6. Electronic configurations of the ground state and some of the excited crystal field states of the Fe^{2+} ($3d^6$) ion in octahedral coordination.

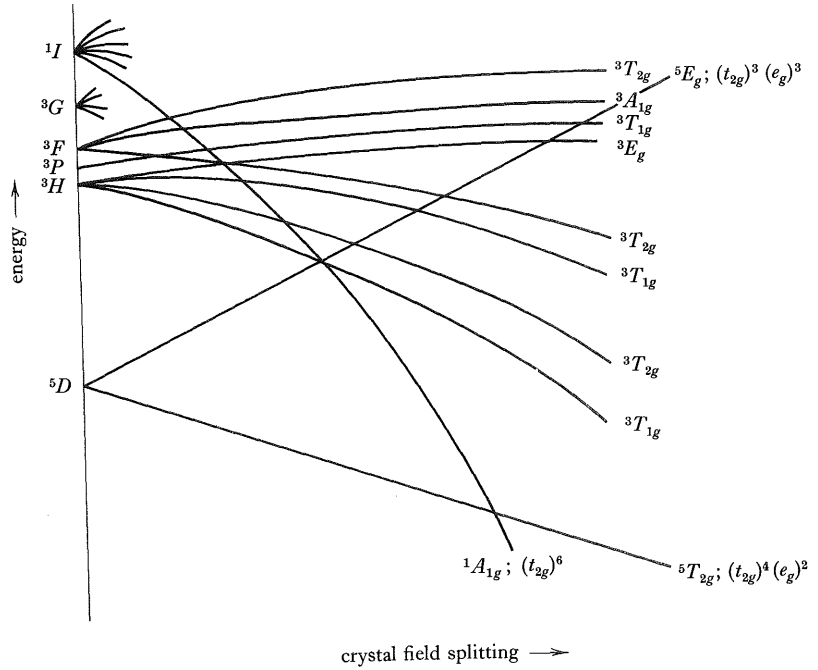

Figure 3.7 Simplified energy level diagram for $3d^6$ ions (e.g., Fe^{2+} and Co^{3+}) in an octahedral crystal field. The diagram shows that in a high intensity field the $^1A_{1g}$ crystal field state, corresponding to the low-spin configuration $(t_{2g})^6$, becomes the ground state.

transition thus depicts the change of electronic configuration of Ti^{3+} from $(t_{2g})^1$ to $(e_g)^1$ in which there is no change in the number of unpaired electrons.

The Fe^{2+} ion, $3d^6$, in octahedral coordination in a silicate has the ground state configuration $(t_{2g})^4(e_g)^2$ or alternatively $(t_{2g}\uparrow)^3(t_{2g}\downarrow)^1(e_g\uparrow)^2$ depicted in fig. 3.6. This configuration is represented by $^5T_{2g}$, in which five of the $3d$ electrons spinning, say, clockwise (or spin-up) occupy singly each of the $3d$ orbitals and the sixth electron with anticlockwise spin (or spin-down) pairs up in one of the three-fold degenerate (symmetry T_2) t_{2g} orbitals in the centrosymmetric (g)

octahedron. In this high-spin configuration, Fe^{2+} has four unpaired electrons (i.e., it is a quintet state). The sixth spin-down $t_{2g}\downarrow$ electron when excited to one of the half-filled two-fold degenerate (E) e_g orbitals gives rise to the ^5E_g crystal field state, representing the configuration $(t_{2g})^3(e_g)^3$ or $(t_{2g}\uparrow)^3(e_g\uparrow)^2(e_g\downarrow)^1$, still with a resultant of four unpaired electrons (fig. 3.6). Thus, the $^5T_{2g} \rightarrow {}^5E_g$ transition in a Fe^{2+} ion located in an octahedral site results in no change in the number of unpaired electrons. The relative energies of the two quintet crystal field states of Fe^{2+} derived from the ^5D spectroscopic term with increasing intensity of the crystal field are indicated by the energy level diagram shown in fig. 3.7. This qualitative energy level diagram for Fe^{2+} resembles that of Ti^{3+} shown in fig. 3.4. However, there are additional triplet and singlet crystal field states for Fe^{2+} derived from some of the low spin-multiplicity spectroscopic terms, all corresponding to electronic configurations with fewer unpaired electrons, some of which are shown in fig. 3.6. In strong crystal fields one of these states, $^1A_{1g}$, representing the unique, spherically symmetric, low-spin electronic configuration $(t_{2g})^6(e_g)^0$ with zero unpaired electrons, becomes the ground state. The cross-over from high-spin to low-spin, which is calculated to take place in the field-free cation when Δ_o exceeds 19,150 cm^{-1} (table 2.5), profoundly affects the ionic radius and magnetic properties of divalent iron. The geophysical consequences of such spin-pairing transitions are discussed in chapter 9 (§9.7).

3.4.2 Tanabe–Sugano Diagrams

The relative energies of the crystal field states of octahedrally coordinated Fe^{2+} ions may also be represented on a Tanabe–Sugano diagram such as that illustrated in fig. 3.8. The energy levels plotted in fig. 3.8 are based on the interelectronic repulsion Racah parameters B and C determined empirically from the atomic spectrum of gaseous Fe^{2+} and the crystal field spectrum of Fe^{2+} ions in the periclase structure. Only nine of the free ion spectroscopic terms of Fe^{2+} listed in table 3.3 are shown in fig. 3.8, the remainder occurring at much higher energies. Note that the lowest energy (ground state) crystal field state is drawn horizontally in a Tanabe–Sugano energy level diagram. This is $^5T_{2g}$ when Fe^{2+} has the high-spin configuration (fig. 3.6). A break in slope of all Fe^{2+} crystal field states occurs beyond the vertical dashed line in fig. 3.8 when the $^1A_{1g}$ level, corresponding to the low-spin configuration (fig. 3.6), becomes the ground state. This occurs when the strength of the crystal field in a coordination site becomes sufficiently high to induce spin-pairing in Fe^{2+} ions (§2.5 and §9.7). Transitions shown by the vertical dotted line in fig. 3.8 correspond to features in the spectrum of the hexahydrated Fe^{2+} ion illustrated in fig. 3.2, including the $^5T_{2g} \rightarrow {}^5E_g$ transition responsible for the broad absorption band near 10,000 cm^{-1}.

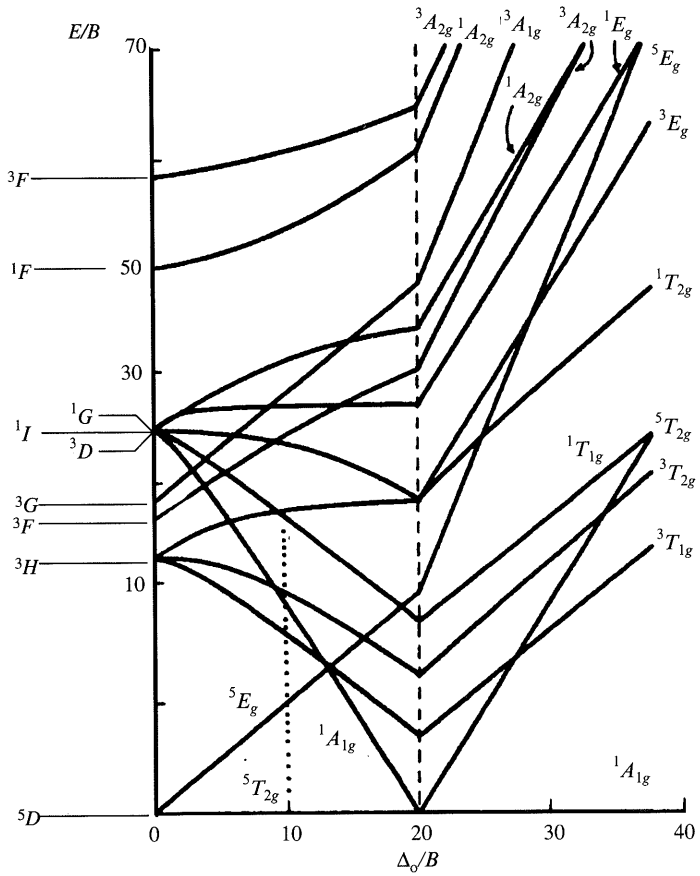

Figure 3.8 Tanabe–Sugano energy level diagram for a $3d^6$ ion in an octahedral crystal field. Note that some of the highest energy triplet and singlet crystal field states listed in table 3.3 are not shown in the diagram.

This transition results in no change in the number of unpaired electrons in Fe^{2+} and is referred to as a spin-allowed transition. The sharp peaks at 20,000 cm^{-1} and 22,200 cm^{-1} in fig. 3.2 correspond to transitions to the triplet states $^3T_{1g}$ and $^3T_{2g}$, respectively (cf. fig. 3.6), having lower spin-multiplicities than the quintet $^5T_{2g}$ ground state. Such transitions leading to fewer unpaired electrons in excited crystal field states are termed spin-forbidden transitions.

Comparable energy level diagrams to that shown for Fe^{2+} in fig. 3.8 may be constructed for each transition metal cation from spectroscopic terms of the field-free ion. The Tanabe–Sugano diagrams for other octahedrally coordinated transition metal ions are discussed later in chapter 5 (§5.10)

Cations with $3d^5$ configurations have distinctive energy level diagrams and crystal field spectra which are worthy of special attention. The electronic con-

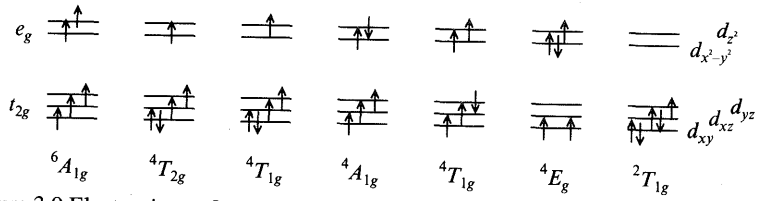

Figure 3.9 Electronic configurations of the ground state and some of the excited crystal field states of the $3d^5$ cations, Fe^{3+} and Mn^{2+}, in octahedral coordination.

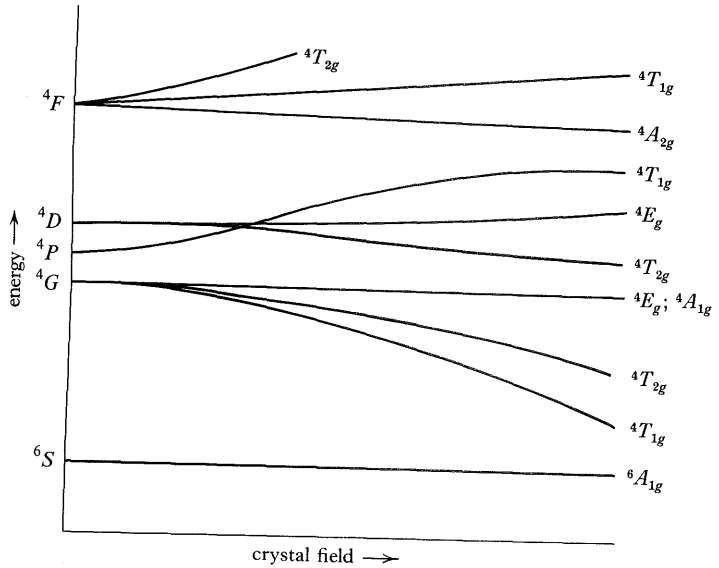

Figure 3.10 Partial energy level diagram for the Fe^{3+} or Mn^{2+} ions with $3d^5$ configurations in high-spin states in an octahedral crystal field. Only sextet and quartet spectroscopic terms and crystal field states are shown. Note that the same energy level diagram applies to the cations in tetrahedral crystal fields (with g subscripts omitted from the state symbols for the acentric coordination site).

figurations of Fe^{3+} and Mn^{2+} illustrated in fig. 3.9 are such that in the ground state the five $3d$ electrons occupy singly each of the three t_{2g} and the two e_g orbitals. In this half-filled high-spin state, $(t_{2g}\uparrow)^3(e_g\uparrow)^2$, represented by $^6A_{1g}$ (where A_{1g} again represents an unique spherically symmetric electronic configuration), there are five unpaired electrons (i.e. a sextet state) with spins aligned parallel (spin-up) when Fe^{3+} ions occupy centrosymmetric octahedral sites. In the energy level diagram shown in fig. 3.10, the $^6A_{1g}$ level represents the ground state of Fe^{3+} in an octahedral crystal field. All excited states of Fe^{3+}, some of which are depicted in fig. 3.9, correspond to electronic configurations with fewer unpaired electrons and, hence, lower spin-multiplicities (i.e. they are either quartets or doublets) than the sextet ground state. As a result, all electronic transitions between the $3d$ orbitals of the Fe^{3+} and Mn^{2+} ions are spin-forbidden, leading to weak spectral features in their absorption spectra. Energy levels of the $^4T_{1g}$ and $^4T_{2g}$ crystal field states shown in fig. 3.10 correspond to electronic configurations derived from $(t_{2g})^4(e_g)^1$ or $(t_{2g}\uparrow)^3(t_{2g}\downarrow)^1(e_g\uparrow)^1$. The difference between these two excited crystal field states is related to different interaction energies between the solitary electron remaining in one of the e_g orbitals and the paired electron in one of the t_{2g} orbitals. Thus, less repulsion occurs when these electrons occupy, say, the d_{z^2} and d_{xy} orbitals ($^4T_{1g}$), compared to the d_{xy} and $d_{x^2-y^2}$ orbitals ($^4T_{2g}$). Other distributions such as ($d_{x^2-y^2}$ + d_{yz},) or ($d_{x^2-y^2}$ + d_{xz},) and (d_{xz} +d_{z^2}) or (d_{yz} + d_{z^2}) account for the three-fold degeneracies represented by the $^4T_{1g}$ and $^4T_{2g}$ states, respectively.

3.4.3 Orgel diagrams

Certain qualitative similarities exist between the energy level diagrams for the various $3d^n$ configurations when only crystal field states with the highest spin-multiplicity are considered. There are essentially only three distinct types of energy level diagrams for transition metal ions, corresponding to crystal field states derived from the field-free *S, D,* and *F* spectroscopic ground terms, respectively. Such features, first recognised by Orgel (1952), are summarized in the Orgel diagrams shown in figs 3.11 and 3.12. As might be inferred from fig. 3.4 (Ti^{3+}) and fig. 3.6 (Fe^{2+}), octahedral cations with $3d^1$ and $3d^6$ configurations have the same type of diagram, which in inverted form correspond to the energy level diagram for $3d^4$ (Mn^{3+}) and $3d^9$ (Cu^{2+}) ions (cf. fig. 3.5). These cations, each possessing a *D* spectroscopic ground term, are all represented by the Orgel diagram shown in fig. 3.11. Similarly, octahedrally coordinated cations with $3d^2$ (V^{3+}) and $3d^7$ (Co^{2+}) configurations have similar Orgel diagrams, which correspond to the inverted diagrams for $3d^3$ (Cr^{3+}) and $3d^8$ ions (Ni^{2+}). The Orgel diagram linking all cations with *F* spectroscopic ground terms is shown in fig. 3.12. Curvature of crystal field states with T_{1g} symmetry derived from the spectroscopic *F* and *P* terms is a consequence of the non-crossing rule of group theory. Thus, states with the same symmetry may interact with one another, whereby the lower energy state becomes stabilized and the higher energy one destabilized the closer they approach each other. This non-crossing behaviour of the $T_{1g}(F)$ and $T_{1g}(P)$ states is a manifestation of molecular orbital bonding interactions and influences the Racah *B* parameter, which is used as a measure of covalent bond character in transition metal compounds described in chapter 11 (§11.2). The third type of Orgel diagram, that

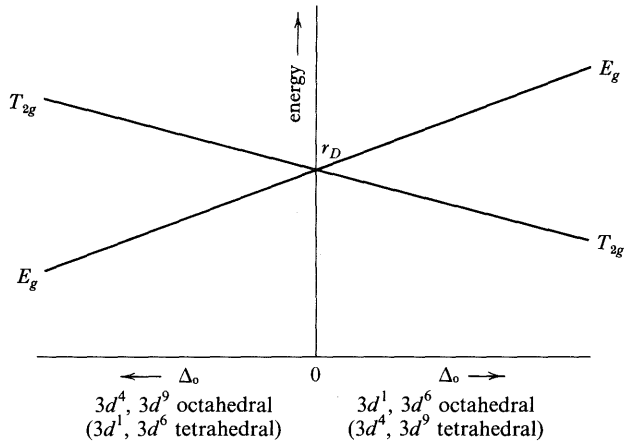

Figure 3.11 Orgel diagram for transition metal ions possessing ^rD spectroscopic terms in octahedral crystal fields of increasing intensity. The right-hand side applies to $3d^1$ (e.g., Ti^{3+}) and $3d^6$ (e.g., Fe^{2+}) cations and the left-hand side to $3d^4$ (e.g., Mn^{3+}) and $3d^9$ (e.g., Cu^{2+}) cations in octahedral coordination. The diagram in reverse also applies to the cations in tetrahedral, cubic and dodecahedral coordinations.

for $3d^5$ cations (Fe^{3+} and Mn^{2+}), corresponds to the Tanabe–Sugano diagram already illustrated in fig. 3.10.

It must be stressed that although qualitative features exist in Orgel diagrams for the three groups of transition metal ions, they are not identical for any pair of cations since the energy separations between the crystal field states of individual ions are different. For example, although qualitative similarities exist in the energy level diagrams for octahedral $3d^1$ and $3d^6$ ions, the energy separations for Ti^{3+} are larger than those for Fe^{2+}, which influence the positions of absorption bands in their respective crystal field spectra (compare figs 3.1 and 3.2.). A similar situation exists for the octahedral $3d^3$ and $3d^8$ cations (Cr^{3+} and Ni^{2+}) and the $3d^2$ and $3d^7$ cations (V^{3+} and Co^{2+}).

The Orgel diagrams illustrated in figs 3.11 and 3.12 indicate that, for electronic transitions between crystal field states of highest spin-multiplicities, one absorption band only is expected in the spectra of $3d^1$, $3d^4$, $3d^6$ and $3d^9$ cations in octahedral coordination, whereas three bands should occur in the spectra of octahedrally coordinated $3d^2$, $3d^3$, $3d^7$ and $3d^8$ ions. Thus, if a crystal structure is known to contain cations in regular octahedral sites, the number and positions of absorption bands in a spectrum might be used to identify the presence and valence of a transition metal ion in these sites. However, this method of cation identification must be used with caution. Multiple and displaced absorption bands may occur in the spectra of transition metal ions situated in low-symmetry distorted coordination sites.

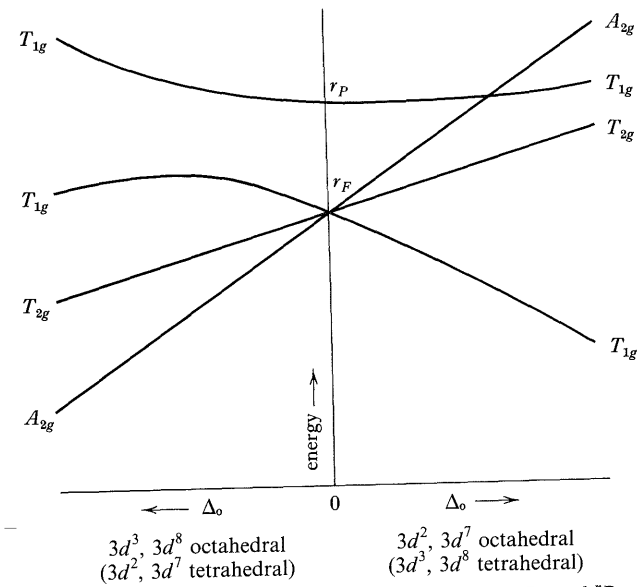

Figure 3.12 Orgel diagram for transition metal ions possessing ^rF and ^rP spectroscopic terms in octahedral crystal fields of increasing intensity. The right-hand side applies to $3d^2$ (e.g., V^{3+}) and $3d^7$ (e.g., Co^{2+}) cations and the left-hand side to $3d^3$ (e.g., Cr^{3+}) and $3d^8$ (e.g., Ni^{2+}) cations in octahedral coordination. The diagram in reverse also applies to the cations in tetrahedral, cubic and dodecahedral coordinations.

3.5 Energy level diagrams for other high-symmetry environments

Energy level diagrams for cations in tetrahedral and body-centred cubic coordinations are related to those for octahedrally coordinated ions. Since the crystal field splittings of $3d$ orbitals in tetrahedral and eight-fold cubic coordinations are opposite to that for octahedral coordination (§2.6), energy levels for cations in tetrahedral, cubic and dodecahedral environments correspond to inverted diagrams for the corresponding ions in octahedral coordination, except for cations with $3d^5$ configurations. These correlations lead to the following general relationships between energy level diagrams:

$$3d^n_{\text{octahedral}} \text{ is the same as } 3d^{10-n}_{\text{tetrahedral}}, 3d^{10-n}_{\text{cubic}} \text{ and } 3d^{10-n}_{\text{dodecahedral}} \tag{3.9}$$

and

$$3d^n_{\text{tetrahedral}},\ 3d^n_{\text{cubic}}, 3d^n_{\text{dodecahedral}} \text{ are the same as } 3d^{10-n}_{\text{octahedral}}. \tag{3.10}$$

For $3d^5$ ions, the same diagram applies for octahedral, tetrahedral, cubic and dodecahedral coordination environments.

The relationships in eqs (3.9) and (3.10) are included in the Orgel diagrams shown in figs. 3.11 and 3.12. Note again, however, that the predicted similarities between the energy level diagrams of an octahedrally coordinated d^n ion and the corresponding tetrahedral d^{10-n} ion of the same valence are only qualitative. In particular, since $\Delta_t = -\frac{4}{9}\Delta_o$ (eq. (2.7)), distinctly different energy separations and peak positions in crystal field spectra are to be expected for cations in octahedral and tetrahedral sites.

Another important feature concerns the energy level diagram for cations with $3d^5$ configurations (fig. 3.10), the profile of which is apparently identical for the same cation in octahedral and tetrahedral coordinations. Thus, for octahedrally coordinated Fe^{3+} or Mn^{2+} ions, the sequence of crystal field states is $^6A_{1g}$, $^4T_{1g}$, $^4T_{2g}$, ^4E_g, $^4A_{1g}$, etc. A similar sequence, $^6A_1$, $^4T_1$, $^4T_2$, ^4E, $^4A_1$, etc., applies to these cations in tetrahedral coordination. The negative slope of the octahedral $^4T_{1g}$ level (or corresponding tetrahedral $^4T_1$ level) relative to the ground state octahedral $^6A_{1g}$ level (or tetrahedral $^6A_1$ level) results in a *lower* energy for the (octahedral) $^6A_{1g} \rightarrow {}^4T_{1g}$ transition compared to the (tetrahedral) $^6A_1 \rightarrow {}^4T_1$ transition. Thus, an absorption band representing this crystal field transition in tetrahedrally coordinated Fe^{3+} ions occurs at a *higher* energy than that for Fe^{3+} ions in octahedral coordination, apparently in contradiction to eq. (2.7). A similar situation applies to the (octahedral) $^6A_{1g} \rightarrow {}^4T_{2g}$ and (tetrahedral) $^6A_1 \rightarrow {}^4T_2$ transitions, but not to transitions involving the (octahedral) $^4A_{1g}$,^4E_g or (tetrahedral) $^4A_1$,^4E levels. This is because the energy separation between the $^6A_{1g}$ and $^4A_{1g}$,^4E_g levels is relatively unaffected by changes of crystal field strength. Such factors are apparent in crystal field spectral data of Mn^{2+}-and Fe^{3+}-bearing minerals summarized in tables 5.14, 5.15 and 10.2.

3.6 Energy level diagrams for low-symmetry environments

Further resolution of the $3d$ orbital energy levels takes place, as illustrated in fig. 2.9, when the symmetry of the environment about a transition metal is lowered from octahedral symmetry by either distortion of the coordination site or uneven distribution of the ligands forming the coordination polyhedron. Additional electronic configurations arise from the different arrangements of electrons in the resolved orbitals, each having a different energy and symmetry. Therefore, several additional crystal field states of lower degeneracies may now exist for each $3d^n$ configuration. The symmetry of each crystal field state is again designated by group theory notation.

To designate point symmetries of regular and distorted coordination polyhedra in transition metal-bearing phases, Schöenflies symbols are assigned to spectroscopic states, by convention, rather than the Hermann–

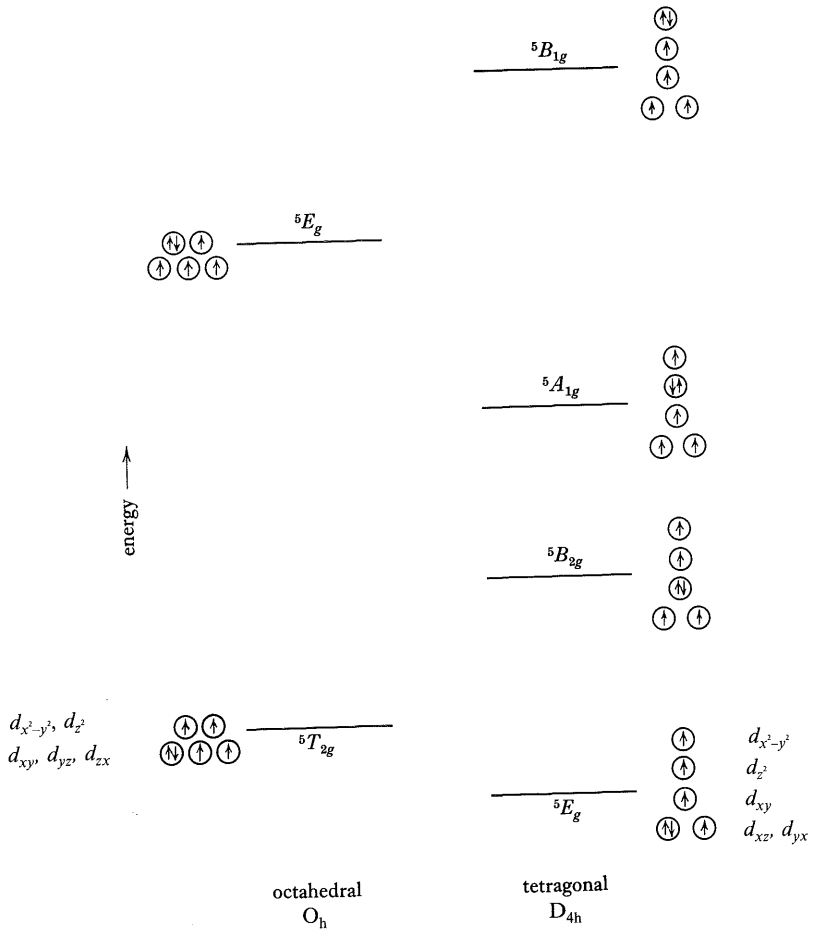

Figure 3.13 Crystal field states and electronic configurations of Fe^{2+} ions in regular octahedral and tetragonally distorted octahedral sites. The tetragonally distorted octahedron is elongated along the tetrad axis.

Mauguin symbols that are more familiar to mineralogists. Correlations between the Schöenflies and Hermann–Mauguin notations for different point symmetries are given in Appendix 6. Regular octahedra and tetrahedra have Schöenflies point symmetries O_h and T_d, respectively, while D_{4h} and C_{3v} may represent tetragonally distorted and trigonally distorted octahedra, respectively. Other examples of Schöenflies symbols denoting low-symmetry coordination sites in minerals are contained in Appendix 7, which also summarizes information about crystal structures of many transition metal-bearing phases. By convention, the major symmetry axis is taken to be the z electronic axis of

each electronic configuration. This axis usually corresponds to the axis of greatest distortion of a regular octahedron, tetrahedron or cube.

The energy separations between the crystal field states of a transition metal ion change when high-symmetry coordination polyhedra become distorted, and these are again portrayed by energy level diagrams. For example, the crystal field states of Fe^{2+} in a tetragonally distorted octahedral environment are shown in fig. 3.13. The octahedral $^5T_{2g}$ state is split into ^5E_g and $^5B_{2g}$ states and the excited octahedral ^5E_g state is split into $^5A_{1g}$ and $^5B_{1g}$ states in the symmetry D_{4h} environment. The electronic configurations of each of these states are also shown in fig. 3.13 (cf. fig. 2.8.*a*). In each configuration the z axis is the tetrad axis and corresponds to the axis of elongation of the octahedron.

The simplicity of energy level diagrams for transition metal ions in regular octahedral sites shown in figs 3.4 to 3.12 is lost when cations are located in low-symmetry environments, with many of the crystal field states becoming non-degenerate. For example, the crystal field states of Fe^{2+} in coordination polyhedra of different symmetries are summarized in table 3.5, together with examples of mineral crystal structures providing such distorted coordination sites. The crystal field states of Fe^{2+}, as well as those for transition metal ions with other $3d^n$ configurations in low-symmetry environments, may be derived from group theory (Cotton, 1990). Note that ground states of cations with spherically symmetrical configurations, for example, Fe^{3+} ($^6A_{1g}$), Cr^{3+} ($^4A_{2g}$), Ni^{2+} ($^3A_{2g}$), and low-spin Fe^{2+} ($^1A_{1g}$), remain as non-degenerate (A) crystal field states in low-symmetry environments, thereby simplifying somewhat assignments of their crystal field spectra.

3.7 Selection rules and intensities of absorption bands

The most important use of energy level diagrams described in §3.5 is to interpret visible to near-infrared spectra of transition metal compounds and minerals. The diagrams provide qualitative energy separations between split $3d$ orbitals and convey information about the number and positions of absorption bands in a crystal field spectrum. Two other properties of absorption bands alluded to in §3.3 are their intensities and widths.

Several factors affect intensities of crystal field spectra. In addition to enhancement by increased temperature and pressure discussed in chapter 9 (§9.4), intensities of absorption bands depend on: first, the spin-state or number of unpaired electrons possessed by a transition metal ion; second, whether or not the cation is located at the centre of symmetry of a coordination site; and third, interactions with next-nearest-neighbour cations.

Table 3.5. *Crystal field states of Fe^{2+} in coordination sites of different symmetries*

Symmetry of crystal field	Symmetry notation	Crystal field states	Mineral examples
octahedral	O_h	$T_{2g} + E_g$	magnesiowüstite; ≈ orthopyroxene M1
tetrahedral	T_d	$E + T_2$	spinel; ≈ staurolite
tetragonal (elongated oct.)	D_{4h}	$E_g + B_{2g} + A_{1g} + B_{1g}$	≈ olivine M1
tetragonal (compressed oct.)	D_{4h}	$B_{2g} + E_g + B_{1g} + A_{1g}$	≈ amphibole M3; ≈ biotite M1
square planar	D_{4h}	$A_{1g} + E_g + B_{2g} + B_{1g}$	≈ gillespite; ≈ eudialyte
trigonal (compressed oct.)	D_{3d}	$A_{1g} + E_g + E_g$	silicate spinel (γ-phase)
trigonal (compressed oct.)	C_{3v}	$A_1 + E + E$	≈ corundum; ≈ olivine M2
trigonal (compressed oct.)	C_3	$A + E + E$	ilmenite; corundum
orthorhombic (distorted cube)	D_2	$A + A + B_1 + B_2 + B_3$	almandine garnet
orthorhombic	C_{2v}	$A_2 + B_1 + B_2 + A_1 + A_1$	amphibole M4; ≈ orthopyroxene M2
monoclinic	C_{2h}	$B_g + B_g + A_g + A_g + A_g$	amphibole M3; biotite M1
monoclinic	C_2	$A + B + B + A + A$	calcic pyroxene M1; amphibole M1; biotite M2
monoclinic	C_s	$A' + A' + A' + A'' + A''$	olivine M2
triclinic	C_i	$A_g + A_g + A_g + A_g + A_g$	olivine M1
triclinic	C_1	$A + A + A + A + A$	orthopyroxene M1

Intensities of absorption bands are governed by probabilities of electronic transitions between the split $3d$ orbital energy levels. The probabilities are expressed by selection rules, two of which are the spin-multiplicity selection rule and the Laporte selection rule.

3.7.1 Laporte or parity selection rule

An electronic transition takes place through the interaction of the electric field of incident electromagnetic radiation with a component of the dipole moment of the absorbing atomic or molecular system. Such transitions usually involving light in the visible region of the spectrum can occur only between states that differ in parity; that is, one state must have a symmetric (g) wave function and the other an antisymmetric (u) wave function.

The probability of a transition, P_x, which influences the intensity of an absorption band, depends on the square of the transition moment, Q, expressed as

$$\sqrt{P_x} = Q \propto \int_0^{\infty} \Psi_g \, \mu_x \, \Psi_e \, dx, \tag{3.11}$$

where Ψ_g and Ψ_e are the wave functions of the ground and excited states, respectively, and μ_x is the dipole moment component of light polarized along the x axis. The significance of eq. (3.11) is that the probability of an electronic transition is zero unless Ψ_g and Ψ_e differ in parity.

The transition moment, Q, is related to the oscillator strength, f, which is a measure of intensity of an absorption band (table 3.2), by

$$f = 1.085 \text{ x } 10^{11} \, G \upsilon Q \, , \tag{3.12}$$

where υ is the frequency of the band in wavenumber units (cm^{-1}) and G is unity for a transition between non-degenerate states. Otherwise, $G = 1/\Omega$ for states of degeneracy Ω, and the oscillator strength is summed over all pairs of possible transitions.

The Laporte selection rule may also be expressed in the form $\Delta l = \pm 1$, for orbitally allowed transitions, where l is the azimuthal or orbital angular momentum quantum number (§2.2.2). In §2.2 it was noted that orbitals, being probability amplitude functions of electron distributions about the nucleus of an atom, have mathematical positive and negative signs associated with them as solutions to the Schrödinger wave equation. The *s* and *d* orbitals have similar signs because they are centrosymmetric (designated as subscript *g* in group theory notation), as do the *p* and *f* orbitals which lack inversion symmetry (designated as subscript *u*). Thus, *s* and *d* orbitals have identical parities, as do *p* and *f* orbitals, but *d* and *p* orbitals have opposite parities. Therefore, electronic transitions between *d* and *p* orbitals are allowed by the Laporte selection rule, whereas those between *d* and *s* orbitals are forbidden. In particular, electron transfer between two different *d* orbitals is forbidden. Thus, the excitation of an electron between a t_{2g} orbital and an e_g orbital of a transition metal ion in octahedral coordination is not allowed by the Laporte selection rule.

The Laporte selection rule is weakened, or relaxed, by three factors: first, by the absence of a centre of symmetry in the coordination polyhedron; second, by mixing of *d* and *p* orbitals which possess opposite parities; and third, by the interaction of electronic 3*d* orbital states with odd-parity vibrational modes. If the coordination environment about the cation lacks a centre of symmetry, which is the case when a cation occupies a tetrahedral site, some mixing of *d* and *p* orbitals may occur because they have symmetry operations in common in a tetrahedral environment. It may happen that a transition involving electron transfer from one 3*d* orbital to another embodies a small amount of transfer via *p* orbitals embraced in covalent bonding with surrounding ligands. Since transitions between *d* and *p* orbitals are allowed, a mechanism is available for the normally Laporte-forbidden transition of an electron between *e*-type and t_2-type 3*d* orbitals in a tetrahedrally coordinated transition metal ion. This leads to an absorption band in a spectrum, the intensity of which is proportional to the extent of mixing of *d* and *p* orbitals which, in turn, is inflenced by covalent bonding in a transition metal–ligand coordination cluster (chapter 11). In an octahedral site, however, mixing of the transition metal 3*d* and 4*p* orbitals is not possible when the cation lies at the centre of symmetry of the site because these orbitals have few symmetry operations in common in an octahedral environment. The overall result is that absorption bands originating from crystal field transitions within a given cation in an octahedral environment may be one-hundred times less intense than those within the cation tetrahedrally coordinated to the same ligands. One manifestation of this difference appears in crystal field spectra of basaltic glasses, for example, in which an absorption band at 1,800 nm originating from one per cent Fe^{2+} in tetrahedral sites would have an intensity comparable to an absorption band at 1,050 nm contributed by ninety-nine per cent Fe^{2+} in octahedral sites in the glass structure (Nolet *et al.*, 1979; Dyar and Burns, 1981).

3.7.1.1 Vibronic coupling

Another mechanism by which Laporte-forbidden transitions may occur, even in cations located in centrosymmetric (octahedral) sites, is through vibronic coupling, which involves coupling of *vib*rational and elect*ronic* wave functions with opposite parities. Electronic transitions between ground and excited states involve vibrational levels of the two states. The energy diagram illustrated in fig. 3.14 shows the potential energy surfaces of the ground and excited electronic states drawn as a function of one of the normal vibrational modes of a transition metal–ligand coordination cluster. In the simplest case illustrated in fig. 3.14, an electronic transition from the lowest vibrational mode of the ground electronic state takes place to several vibrational modes of the excited electronic state. According to a condition known as the Frank–Condon principle, an electronic transition between two energy states takes place in such a short time interval (~10^{-15} s) that the nuclei remain almost stationary during the transition. At the instant of an electronic transition, the excited state may have the same nuclear geometry as the ground state but may be highly excited vibrationally. However, relaxation to the ground vibrational level of the

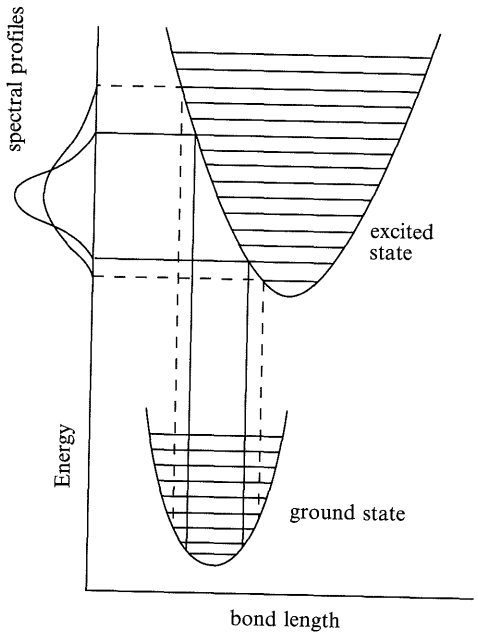

Figure 3.14 Potential energy diagram showing how an electronic transition takes place between vibrational levels of the ground and excited states. The illustration also demonstrates how the width and asymmetry of an absorption band changes at elevated temperature as a result of increased thermal population of vibrational levels of the ground electronic state (— low temperature; – – – elevated temperature). (Modified from Hitchman, 1985, figs 8 and 18.)

excited electronic state also occurs less rapidly (~10^{-12} s). In the course of molecular vibrations between the transition metal ion and ligands surrounding it in octahedral coordination, some of the vibrational modes cause the cation to be offset periodically from its equilibrium centrosymmetric position. Electronic transitions between different 3*d* orbital energy levels may then take place via vibrational sublevels with opposite parities, such as two of the acentric vibrational modes of an octahedron illustrated in fig. 3.15. Note that Greek letters are used to designate symmetries of vibrational modes (*e.g.*, α_{1g}, ε_u, τ_{1u}, etc.) in order not to confuse them with the symmetry notation of electron orbitals (*e.g.*, a_{1g}, t_{1u}, etc.) and crystal field states (e.g., A_{1g}, E_g, T_{1g}, etc.,) which are represented by Arabic symbols. Since molecular vibrations are thermally activated, intensification of crystal field transitions by the vibronic coupling mechanism is expected, and often observed, in high temperature crystal field spectra. Increased temperature also broadens absorption bands by the same mechanism and is discussed later (§3.9.4).

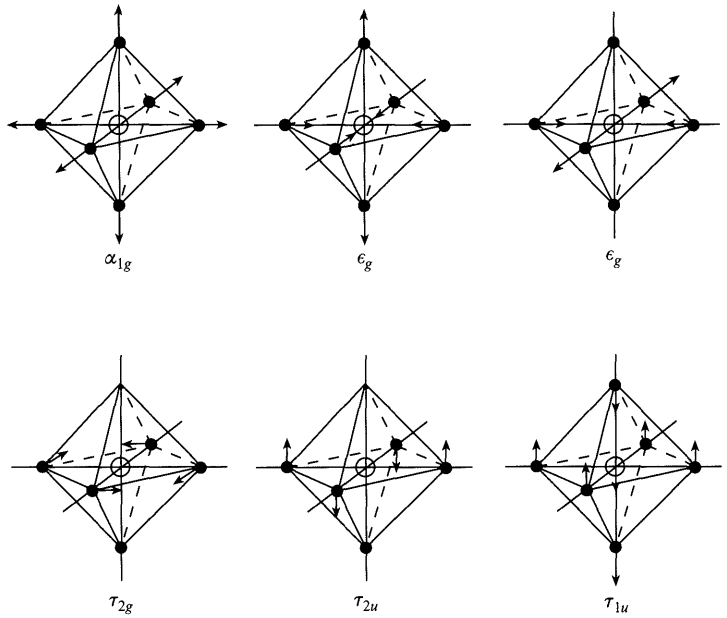

Figure 3.15 Vibrational modes of an octahedron. Note the acentric modes τ_{1u} and τ_{2u} which aid vibronic coupling.

3.7.2 Spin-multiplicity selection rule

The spin-multiplicity selection rule relates to changes in the number of unpaired electrons when they are excited between split 3*d* orbital energy levels within a cation. The selection rule states that the total number of unpaired electrons on an atom must remain unchanged during an electronic transition. Accordingly, spin-allowed transitions are distinguished in intensity from very weak spin-forbidden transitions in a crystal field spectrum, and depend on the electronic configurations of each cation. The simplest example of a spin-allowed transition is Ti^{3+}, $3d^1$, the single 3*d* electron of which in octahedral coordination occupies one of the t_{2g} orbitals in the ground state. The $^2T_{2g} \rightarrow {}^2E_g$ transition, which is portrayed by the absorption band at 493 nm in fig. 3.1 and results from a change of electronic configuration within Ti^{3+} from $(t_{2g})^1$ to $(e_g)^1$, is spin-allowed because there is no change in the number of unpaired electrons. A similar spin-allowed transition in octahedral Fe^{2+}, $^5T_{2g} \rightarrow {}^5E_g$, is responsible for the broad band centred near 1,000 nm in fig. 3.2.

In contrast to these spin-allowed transitions in Ti^{3+} and Fe^{2+}, only spin-forbidden transitions are possible in $3d^5$ cations such as Fe^{3+} and Mn^{2+} when they are coordinated to oxygen ligands. The electronic structures of these cations are such that in their ground-state configurations, $(t_{2g})^3(e_g)^2$ represented by

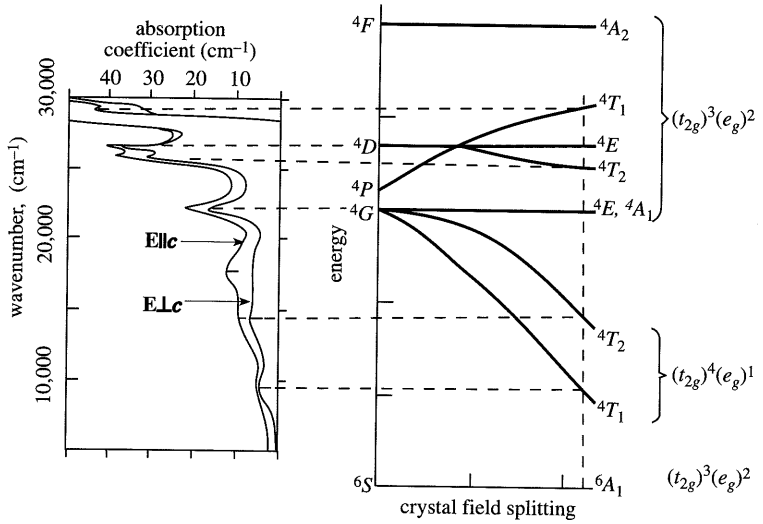

Figure 3.16 Energy level diagram for ferric iron matched to spin-forbidden crystal field transitions within Fe^{3+} ions, which are portrayed by the polarized absorption spectra of yellow sapphire (adapted from Ferguson & Fielding, 1972; Sherman, 1985a). Note that the unassigned band at ~17,600 cm^{-1} represents a paired transition within magnetically coupled Fe^{3+} ions located in adjacent face-shared octahedra in the corundum structure.

$^6A_{1g}$, there are five unpaired electrons when the cations occupy centrosymmetric octahedral sites. All possible crystal field transitions within Fe^{3+} and Mn^{2+} are to excited states with electronic configurations containing fewer unpaired electrons (fig. 3.9). Such transitions, because they are spin-forbidden, result in relatively low intensity absorption bands compared to Ti^{3+} and Fe^{2+}. The crystal field spectra of Fe^{3+}-bearing silicates and oxides, for example, such as the absorption spectra of yellow sapphire illustrated in fig. 3.16, contain two weak, broad bands in the vicinity of 9,500 cm^{-1} and 14,500 cm^{-1} (representing transitions from the $^6A_{1g}$ ground state to the $^4T_{1g}(G)$ and $^4T_{2g}(G)$ excited states, respectively), as well as superimposed sharp peaks at approximately 22,000 cm^{-1} (representing the $^6A_{1g} \rightarrow {}^4E_g, {}^4A_{1g}(G)$ transition) and other peaks located at higher energies in the ultraviolet region. The intensities of these spin-forbidden transitions in Fe^{3+}-bearing silicates are generally one or two orders of magnitude lower than the spin-allowed transitions within Fe^{2+} ions.

Spin-forbidden transitions are possible in other cations with two or more $3d$ electrons (except Cu^{2+}, $3d^9$). Thus, in oxygen ligand environments containing Fe^{2+} ions in octahedral coordination, spin-forbidden transitions also occur in the crystal field spectra, often appearing as weak, sharp peaks in the visible region, in addition to the broad spin-allowed bands located in the near-infrared

around 1,000 nm. For example, in the spectra of Fe^{2+} in the hydrated $[Fe(H_2O)_6]^{2+}$ ion (fig. 3.2), the two peaks identified near 20,000 cm^{-1} and 22,200 cm^{-1} represent the spin-forbidden transitions $^5T_{2g} \rightarrow {}^3T_{1g}$ and $^5T_{2g} \rightarrow {}^3T_{2g}$, respectively (compare fig. 3.7). Similar weak spin-forbidden peaks occur in the visible region in crystal field spectra of many of the ferromagnesian silicates described in chapter 5.

3.7.3 Coupling interactions with nearest-neighbour cations

Intensities of spin-forbidden crystal field bands, particularly those of ferric oxide minerals such as crystalline hematite (see fig. 10.2), may be enhanced by magnetic coupling of electron spins on next-nearest-neighbour Fe^{3+} ions when they occupy adjacent sites in a crystal structure. Spectroscopic selection rules for coupled Fe^{3+}–Fe^{3+} pairs differ from those for isolated individual Fe^{3+} ions (Sherman and Waite, 1985). Furthermore, additional transitions corresponding to simultaneous excitations within two adjacent Fe^{3+} ions may be present in visible-region spectra (Ferguson and Fielding, 1972). In the spectra of yellow sapphire shown in fig. 3.16, for example, another absorption band occurs at 18,690 cm^{-1} in addition to the crystal field transitions within individual Fe^{3+} ions at 9,450 cm^{-1} ($^6A_1 \rightarrow {}^4T_1$), 14,350 cm^{-1} ($^6A_1 \rightarrow {}^4T_2$) and 22,730 cm^{-1} ($^6A_1 \rightarrow {}^4E, {}^4A_1$). The additional feature at 18,690 cm^{-1} represents the pair excitation $^6A_1 + {}^6A_1 \rightarrow {}^4T_1 + {}^4T_1$ between two Fe^{3+} ions located in adjacent face-shared octahedra in the corundum structure (see fig. 5.4). Similar intensity enhancement of Fe^{2+} crystal field transitions occurs in optical spectra of mixed-valence Fe^{2+}–Fe^{3+} and Fe^{2+}–Ti^{4+} minerals (Smith, 1977, 1978b; Amthauer and Rossman, 1984; Mattson and Rossman, 1987a,b, 1988), including vivianite, babingtonite, tourmalines and other minerals described in chapters 4 and 5.

3.7.4 Relative intensities of crystal field spectra

Taking into account all of the factors influencing intensities of crystal field spectra discussed so far, the following generalizations may be made. Transitions of $3d$ electrons within cations in octahedral coordination are expected to result in relatively weak absorption bands. Intensification occurs if the cation is not centrally located in its coordination site. In tetrahedral coordination, the intensities of crystal field transitions should be at least one-hundred times larger than those in octahedrally coordinated cations. Spin-forbidden transitions are usually about one-hundred times weaker than spin-allowed transitions in centrosymmetric, octahedrally coordinated cations, but become

Table 3.6. *Relative intensities of absorption bands in transition metal-bearing minerals*

Type of electronic transition	Molar extinction coefficient, ε*	Mineral examples	Reference
	Crystal Field Transitions		
1. Spin-forbidden, Laporte-forbidden, centrosymmetric site	10^{-3} to 1	Fe^{3+} in garnet	fig. 4.9
2. Spin-forbidden, Laporte-forbidden, acentric site	10^{-1} to 10	Fe^{3+} in feldspars (tetrahedral)	fig. 5.22
		Fe^{3+} in epidote M3 (distorted oct)	fig. 4.9
3. Spin-forbidden, Laporte-forbidden, pair-enhancement	1 to 10	Fe^{3+} in corundum, hematite	fig. 3.16 fig. 10.2
4. Spin-allowed, Laporte-forbidden, centrosymmetric site	1 to 10	Fe^{2+} in olivine M1, gillespite	figs 5.9 & 4.3
	10 to 50	Mn^{3+} in andalusite M1	§4.4.2.2 & §5.4.4.1
5. Spin-allowed, Laporte-forbidden, acentric site	10 to 15	Fe^{2+} in olivine M2	fig. 5.9
	10 to 100	Fe^{2+} in pyroxene	fig. 5.15
	50 to 300	M2, amphibole M4	
		Mn^{3+} in epidote M3	fig. 4.2
	Electron Transfer Transitions		
6. Spin-allowed metal → metal intervalence charge transfer	10^2 to 10^3	$Fe^{2+} \rightarrow Fe^{3+}$ in glaucophane	fig. 4.16
		$Fe^{2+} \rightarrow Ti^{4+}$ in blue sapphire	fig. 4.17
7. Spin- and Laporte-allowed oxygen → metal charge transfer	10^3 to 10^5	$O \rightarrow Fe^{3+}$ in biotite and hornblende	§4.7.3

* ε has units litre $mole^{-1}$ cm^{-1} or litre $(g.ion)^{-1}$ cm^{-1}

intensified by magnetic interactions with cations in adjacent sites, especially in face-shared and edge-shared octahedra. Spin-forbidden transitions may also be intensified when cations occupy acentric coordination sites. Transitions allowed by both the spin-multiplicity and Laporte selection rules, such as oxygen → metal charge transfer transitions described later (§4.7.3 and §11.7.2), may be ten-thousand times more intense than crystal field transitions in octahedrally coordinated cations. Relative intensities of crystal field transitions are summarized in table 3.6.

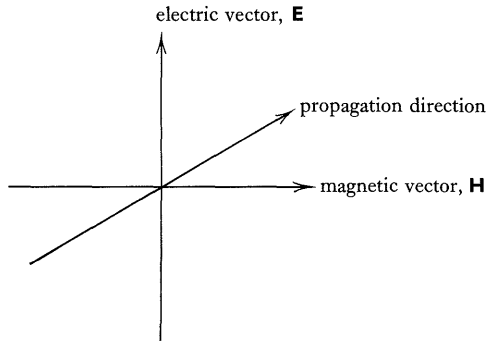

Figure 3.17 Orientations of the electric vector and magnetic vector with respect to the propagation direction of linearly polarized electromagnetic radiation.

3.8 Polarization dependencies of absorption bands

The crystal structures of transition metal compounds and minerals have either cubic or lower symmetries. The cations may occur in regular octahedral (or tetrahedral) sites or be present in distorted coordination polyhedra in the crystal structures. When cations are located in low-symmetry coordination environments in non-cubic minerals, different absorption spectrum profiles may result when linearly polarized light is transmitted through single crystals of the anisotropic phases. Such polarization dependence of absorption bands is illustrated by the spectra of Fe^{2+} in gillespite (fig. 3.3) and of Fe^{3+} in yellow sapphire (fig. 3.16).

Gillespite, $BaFe^{2+}Si_4O_{10}$, belongs to the tetragonal system and the crystal structure contains a coordination site closely approximating D_{4h} symmetry. The four coplanar oxygen atoms that are nearest to Fe are bonded to Si and lie at the corners of a square surrounding the Fe^{2+} cations. As a result of Fe^{2+} ions being in square planar sites, the crystal field spectra of gillespite differ for light polarized parallel and perpendicular to the optic axis (*c* axis). Similarly, since corundum is a trigonal mineral and trivalent cations occupy a trigonally distorted octahedron (point symmetry C_3), different spectrum profiles are obtained for Fe^{3+} in yellow sapphire when light is polarized parallel and perpendicular to the *c* axis (fig. 3.16). In order to account for the different spectrum profiles of these and other non-cubic minerals, it is necessary to examine the nature and properties of polarized light.

3.8.1 Electric and magnetic vectors in polarized light

Electromagnetic radiation has associated with it an electric vector **E** and a magnetic vector **H**. In linearly polarized light these vectors are mutually per-

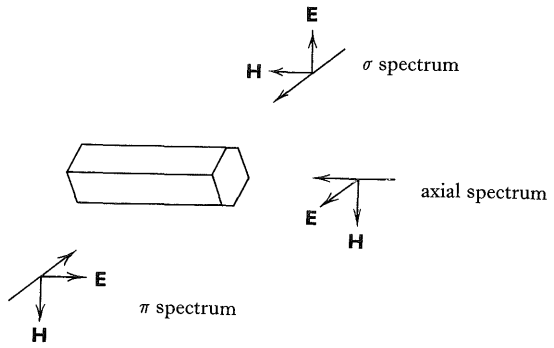

Figure 3.18 Three ways of measuring the polarized absorption spectra of a uniaxial crystal.

pendicular and are each perpendicular to the direction of propagation of light through a crystal. The orientations of the electric vector, magnetic vector and propagation directions are shown in fig. 3.17. Electromagnetic radiation may induce a transition by either a magnetic dipole or an electric dipole mechanism. In the visible region, electronic transitions between orbitals are dominated by electric dipole interactions. Contributions from magnetic dipole interactions are negligible, except when they help intensify weak spin-forbidden transitions as in Fe^{3+}-bearing minerals such as yellow sapphire (fig. 3.16), sulphates (Rossman, 1974; 1975) and oxyhydroxides (Sherman and Waite, 1985).

When light is passed through a polarizer such as a calcite Nicol prism, the electric vector is parallel to the plane of polarization. The electric vector transforms in different ways when the polarized light is transmitted through a single crystal of a mineral, depending on its crystal symmetry.

In cubic crystals no polarization of light occurs and the electric vector is identical in all crystallographic directions. Therefore, one spectrum only is observed in cubic crystals. Three types of spectrum are theoretically possible in uniaxial crystals, depending on the orientations of the electric and magnetic vectors with respect to the crystallographic axes (McClure, 1959). These are shown in fig. 3.18. In the axial spectrum the light propagation direction is along the optic axis corresponding, for example, to the c axis of gillespite and corundum. In the so-called σ spectrum (McClure, 1959), the propogation direction and electric vector are perpendicular to the optic axis, whereas the propagation direction and magnetic vector are perpendicular to the optic axis in the π spectrum. In electric dipole transitions the axial and σ spectra become identical so that in minerals of the tetragonal, trigonal and hexagonal systems only two spectrum profiles may be distinguished. These correspond to spectra obtained with the ordinary and extraordinary rays of polarized light, and are

designated as the ω (or $\mathbf{E}\perp c$) and ε (or $\mathbf{E}\|c$) spectra, respectively. Examples of such polarized spectra include those for gillespite and yellow sapphire illustrated in figs 3.3 and 3.16.

Six types of spectra are theoretically possible in minerals of the orthorhombic, monoclinic and triclinic systems (McClure, 1959). However, for electric dipole transitions only three spectra are usually distinguished. These are the α, β and γ spectra obtained when light is polarized along each of the three indicatrix axes, which in orthorhombic minerals such as olivine and orthopyroxene correspond to the three crystallographic axes. The majority of the spectra of minerals described in chapters 4 and 5 consist of polarized spectra measured in the three mutually perpendicular directions corresponding to α, β and γ polarized light.

When light impinges on a non-cubic mineral the electric vector transforms into different components, the symmetry properties of which depend on the direction of propagation of light through the crystal and the symmetry of the crystal structure. In cubic crystals, the electric vector is identical for light polarized along each of the three tetrad axes. For an octahedal site in a cubic crystal, the electric vector has group theory symmetry T_{1u}; for a tetrahedral site, it is represented by T_2 symmetry. In a tetragonal crystal with D_{4h} symmetry such as gillespite, the electric vector has A_{2u} symmetry when light is polarized along the c axis and E_u symmetry for light polarized perpendicular to the c axis. In a trigonal crystal with C_3 symmetry such as yellow sapphire, the electric vector has either A_1 ($\mathbf{E}\|c$) or E ($\mathbf{E}\perp c$) symmetry. In crystals of lower symmetries, the electric vector is represented by different group theory symmetries when polarized along each of the three optical indicatrix axes.

Methods of group theory are used to ascertain whether electronic transitions will take place between crystal field states of a transition metal ion for light polarized along each electronic axis. This axis may or may not coincide with a crystallographic or optical indicatrix axis of the host crystal. Intensities of absorption bands in polarized light hinge upon expressions for the transition probability such as that in eq. (3.10). Not only must the transition probability, P_x, be non-zero and have a finite value, implying that the wave functions for the ground state (Ψ_g) and excited state (Ψ_e) have opposite parities, but the product of group theory representations of quantities in the integral in eq. (3.10) must be totally symmetric, that is, it must possess A_1 or A_{1g} symmetry. Stated in group theory terminology, the transition probability (P_x) is determined from the symmetry of the ground state and excited state by constructing the direct product involving the irreducible representations of the wave functions of the two states (Γ_g and Γ_e, respectively) and the electric dipole vector (Γ_μ). If the direct product, $\Gamma_g \times \Gamma_\mu \times \Gamma_e$, contains the A_1 or A_{1g} representation, the transition is allowed. If the A_{1g} (or A_1) representation is absent from the

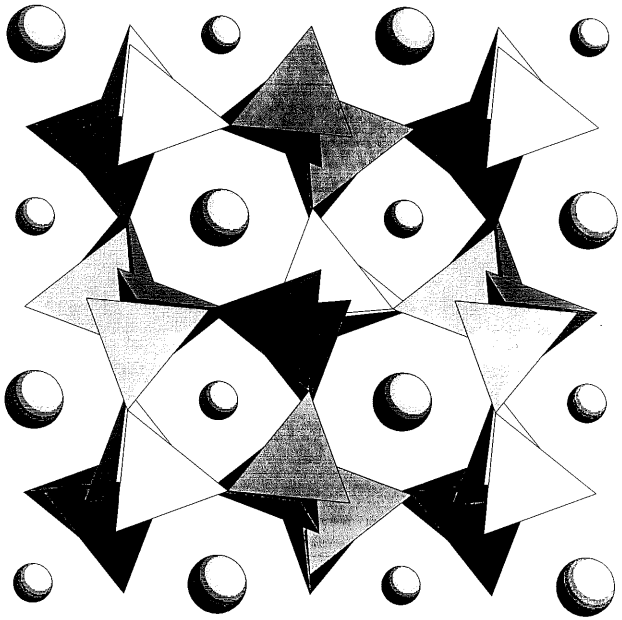

Figure 3.19 The crystal structure of gillespite projected down the c axis. Large spheres: Ba^{2+}; small spheres: Fe^{2+} in square planar coordination; tetrahedra: linked $[SiO_4]$.

factorized direct product, the transition is forbidden. Such direct product calculations are simplified by the use of character tables, which provide a shorthand notation of the symmetry properties of the crystal field states and electric vectors in coordination sites with a particular symmetry. An elementary account of such calculations is given by Cotton (1990).

3.8.2 Group theoretical interpretation of gillespite polarized spectra

The polarized spectra of gillespite, $BaFe^{2+}Si_4O_{10}$, shown in fig. 3.3 serve to illustrate these group theoretical methods for assigning absorption bands. This rare tetragonal layered silicate mineral containing Fe^{2+} ions in square planar coordination with oxygen ions has figured prominently in developments of spectral mineralogy, having played a key role in understanding $3d$ orbital energy levels and predicting pressure-induced spin-pairing transitions in Fe^{2+}–bearing minerals in the Earth's interior (§9.7.3). The platey habit of gillespite is particularly favourable for measuring and assigning absorption bands in its polarized crystal field spectra.

The gillespite structure is illustrated in fig. 3.19. The planar $[FeO_4]$ group, strictly speaking, has C_4 symmetry. However, the Fe^{2+} ion is only 0.3 pm out of

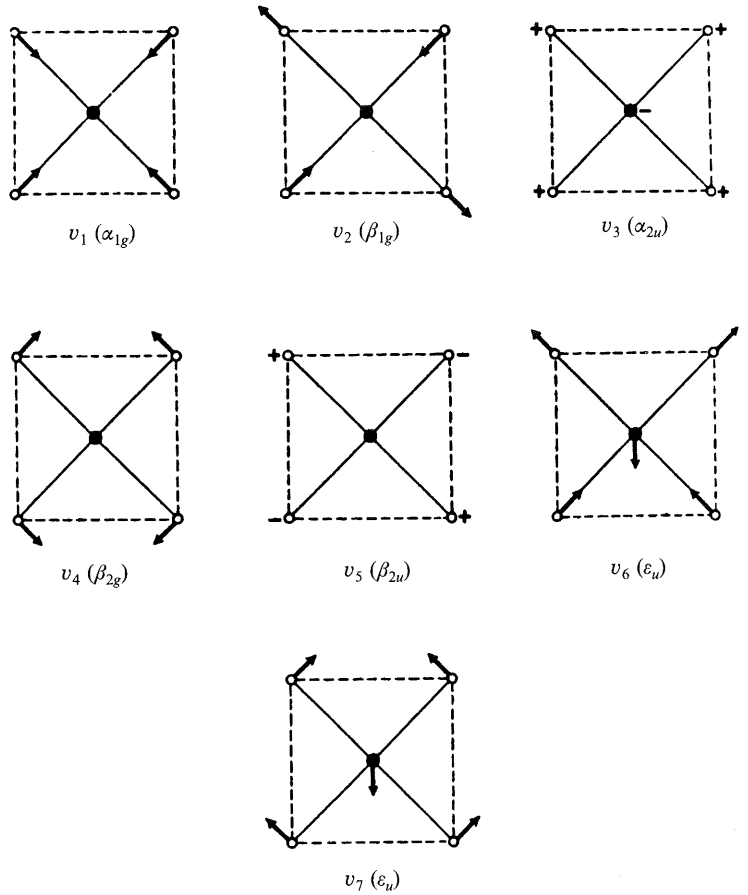

Figure 3.20 Vibrational modes, υ_1 to υ_7, of atoms in a square planar site such as the $[FeO_4]$ coordination environment in gillespite (from Hitchman, 1985). Note the acentric α_{2u}, β_{2u} and ε_u modes that facilitate electronic transitions within Fe^{2+} ions by vibronic coupling.

the plane of the four coordinating oxygen atoms, with diagonal O–Fe–O angles of 178° and all four Fe–O distances equal to 200 pm. Therefore, the $[FeO_4]$ group very closely approximates D_{4h} symmetry. In addition, the square planar site is aligned perpendicular to the optic axis. Thus, the z electronic axis of the $3d$ orbitals coincides with the c crystallographic axis. A square planar coordination site may be regarded as one of the limiting cases of tetragonal distortion of an octahedron (cf. figs 2.8 and 3.13) in which two ligands along the z electronic axis are completely removed. Since repulsion of electrons by surrounding ligands is minimal along the z axis, orbitals projecting in this direction are more stable than those with lobes in the x–y plane. Therefore, the order

Table 3.7. *Assignments of absorption bands in the polarized spectra of gillespite*

Spectrum	Electric vector: Polarization	Electric vector: Group theory representation (Γ_μ)	Transition ($\Psi_g \rightarrow \Psi_e$)	Direct product ($\Gamma_g \times \Gamma_\mu \times \Gamma_e$)	Vibrational mode allowing vibronic coupling (Fig. 3.20)	Assignment (position of peak in cm^{-1}) (Fig. 3.3)
ε	parallel to c (**E**$\parallel c$)	A_{2u}	$^5A_{1g} \rightarrow {}^5E_g$	E_u	ε_u	$\approx$ 2,500
			$^5A_{1g} \rightarrow {}^5B_{2g}$	B_{1u}	none	forbidden
			$^5A_{1g} \rightarrow {}^5B_{1g}$	B_{2u}	β_{2u}	19,650
ω	perpendicular to c (**E**$\perp c$)	E_u	$^5A_{1g} \rightarrow {}^5E_g$	$A_{2u}+B_{2u}+E_u$	$\alpha_{2u}, \beta_{2u}, \varepsilon_u$	$\approx$ 2,500
			$^5A_{1g} \rightarrow {}^5B_{2g}$	E_u	ε_u	8,300
			$^5A_{1g} \rightarrow {}^5B_{1g}$	E_u	ε_u	20,160

of increasing energy of the 3*d* orbitals is: $d_{z^2} < d_{xz} = d_{yz} < d_{xy} < d_{x^2-y^2}$. The ground state of Fe^{2+} in gillespite has an electronic configuration $(d_{z^2})^2(d_{xz})^1(d_{yz})^1(d_{xy})^1(d_{x^2-y^2})^1$ and symmetry $^5A_{1g}$. Excited states are ^5E_g, $^5B_{2g}$ and $^5B_{1g}$. Thus, electronic transitions between the $^5A_{1g}$ ground state and each of these excited states appear likely. However, since each crystal field state is centrosymmetric, such transitions are forbidden by the Laporte selection rule (§3.7.1). Transitions may be allowed by vibronic coupling, however. The symmetries of the vibrational modes of the square $[FeO_4]$ group illustrated in fig. 3.20 are α_{1g}, α_{2u}, β_{1g}, β_{2g}, β_{2u} and two with ε_u symmetry. Thus, they include three types (α_{2u}, β_{2u} and ε_u) having acentric vibrational modes.

To account for the polarization dependencies of the absorption bands in the polarized spectra of gillespite in fig. 3.3, it is necessary to consider the symmetry properties of the electric vector of light in a tetragonal (symmetry D_{4h}) crystal, which are A_{2u} (parallel) and E_u (perpendicular) relative to the optic axis (or *c* crystallographic axis) coinciding exactly with the *z* electronic axis of iron in the square planar site in gillespite. Evaluations of direct products involving the symmetry properties of the crystal field ground state (A_{1g}), with each excited state (E_g, B_{2g} or B_{1g}), each component of the electric dipole moment (A_{2u} or $\mathbf{E}_u$) and the various acentric vibrational modes (α_{2u}, β_{2u} or ε_u) through the use of character tables (e.g., Cotton, 1990) leads to the interpretation of the polarized spectra summarized in table 3.7.

The assignments summarized in table 3.7 reveal that all electronic transitions in gillespite are allowed through the mechanism of vibronic coupling *except* the transition $^5A_{1g} \rightarrow {}^5B_{2g}$ in light polarized along the optic axis (**E**$\parallel c$ spectrum) for which no vibrational mode exists to assist this electronic transition. This accounts for the absence of an absorption band at about 1,200 nm (8,300 cm^{-1}) in the **E**$\parallel c$ spectrum of gillespite shown in fig. 3.3. Note that the low energy transition $^5A_{1g} \rightarrow {}^5E_g$ leads to an absorption band beyond the wavelength range shown in the spectra in fig. 3.3. Studies of the crystal field spectra of cuprorivaite or Egyptian blue, $CaCuSi_4O_{10}$ (Clark and Burns, 1967; Ford and Hickman, 1979), and synthetic $CaCrSi_4O_{10}$ (Belsky *et al.*, 1984), which are isostructural with gillespite and contain Cu^{2+} or Cr^{2+} ions in the square planar coordination site, lead to estimates of $\leq$ 2,500 cm^{-1} for the $^5A_{1g} \rightarrow {}^5E_g$ transition in gillespite.

The interpretation of the crystal field spectra of gillespite is simplified by the high symmetry of this tetragonal mineral and by the coincidence of the electronic axes of Fe^{2+} in the square planar site with the electric vectors of polarized light, due to the perfect alignment of the $[FeO_4]$ plane perpendicular to the *c* axis. Detailed spectral analyses of most other non-cubic transition metal-bearing minerals become increasingly difficult when electronic axes within a coordination site do not coincide with optic axes of polarized light. This occurs

in most silicate minerals, including orthopyroxene, the spectra of which have been interpreted, nevertheless, by group theory (e.g., Goldman and Rossman, 1977a; Rossman, 1988). Because of such misalignments in silicates, a small component of an electronic transition which may be allowed along one electronic axis that is inclined to the light polarization axes often causes the absorption band to occur with different intensities in all three polarized spectra.

3.9 Widths of absorption bands

Absorption bands in crystal field spectra are not sharp lines. Instead, as the spectra illustrated in figs 3.1, 3.2 and 3.3 show, they contain rather broad envelopes approximating gaussian profiles which at half peak-height may have full widths ranging from <100 cm^{-1} to 1,000–2,000 cm^{-1}. Several factors lead to broadened absorption bands and they are discussed below.

3.9.1 Correlations with energy level diagrams

Energy level diagrams, which provide a measure of relative energies of crystal field transitions, also account for relative widths of absorption bands in crystal field spectra of transition metal compounds. The widths are related to the slope differences of crystal field states in an Orgel or Tanabe–Sugano energy level diagram. Atoms in a structure are in continual thermal vibration about their mean positions. As cations and surrounding ligands vibrate about their structural positions through vibrational modes such as those illustrated in figs 3.15 and 3.20, metal–ligand distances vary so that Δ oscillates about a mean energy corresponding to the average position of the atoms. If the energy separation between the ground state and an excited state is a sensitive function of Δ, the energy difference will vary appreciably over the range through which Δ varies in response to vibrations of the metal and ligand atoms. Electronic transitions between the two states will result in a broad absorption band. If, however, there is little variation in the energy separation between the ground and excited states with fluctuating Δ, an electronic transition between these states will lead to a sharp absorption band.

These features are particularly well illustrated by crystal field spectra of $3d^5$ cations, such as those of Fe^{3+} ions in yellow sapphire illustrated in fig. 3.16. The energy separations between the $^6A_{1g}$ ground state and the $^4T_{1g}$ and $^4T_{2g}$ excited states of Fe^{3+} converge with increasing Δ but the energy separation between the $^6A_{1g}$ and ^4E_g,$^4A_{1g}$ levels shown in fig. 3.10 remains constant. As a result, crystal field spectra of Fe^{3+} in yellow sapphire (fig. 3.16), Fe^{3+} in epidote (fig. 4.9) and Mn^{2+} in tephroite (fig. 4.8*a*) typically show two broad bands at longer wavelengths and one or two sharp peaks in the visible region.

Broadening of absorption bands is commonly found for electronic transitions between two crystal field states arising from the same spectroscopic term. For example, the $^5T_{2g}$ and ^5E_g states are both derived from the ^5D ground term of Fe^{2+} (figs 3.7 and 3.8). The energy separation between the two crystal field states increases with increasing Δ_o. As a result, the $^5T_{2g} \rightarrow {}^5E_g$ transition in Fe(II) compounds is represented by a broad absorption band. This partially accounts for the broad band centred around 10,000 cm^{-1} in the spectrum of the hydrated Fe^{2+} ion in fig. 3.2. A similar explanation applies to the $[Ti(H_2O)_6]^{3+}$ spectrum shown in fig. 3.1.

3.9.2 The dynamic Jahn–Teller effect.

Another factor contributing to the asymmetry and breadth of absorption bands in crystal field spectra of transition metal ions is the dynamic Jahn–Teller effect, particularly for dissolved hexahydrated ions such as $[Fe(H_2O)_6]^{2+}$ and $[Ti(H_2O)_6]^{3+}$, which are not subjected to static distortions of a crystal structure. The degeneracies of the excited ^5E_g and ^2E_g crystal field states of Fe^{2+} and Ti^{3+}, respectively, are resolved into two levels during the lifetime of the electronic transition. This is too short to induce static distortion of the ligand environment even when the cations occupy regular octahedral sites as in the periclase structure. A dual electronic transition to the resolved energy levels of the E_g excited states causes asymmetry and contributes to the broadened absorption bands in spectra of most Ti(III) and Fe(II) compounds and minerals (cf. figs 3.1, 3.2 and 5.2).

3.9.3 Effects of multiple site occupancies

Broadening of absorption bands also results from the superposition of close-spaced bands originating from a single transition metal ion located in a low-symmetry coordination site, or from the cations being distributed over two or more structurally similar sites. Each of these factors is significant in crystal field spectra of silicate minerals, the structures of which often contain transition metal ions in two or more distorted sites. Even in crystal structures providing a single crystallographic position, different next-nearest-neighbour distributions resulting from atomic substitution in minerals may prevent a specific transition metal ion from being in identical coordination environments, again contributing to the breadth of absorption bands.

3.9.4. Vibrational interactions

Implicit in the foregoing discussion is that increased temperature, which increases thermal motions of atoms in a crystal structure, also contributes to

the broadening of absorption bands in a crystal field spectrum. Since the crystal field splitting is proportional to the inverse fifth-power of the metal–ligand distance, eq. (2.17), energy separations between crystal field states are very sensitive to changes of interatomic distances induced by thermal expansion of a crystal structure, eq. (2.25).

Thermal broadening of an electronic transition results from the population of additional vibrational levels of the electronic ground state illustrated by the potential energy diagram in fig. 3.14. Conversely, spectral features may be narrowed, and better resolution of absorption bands achieved, by performing crystal field spectral measurements at low temperatures. Under these conditions, vibrational peaks may contribute to fine structure observed on electronic absorption bands of transition metal-bearing phases, particularly in low temperature spectra.

3.9.5 Band shape

As noted earlier (§3.2.2), absorption bands are assumed to have gaussian shape, eq. (3.6). However, vibrational interactions may modify their shapes and contribute to asymmetric profiles in crystal field spectra. At low temperatures when few vibrational modes are active in the electronic ground state, absorption bands may be comparatively narrow, as indicated by the potential energy level diagram in fig. 3.14. At elevated temperatures, a Boltzmann distribution results in increased populations of higher energy vibrational modes so that excitation of electrons to higher energy crystal field states takes place over a wider range of vibrational modes. Due to anharmonicity of potential energy curves, absorption bands broaden more towards lower frequencies, thereby modifying the gaussian shape and causing asymmetry towards long wavelength tails of absorption bands. The position of the absorption maximum may also change with temperature as an increased number of higher energy vibrational modes become occupied.

3.10 Ligand field parameters for distorted environments

The ligand field parameter for cations in a regular octahedral environment, 10 *Dq*, expressed by eq. (2.17),

$$\Delta_0 = 10Dq = \frac{Z_L e^2}{6R^5} < r^4 > \qquad (2.17)$$

and embracing the radial integral term, $<r^4>$, must be modified in low-symmetry environments to take into account angular distortions and variations of

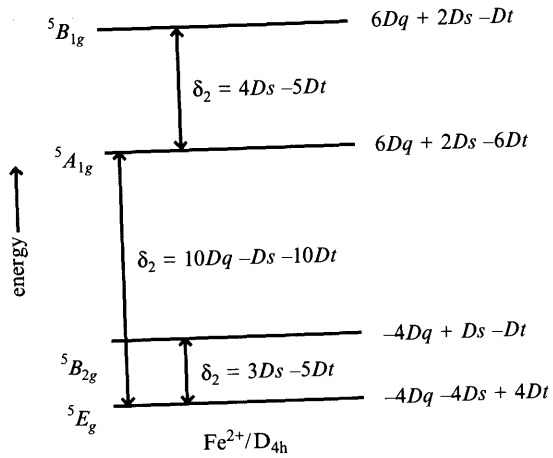

Figure 3.21 Ligand field energy separations for Fe^{2+} ions in a tetragonally elongated octahedron (compare fig. 3.13). The inverted diagram applies to Mn^{3+} in a similar D_{4h} environment.

metal–ligand distances (*R*) in deformed coordination polyhedra or uneven arrangements of different ligands surrounding the central cation. Such asymmetries require the specification of an additional parameter, C_p, (Gerloch and Slade, 1973), defined as

$$Cp = \frac{Z_L e^2}{7R^3} < r2 >. \qquad (3.13)$$

A particularly common type of distortion involves the lowering of symmetry of a ligand coordination polyhedron from O_h to D_{4h}. In such a tetragonally distorted octahedron, the *Dq* parameter has two values resulting from different metal–ligand distances represented by the four equatorial (eq) and two axial (ax) bonds. Two additional radial integral splitting parameters, *Ds* and *Dt*, are used to express the orbital energies of the individual 3*d* orbitals (Ballhausen, 1962, p. 100; Gerloch and Slade, 1973; Lever, 1984, p. 19)

$$Ds = Cp_{(eq)} - Cp_{(ax)} \qquad (3.14)$$

$$Dt = \tfrac{4}{7}\,[Dq_{(eq)} - Dq_{(ax)}]\,. \qquad (3.15)$$

The *Dt* parameter is a measure of the difference between the equatorial and axial *Dq* parameters. In an elongated octahedron, the energy separations between pairs of 3*d* orbital energy levels are expressed by

$$\begin{aligned} b_{2g} - e_g &= \delta_1 = 3\,Ds - 5\,Dt \\ a_{1g} - e_g &= \delta_2 = 10\,Dq_{(eq)} - Ds - 10\,Dt \\ b_{1g} - a_{1g} &= \delta_3 = 4\,Ds + 5\,Dt\,. \end{aligned} \qquad (3.16)$$

Analogous expressions apply to crystal field states for electronic configurations involving these orbitals (cf. fig. 3.13). These energy separations are shown in fig. 3.21. All three parameters, $Dq_{(eq)}$, Dt and Ds, may be determined experimentally provided that energies of three absorption bands originating from transition metal ions in tetragonally distorted octahedral sites occur in the crystal field spectra. Equation (3.15) yields the $Dq_{(ax)}$ parameter, so that the mean Dq parameter, $Dq_{(av)}$ may be calculated from

$$Dq_{(av)} = \tfrac{1}{6}\,[4\,Dq_{(eq)} + 2\,Dq_{(ax)}]\,. \qquad (3.17)$$

This method of evaluating ligand field parameters for transition metal ions in tetragonally distorted octahedra is particularly applicable to minerals containing Mn^{3+} and Cr^{2+}, as well as Fe^{2+} ions in some very distorted octahedra, because their crystal field spectra enable δ_1, δ_2 and δ_3 (eq. 3.16)) to be determined experimentally. Examples are discussed in chapter 5 particularly when crystal field spectra of Mn^{3+}-bearing minerals are described (§5.10.5).

3.11 Summary

Chapter 3 describes the theory of electronic spectra of transition metal ions. The three characteristic features of absorption bands in a spectrum are position or energy, intensity of absorption and width of the band at half peak-height. Positions of bands are commonly expressed as wavelength (micron, nanometre or ångstrom) or wavenumber (cm^{-1}) units, while absorption is usually displayed as absorbance, absorption coefficient (cm^{-1}) or molar extinction coefficient [litre $(g.ion)^{-1}\,cm^{-1}$] units.

Spectroscopic terms. Each isolated ion gives rise to several spectroscopic terms, each term representing an energy level resulting from a different arrangement of electrons in atomic orbitals. Spectroscopic terms are designated by letter symbols, ${}^rL$, denoting the total atomic orbital angular momenta of unpaired electrons (L) and the spin multiplicity (r)which are calculated by adding one to the number of unpaired electrons. Energy separations between spectroscopic terms are determined from atomic spectra of gaseous ions.

Crystal field states and positions of absorption bands. The spectroscopic terms are split into one or more crystal field states when a transition metal ion is located in a coordination site in a crystal structure. Each crystal field state represents a different electronic configuration of $3d$ orbitals. Crystal field states are labelled by group theory notation summarizing the symmetry properties of the electronic configurations and the spin multiplicities. Energy level diagrams, including Orgel and Tanabe–Sugano diagrams, show how anions or ligands coordinated to the cation influence interelectronic coulombic and exchange interactions between the $3d$ electrons. For crystal field states with highest spin multiplicities, energy level diagrams for cations with d^n and d^{10-n} configurations show qualitative similarities, with one diagram representing the inverted form of the other. The diagrams also bear an inverse relationship for cations in octahedral and tetrahedral (or cubic and dodecahedral) sites. As a result, there are essentially only three types of energy level diagrams, correlating with three distinct absorption spectrum profiles, for the various $3d$ electronic configurations in high-symmetry environments. One type applies to $3d^5$ cations, a second to $3d^1$, $3d^6$, $3d^4$ and $3d^9$ cations, and the third to cations with $3d^2$, $3d^7$, $3d^3$ and $3d^8$ configurations. When a transition metal ion is situated in a distorted coordination site, or the ligands are unevenly distributed about the cation, further resolution of the $3d$ orbital energy levels takes place. The number and positions of absorption bands in visible to near-infrared spectra reflect energy separations between electronic configuration differing in symmetry in the non-cubic coordination environments.

Selection rules and intensities of absorption bands. The probability of electronic transitions between different crystal field states, which influences intensities of absorption bands in crystal field spectra, may be deduced from selection rules. The spin-multiplicity selection rule specifies that transitions may take place only between ground and excited states having the same number of unpaired electrons. Spin-allowed transitions occur in crystal field spectra of most transition metal ions except cations with high-spin $3d^5$ configurations. Thus, spin-forbidden transitions, observed in minerals containing Mn^{2+} and Fe^{3+} ions, produce very weak absorption bands, which may gain intensity by spin–orbit coupling of electrons and magnetic interactions between neighbouring cations. The Laporte selection rule specifies that electronic transitions between orbitals of the same type and quantum number, such as two $3d$ orbitals, are forbidden. However, crystal field transitions involving electrons in t_{2g} and e_g orbitals may take place and gain intensity whenever cations occur in coordination environments, such as tetrahedral sites, that lack a centre of symmetry. In centrosymmetric octahedral sites, absorption bands gain intensity by vibronic coupling when electronic transitions proceed via acentric vibrational modes of the cation and surrounding ligands.

Polarization dependence of absorption bands. The occurrence of transition metal ions in low-symmetry coordination sites leads to crystallographic dependencies of absorption spectra for non-cubic minerals in polarized light. Interpretations of such polarized spectra using methods of group theory hinge upon considerations of symmetry properties of ground and excited crystal field states as well as the electric vectors of polarized light transmitted through the crystal. For centrosymmetric cations, symmetries of vibrational modes must also be taken into account. The polarized spectra of gillespite, $BaFeSi_4O_{10}$, a tetragonal mineral with Fe^{2+} ions in square planar coordination, illustrate group theoretical methods for analysing absorption bands in visible to near-infrared spectra.

Widths of absorption bands. Thermal vibrations of atoms produce fluctuating energy separations between 3*d* orbital energy levels, leading to broadened and asymmetric absorption bands, particularly at elevated temperatures. Sharp peaks in visible-region spectra of Mn^{2+}- and Fe^{3+}-bearing minerals are due to transitions between crystal field states of constant energy separation. Superposition of two or more bands representing transitions to closely spaced energy levels of transition metal ions either located in a single low-symmetry site or distributed over several structurally similar sites may also broaden absorption bands.

3.12 Background reading

Ballhausen, C. J. (1962) *Introduction to Ligand Field Theory*. (McGraw–Hill, New York), 298 pp.

Burns, R. G. (1985) Electronic spectra of minerals. In *Chemical Bonding and Spectroscopy in Mineral Chemistry*. (F. J. Berry & D. J. Vaughan, eds; Chapman & Hall, London), pp. 63–101.

Cotton, F. A. (1990) *Chemical Applications of Group Theory, 3rd edn.* (Wiley–Interscience, New York), 579 pp.

Figgis, B. N. (1966) *Introduction to Ligand Fields*. (Interscience Publ., New York), 351 pp.

Gerloch, M. & Slade, R. C. (1973) *Ligand–Field Parameters*. (Cambridge Univ. Press, Cambridge), 235 pp.

Henderson, B. & Imbusch, G. F. (1989) *Optical Spectroscopy of Inorganic Solids*. (Oxford Univ. Press, Oxford), ch. 2 & 3.

Hitchman, M. A. (1985) Chemical information from the polarized crystal spectra of transition metal complexes. In *Transition Metal Chemistry, vol. 9*. (G. A. Melson & B. N. Figgis, eds; Marcel Dekker, Inc., New York), pp. 1–223.

Lever, A. B. P. (1984) *Inorganic Electronic Spectroscopy, 2nd edn.* (Elsevier, Amsterdam), 863 pp.

McClure, D. S. (1959) Electronic spectra of molecules in crystals. Part II: Spectra of ions in crystals. *Solid State Phys.*, 9, 399–425.

Marfunin, A. S. (1979) *Physics of Minerals and Inorganic Materials*. (Springer–Verlag, New York), chs 1 & 2.

Orgel, L. E. (1966) *An Introduction to Transition-Metal Chemistry: Ligand-Field Theory, 2nd edn.* (Methuen, London), ch. 6.

4

Measurements of absorption spectra of minerals

Since ferrous iron usually colors minerals green, and ferric iron yellow or brown, it may seem rather remarkable that the presence of both together should give rise to a blue color, as in the case of vivianite. – – Other instances may perhaps be discovered, should this subject ever be investigated as it deserves to be.

E. T. Wherry, *Amer. Mineral.*, 3, 161 (1918)

4.1 Introduction

In order to apply crystal field theory to geologic processes involving transition metal ions, it is necessary to have crystal chemical information and thermodynamic data for these cations in mineral structures. In §2.8, it was noted that the principal method for obtaining crystal field splittings, and hence stabilization energies of the cations, is from measurements of absorption spectra of transition metal compounds at wavelengths in the visible and near-infrared regions. The origins of such absorption bands in crystal field spectra were discussed in chapter 3. The focus of this chapter is on measurements of absorption spectra of minerals, with some applications to fundamental crystal chemical problems.

When minerals occur as large, gem-sized crystals, it is comparatively easy to obtain absorption spectra by passing light through natural crystal faces or polished slabs of the mineral. However, most rock-forming minerals are present in assemblages of very small crystals intimately associated with one another, leading to technical problems for measuring spectra of minerals *in situ*. In addition, several of the transition elements occur in only trace amounts in common minerals, making spectral features of individual cations difficult to resolve, especially in the presence of more abundant elements such as iron, titanium and manganese which also absorb radiation in the visible to near-infrared region. Mineral spectroscopists are continually searching for exotic